
# ADJUSTABLE DYNAMIC RANGE FOR PAPR REDUCTION SCHEMES IN LARGE-SCALE MIMO-OFDM SYSTEMS

A Thesis submitted by

Thana Udomsripaiboon, M Eng

For the award of

Doctor of Philosophy

2017

# Abstract

In a multi-input-multi-output (MIMO) communication system there is a necessity to limit the power that the output antenna amplifiers can deliver. Their signal is a combination of many independent channels, so the demanded amplitude can peak to many times the average value. The orthogonal frequency division multiplexing (OFDM) system causes high peak signals to occur because many subcarrier components are added by an inverse discrete Fourier transformation process at the base station. This causes out-of-band spectral regrowth. If simple clipping of the input signal is used, there will be in-band distortions in the transmitted signals and the bit error rate will increase substantially.

This work presents a novel technique that reduces the peak-to-average power ratio (PAPR). It is a combination of two main stages, a variable clipping level and an Adaptive Optimizer that takes advantage of the channel state information sent from all users in the cell.

Simulation results show that the proposed method achieves a better overall system performance than that of conventional peak reduction systems in terms of the symbol error rate. As a result, the linear output of the power amplifiers can be minimised with a great saving in cost.

# Certification of Thesis

This thesis is entirely the work of Mr. Thana Udomsripaiboon except where otherwise acknowledged. The work is original and has not previously been submitted for any other award, except where acknowledged.

Student and supervisors signatures of endorsement are held at USQ.

*Prof., John Billingsley*

Principal Supervisor

*Dr Andrew Maxwell*

Associate Supervisor

# Acknowledgments

First and the foremost, I would like to express my deepest gratitude to my principal supervisor Prof. John Billingsley for his endless commitment to directing the research and invaluable guidance. Without his motivation and guidance, would not have been completed.

I would like to express my sincere thanks to my associate supervisor Dr Andrew Maxwell for his support and encouragement throughout my PhD studies.

I am also thankful to my previous supervisor, Prof. Wei Xiang from JCU, for his instructive discussions and constructive suggestions to my thesis.

I would like to thank the Staff Development Scholarship of the University of Phayao for supporting my study at USQ during these three years. In addition, a special thank to all my friends and colleagues at USQ.

I would like to dedicate this work to '*Jesus Christ*'. I am greatly indebted to him for his unconditional love. Last, but not least, my thanks go to my parents for their great support, love and encouragement.

THANA UDOMSRIPAIBOON

*University of Southern Queensland*

*July 2017*

# Contents

# List of Figures

# List of Tables

# Acronyms & Abbreviations

| | |
|---|---|
| 5G | Fifth-generation wireless systems |
| ACL | Adaptive PAPR clipping level |
| APO | Adaptive PAPR Optimizer |
| ASK | Amplitude shift keying |
| BCJR | Bahl, Cocke, Jelinek, and Raviv |
| BER | Bit error rate |
| BPSK | Binary phase shift keying |
| BS | Base station |
| CCDF | Complementary cumulative distribution function |
| CDF | Cumulative distribution function |
| CP | Clipping scheme |
| CSI | Channel state information |
| dB | Decibel |
| DFE | Decision feedback equaliser |
| FFF | Fixed-forgetting factor |
| FITRA | Fast iterative truncation algorithm |
| FLOPs | Floating point operations |

| | |
|---|---|
| FS | Fixed-step-size |
| FSK | Frequency shift keying |
| HPA | High-power amplifier |
| HSUPA | High-speed uplink packet access |
| i.i.d. | Independent and identically distributed |
| ICI | Intercarrier interference |
| IDFT | Inverse discrete Fourier transformation |
| IIR | Infinite impulse response |
| LMS | Least mean square |
| LTE | Long term evolution |
| MIMO | Multi-input-multi-output |
| MU | Multiuser |
| OBR | Out-of-band ratio |
| OFDM | Orthogonal frequency-division multiplexing |
| PAPR | Peak-to-average power ratio |
| PDF | Power density function |
| PMP | Precoding modulation PAPR reduction |
| PSD | Power spectral density |
| QAM | Quadrature amplitude modulation |
| QPSK | Quadrature phase shift keying |
| RF | Radio frequency |
| RLS | Recursive least squares |
| SNR | Signal to noise ratio |

| | |
|---|---|
| SNDIR | Signal to noise plus distortion ratio |
| SSPA | Solid state power amplifier |
| VFF | Variable forgetting factor |
| VS | Variable step-size |
| WCDMA | Wideband code division multiple access |
| WLAN | Wireless local area networks |
| ZF | Zero-forcing |

| | |
|---|---|
| Bold letter: | A matrix (e.g. $\mathbf{x}$, $\mathbf{X}$) |
| Bold and italic letter: | A vector (e.g. $\boldsymbol{x}$, $\boldsymbol{X}$) |
| $\lvert\cdot\rvert$ | Absolute value operator |
| $\lVert\cdot\rVert$ | The Euclidean norm |
| $\lVert\cdot\rVert_\infty$ | The infinity norm |
| $(\cdot)^*$ | Conjugate operator |
| $(\cdot)^H$ | Conjugate transpose operator or a Hermitian transposition |
| $(\cdot)^\dagger$ | Pseudo-inversion operator |
| $(\cdot)^T$ | Transpose operator |
| $(\cdot)^{-1}$ | Inverse operator |
| $[\mathbf{x}]_{x,y}$ | Element in row $x$ and column $y$ of $\mathbf{x}$ |
| $\mathbf{I}_n$ | An $n \times n$ identity matrix |
| $\mathbf{0}_{n\times m}$ | An $n \times m$ matrix of all zeros |

| | |
|---|---|
| $\mathbf{1}_{n\times m}$ | An $n \times m$ matrix of all ones |
| $\mathrm{diag}(\boldsymbol{x})$ | Diagonal matrix with the diagonal elements are given by vector $\boldsymbol{x}$ |
| $\mathrm{sign}[\cdot]$ | The sign function |
| $E[\cdot]$ | Expectation operator |
| $\Gamma[\cdot]$ | Optimization operator |
| $Tr[\mathbf{x}]$ | Trace of a matrix $\mathbf{x}$ |
| $Pr[\cdot]$ | The probability function |
| $p(\cdot)$ | The power density function |
| $\mathfrak{F}[\cdot]$ | The discrete Fourier transform operator |
| $\mathfrak{F}^{-1}[\cdot]$ | The inverse discrete Fourier transform operator |
| $\mathbb{C}^{n\times m}$ | An $n\times m$ complex valued matrix |
| $R_{\mathbf{X}} \triangleq E[\mathbf{x}^{*}\mathbf{x}]$ | A covariance of $\mathbf{x}$ |
| $R_{\mathbf{X},\mathbf{Y}} \triangleq E[\mathbf{x}^{*}\mathbf{y}]$ | A cross-covariance of $\mathbf{x}$ and $\mathbf{y}$ |
| $\mathcal{CN}(m, R)$ | Circular symmetric complex Gaussian distribution with mean $m$ and covariance $R$ |
| $\mathcal{L}$ | The Lipschitz constant |
| $\otimes$ | Circular convolution |
| $n_c$ | Number of subcarriers |
| $\varepsilon$ | Number of the active subcarriers |

| | |
|---|---|
| $\varepsilon^{inac}$ | Number of the inactive subcarriers |
| $n_d$ | Number of channel taps |
| $n_p$ | Number of the clipping pulses per an OFDM signal duration |
| $n_r$ | Number of antennas at the user |
| $n_s$ | Length of transmitted data per one packet |
| $n_t$ | Number of antennas at the base station |
| $n_u$ | Number of users |
| $\mathbf{H}$ | Channel gain matrix |
| $\mathbf{G}_{ZF}$ | The zero-forcing precoding matrix |
| $\Omega_{ZF}$ | A normalization factor |
| $T_b$ | Time duration of an OFDM block |
| $T_s$ | Time duration of an OFDM symbol |
| $\Delta f$ | Distance between subcarriers in frequency domain |
| $\Delta q$ | Length of a quantized step of the adjustable PAPR clipping |
| $\Delta\theta$ | Phase change of the frequency component |
| $\Delta J$ | Jacobian's matrix |
| $f_c$ | The $c_{th}$ location of the subcarriers in frequency domain. |
| $\lambda$ | A signal attenuation factor |
| $\lambda_{PMP}$ | A regularization parameter of PMP scheme |
| $\lambda(\zeta)_{PMP}$ | The variable regularization parameter of the adjustable PMP scheme |

| | |
|---|---|
| $\lambda_{\beta_{CP}(\zeta)}$ | A variable level crossing rate of the adjustable clipping scheme |
| $Z_{PMP}$ | A number of FITRA iterations |
| $\omega$ | The frequency spectrum of the $k_{th}$ discrete-time domain |
| $\alpha$ | High peak level of PAPR signal of the IDFT signal |
| $\beta$ | Low peak level of PAPR signal of the IDFT signal |
| $\theta$ | Angle of the IDFT signal |
| $S[\omega]$ | Discrete power spectral density of the IDFT signal |
| $\zeta$ | Average of BER from users |
| $\beta(\zeta)$ | Adjustable PAPR reduction level |
| $\beta_{\max}$ | A maximum quantized PAPR level |
| $\beta_{\min}$ | A minimum quantized PAPR level |
| $\beta_{qt}$ | A percentage of the quantized PAPR level |
| $E_b / N_0$ | Signal to noise ratio |
| $\gamma_0$ | Signal to noise plus distortion ratio |
| $\gamma_u$ | Signal to noise plus distortion and interference ratio |
| $\kappa_\zeta$ | The maximum input dynamic range of the HPAs that have a linear response |
| $\tilde{x}_{\beta_{\max}}$ | The maximum adjustable clipped signal level |
| $\tilde{x}_{\beta_{\min}}$ | The minimum adjustable clipped signal level |
| $N_{qt}$ | Total number of the quantized step |
| $N_{rep}$ | Total number of the signal repetition |

| | |
|---|---|
| $J(\boldsymbol{w})$ | Cost function of weight vectors $\boldsymbol{w}$ |
| $J_{min}$ | The minimum error of the weight vector $\boldsymbol{w}$ |
| $\sigma_x^2$ | The variance of $x$ |
| $\sigma_{f[k]}$ | The variance of the clipping noise |
| $\boldsymbol{w}^o$ | The optimum weight vector |
| $\mu$ | A fixed-step-size of the LMS algorithm |
| $\mu[k]$ | A variable step-size of the LMS algorithm |
| $L$ | Length of the Adaptive PAPR Optimizer |
| $\chi$ | A fixed-forgetting factor |
| $\chi[k]$ | A variable forgetting factor |
| $\chi^2$ | An up-crossed process at the variable clipping level |
| $\delta$ | A regularization parameter of the RLS algorithm |
| $\varpi$ | A ratio of the adjustable clipping level |
| $k[k]$ | A Kalman gain of the RLS algorithm |
| $\Theta[k]$ | An inverse correlation matrix of the RLS input signal |
| $f[k]$ | Clipping noise of the PAPR reductions in the discrete-time domain |
| $F[\omega]$ | Clipping noise of the PAPR reductions in the frequency spectrum domain |
| $BW$ | The OFDM bandwidth |
| $\beta_{CP}$ | The fixed- clipping level of the clipping scheme |
| $\beta_{PMP}$ | The fixed- clipping level of the PMP scheme |

| | |
|---|---|
| $\beta_{CP}(\zeta)$ | The adjustable clipping level of the clipping scheme |
| $\beta_{PMP}(\zeta)$ | The adjustable clipping level of the PMP scheme |
| $\tau$ | Total pulse duration of the clipping signal |
| $P_e$ | The probability of the symbol error rate |
| $g(\boldsymbol{x})$ | A real-valued non-smooth convex function in the FITRA algorithm |
| $h(\boldsymbol{x})$ | A real-valued smooth convex function in the FITRA algorithm |

# Chapter 1

# Introduction

This thesis addresses the problems that result from high peak-to-average power ratio (PAPR) levels in a multi-antenna communication system by devising a signal shaping method.

Large-scale multi-input-multi-output (MIMO) systems are likely to be adopted as the technology for the fifth-generation wireless systems (5G). Such systems are also called massive MIMO, very large MIMO, hyper-MIMO, or full-dimension MIMO [1-2]. The 5G system must be devised to accommodate the dramatic growth of mobile phones, tablets, laptop computers, smart watches, and other wireless devices. Having many advantages such as high communication reliability, high energy efficiency, and simple signal processing, large-scale MIMO is popular as a topic for research and exploitation [3-8].

In Figure 1.1, orthogonal frequency-division multiplexing (OFDM) together with MIMO has been adopted by present and future wireless local area network (WLAN) standards such as IEEE 802.11a/g, IEEE 802.11n, and IEEE 802.11ac. It is a powerful multi-carrier modulation technique for gaining the bandwidth efficiency of the wireless communication systems. Moreover, one of the main reasons to use OFDM is to increase the robustness to withstand frequency selective fading and narrowband interference. As a result, the advantages of OFDM make this technology a promising alternative for digital broadcasting and communications [9-12].

The main disadvantage of an OFDM system is the large value of the high PAPR that results from the superposition of all subcarrier signals by an inverse discrete

Fourier transformation (IDFT) process. High PAPR then causes waveform distortion because of any nonlinear amplifier characteristics, in particular the constrained output power. To resolve this problem, the transmitter would need to employ an expensive amplifier in each transmitting antenna.

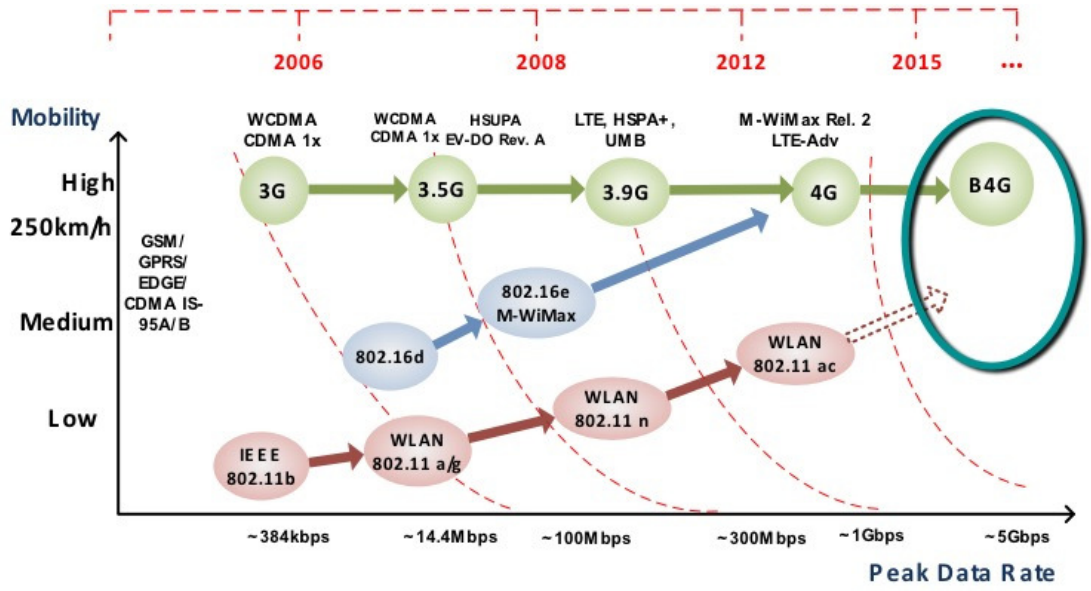


Figure 1.1 [1]Evolution of wireless standards in the last decade (sourced from [13]).

Nevertheless, a hundred antennas or more may have to be installed with a great number of amplifiers for the next generation of the WLAN. As a consequence, two negative effects will be associated with the multiple antennas of OFDM systems:

1. *High power consumption*: The greatest power consumption in the OFDM systems is in the power amplifiers as shown in Table 1.1. They typically consume about 80% of the power budget of a base station (BS). Out of concern for the transmitting power, we wish to reduce the output signal to a small proportion of the maximum output power of the amplifiers. A small reduction of an individual transmitted power maps to a huge power reduction when a very large number of antennas are involved. Reducing that power is a key focus of this research. On the other hand, the signal processing's proportion of the power budget is only around 5% [14].

[1] B4G stands for Beyond the Fourth-Generation.

Table 1.1 Conventional BS average power consumption distribution (sourced from [14]).

| **Appliances** | **Estimated Standard Power (%)** |
|---|---|
| Power Amplifiers | 80 |
| Air Conditioning | 10 |
| Signal Processing | 5 |
| Power Supply | 5 |

2. *High cost of the amplifiers in the systems*: Even though high values of PAPR have long been a problem in a single antenna of the OFDM transmission, the costs of the amplifiers are increased in proportion to the number of antennas in massive antenna systems. The use of expensive RF amplifier components is an undesirable way to solve this problem in the future [15-16].

In consequence, many researchers have presented a variety of digital processing methods for reducing PAPR, both to tackle the high power consumption and the high price of the amplifiers of a large number of antenna systems [17-18].

## 1.1 Background

PAPR problems resulting from OFDM have long been known. Although there are remedies for single antenna systems, they become especially serious when an OFDM system is applied in multiple antenna systems. This problem negatively affects the high-power amplifiers (HPAs) at the front end of each antenna.

To keep the desired information from the original signal in each HPA, the system should be designed to use as much of its dynamic range as possible. But when the uncorrelated multi-channel input signals combine to produce a peak amplitude, this would take the high power amplifiers into a nonlinear region [14]. This will cause many negative effects causing nonlinear distortions, both out-of-band spectral and in-band distortions. The out-of-band spectral affects other operators operating in the adjacent frequency bands whereas; the in-band distortion degrades the symbol error rate (SER) performance [19].

In the past, there have been many efforts to deal with the PAPR problems on a large-scale MIMO-OFDM system, resulting in numerous articles. In [21], the integration between a multiuser (MU) precoding, an OFDM modulation and a PAPR reduction (or a PMP scheme) was presented, where its aim was to reduce the large PAPR. The fast iterative truncation algorithm (FITRA) was devised by Studer et.al. for shrinking the high level of PAPR. In [22], by using a constant envelope precoding, the transmit power and hence the high PAPR of the large antenna of the BS is reduced efficiently. In [23], the weakest eigenchannels are employed for decreasing PAPR. It is utilised with least squares iterative for estimation the high peak level of the transmitted signal. Lastly, in [24], antenna reservation is used for clipped signals to compensate by transmitting correction signals on a set of reserved antennas.

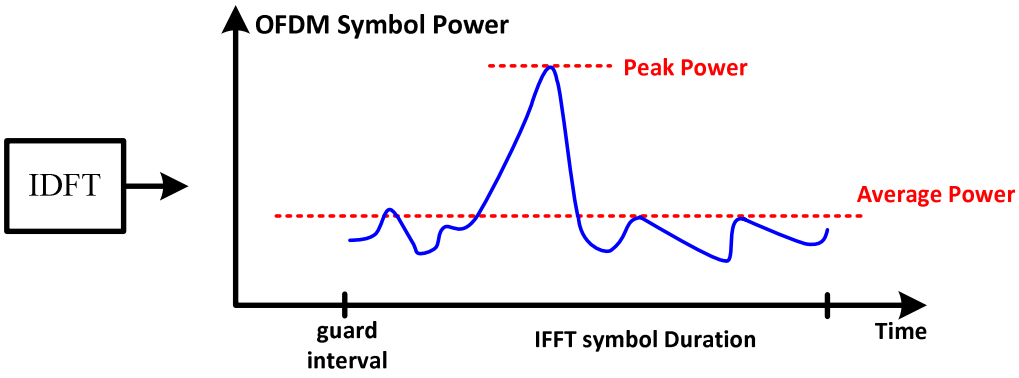


(a) The high peak power of PAPR signal in one subcarrier on OFDM system.

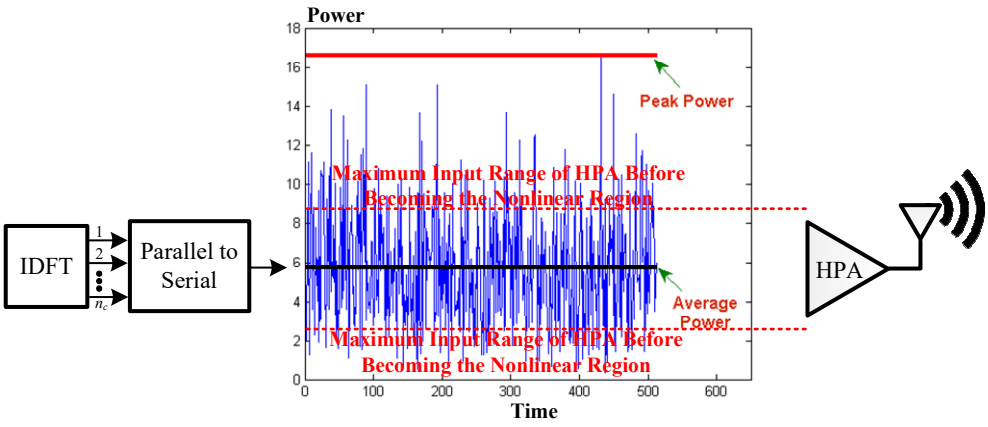


(b) The high peak power of PAPR signal in the multiple carriers on OFDM systems.

Figure 1.2 High dynamic ranges in OFDM symbols taken from [19].

A method that is frequently used to address large PAPR is a fixed level clipping technique [25, 27]. As shown in Figure 1.3, it is located after the IDFT and before the power amplifiers. This leads to in-band distortion in the form of intermodulation terms and spectral regrowth into the adjacent channel [21-24, 28].

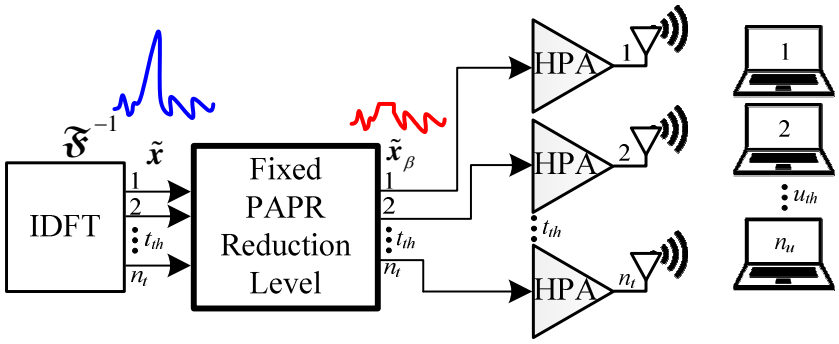


(a) The area of the conventional PAPR reductions in the downlink large-scale MIMO-OFDM system.

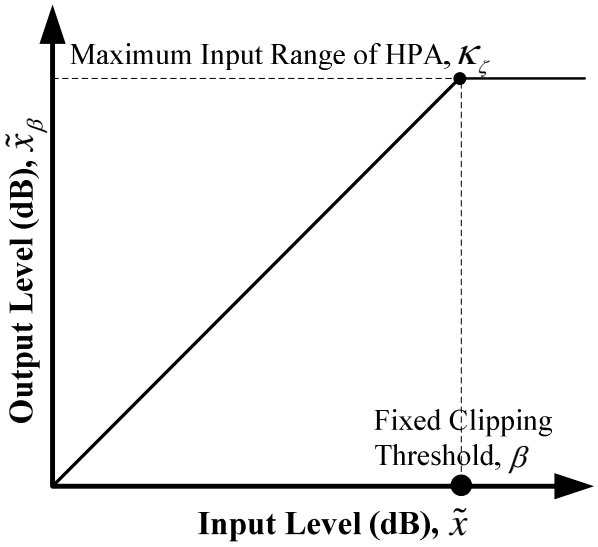


(b) The fixed PAPR reduction's input/output characteristic.

Figure 1.3 The state of art technology of PAPR reductions.

Figure 1.4 shows in-band distortion by this clipping method. The transmitted signal is assumed to be truncated above 3.5 dB with clip durations $t_1$, $t_2$,… The values $d_1$, $d_2$,…, $d_8$ are the means of the sums of squared errors of the data sequence in the frequency domain. As a result, these clipped signals create adjacent channel leakage, which causes power to leak outside the system's own channel, which is called out-of-band distortion. Moreover, they also put unwanted power within the

system's own channel, which is called in-band distortion [19, 29]. Therefore, such PAPR reduction schemes will increase the error rate at the receivers.

The present fixed clipping PAPR reduction schemes give no means of adapting the system to a varying condition that is the situations of wireless local area network channels in a cell. This present research is based on devising an optimiser that can adapt the signal shaping to minimise the symbol error rate. This error rate can be determined from the feedback channel that transmits the channel state from the receiver back to the transmitter.

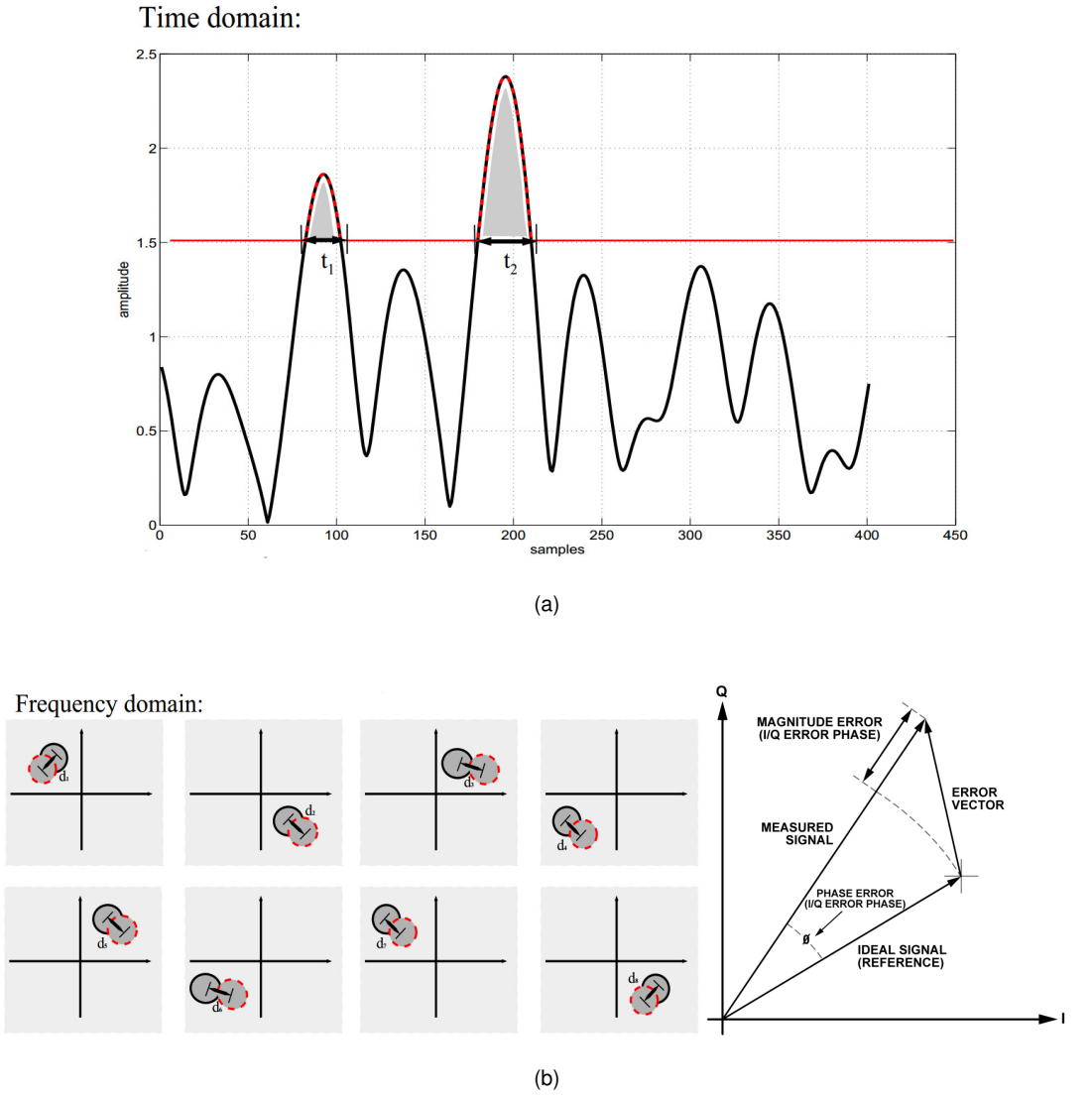


(a)

(b)

Figure 1.4 (a) The distorted OFDM signal in time domain taken from [19]. (b) The corresponding impact on the subcarrier signalling points in the frequency domain (sourced from [19] and [29]).

Although there are PAPR reduction schemes, they have no tools to adjust the clipped signals from them. This interesting point brings the idea of the innovative

tool called the Adaptive PAPR Optimizer (APO) combined with the variable level PAPR clipping technique. Moreover, by the benefit of the channel state information (CSI), it could be adapted itself relating to the network channel by using users' symbol error rate (SER) feedback [30-33].

The main goal of this project is to reduce the problems of the existing PAPR reductions by equalising the clipped signal before sending to all antennas. By this technique, the equalised signals are compensated by the proposed tool to shape them similar to the unclipped signal as possible. Finally, the area of the proposed method should be located as shown in Figure 1.5, and its expected signal could be shown in Figure 1.6 respectively.

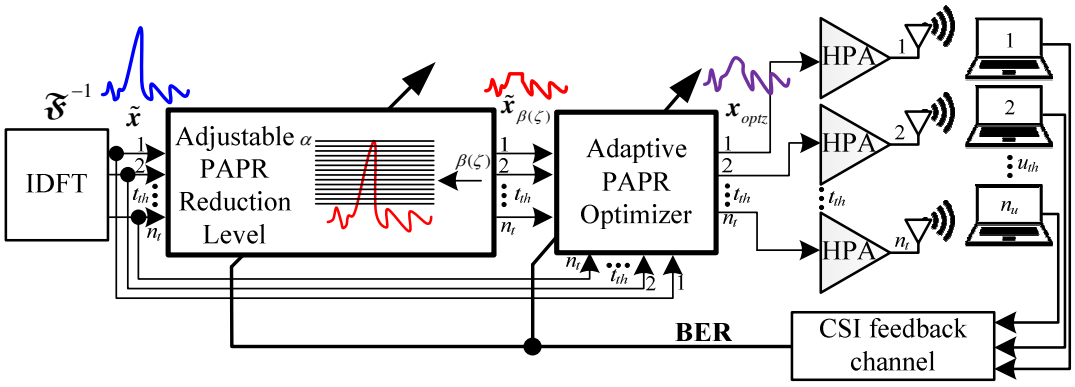


(a) The area of the proposed technique on the downlink large-scale MIMO-OFDM system.

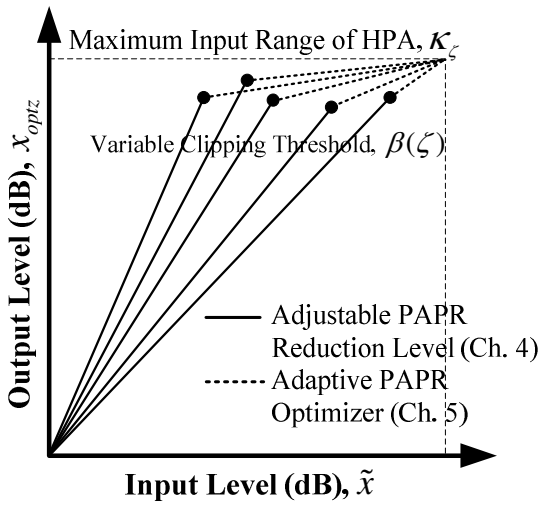


(b) The proposed technique's input/output characteristics.

Figure 1.5 The proposed technique of the adjustable PAPR reductions.

This thesis focuses on decreasing the effects of both in-band and out-of-band distortions from the existing PAPR reduction methods for the large-scale MIMO-OFDM systems, along with a generalised transmission scheme and theoretical studies. The research outcome of this project is able to be further implementation to enhance the wireless network throughput and SER performance of the next generation in wireless communication systems.

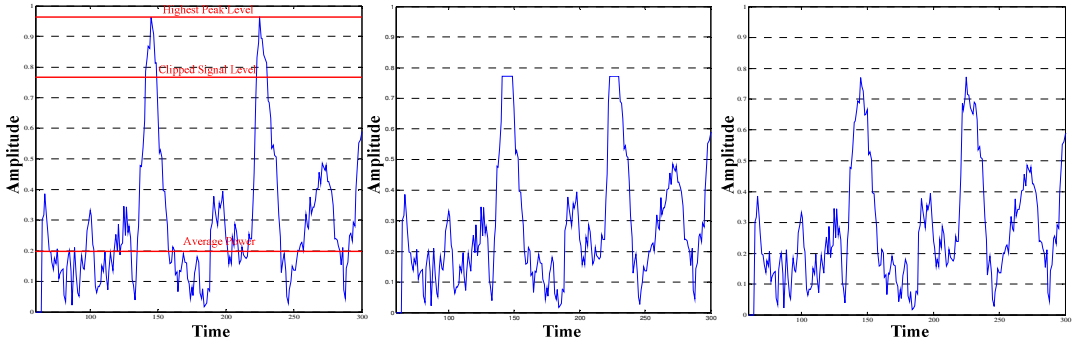


(a) The original signal (b) The clipped signal (c) The expected signal

Figure 1.6 An APO retains the transmitted signal before sending.

## 1.2 Motivation and Goals

Even though the negative effects of PAPR on OFDM system and the PAPR reductions are well understood, the literature on the similar analysis for equalising the clipped signal is low. Practically, there is no existing material to optimise the clipped signal for PAPR reduction methods. In doing this, it is necessary to know if any of the PAPR reduction methods available for OFDM could be applied for the proposed technique and if so what are the modifications required. Furthermore, what are the negative impacts of the proposed scheme? How could it be improved by other techniques? These questions need to find answers to achieve the goals to mitigate the PAPR problems of the large-scale MIMO-OFDM systems.

In this project, a study is conducting on the negative effects of PAPR. It also seeks to find the new technique to relieve them. The main goals of this thesis are:

1. To establish a simulation setup in MATLAB to analyse PAPR reductions on the large-scale MIMO-OFDM system;

2. To analyse the negative effects of PAPR in the large-scale MIMO-OFDM system;
3. To invent a new method to relieve the PAPR problems;
4. To design an assistant tool for PAPR reduction to equalise the clipped signal; and
5. To propose and analyse the new versions of both a clipping scheme (CP) and a PMP.

## 1.3 Innovation and Contribution

This thesis provides many innovations and a research project to the PAPR reduction field to improve the SER performance in the large-scale MIMO-OFDM systems. The innovative works of this thesis are:

- Analysis of the negative effects of PAPR in the large-scale MIMO-OFDM systems.
- Analysis of the symbol error rate of the proposed technique.
- Analysis and designing of the new versions of the PAPR reduction schemes.
- Designing a new tool to equalise the clipped signal from PAPR reductions.
- Designing some algorithms that can adapt themselves relating to the channel circumstance of the networks to mitigate the PAPR problems in the large-scale MIMO-OFDM systems.
- Academic publishing a research paper to contribute the proposed techniques in the international conference.

## 1.4 Thesis Outline

This thesis is organised as follows. In Chapter 2, a literature review is performed by the initial equations of large-scale MIMO-OFDM systems. The PAPR problems with the ODFM fundamental theory are also discussed. The negative effects imposed by non-linearity of the HPAs will be considered in this Chapter. Chapter 3 surveys existing cutting-edge methods of the PAPR reductions considering also the weak points of each PAPR reduction technique. Chapter 4 introduces my own novel PAPR

reduction schemes. They are modified by the conventional PAPR reductions based on a CP and a PMP technique. A new tool to assist the implementation of the proposed PAPR reductions in Chapter 4 is presented in Chapter 5. Moreover, the derivation of this tool will be examined. In Chapter 6, the proposed techniques will be compared with the existing PAPR reduction techniques by all simulation results. Finally, the conclusions and future works of the research are presented in Chapter 7. Figure 1.7 illustrates the organisation of this thesis.

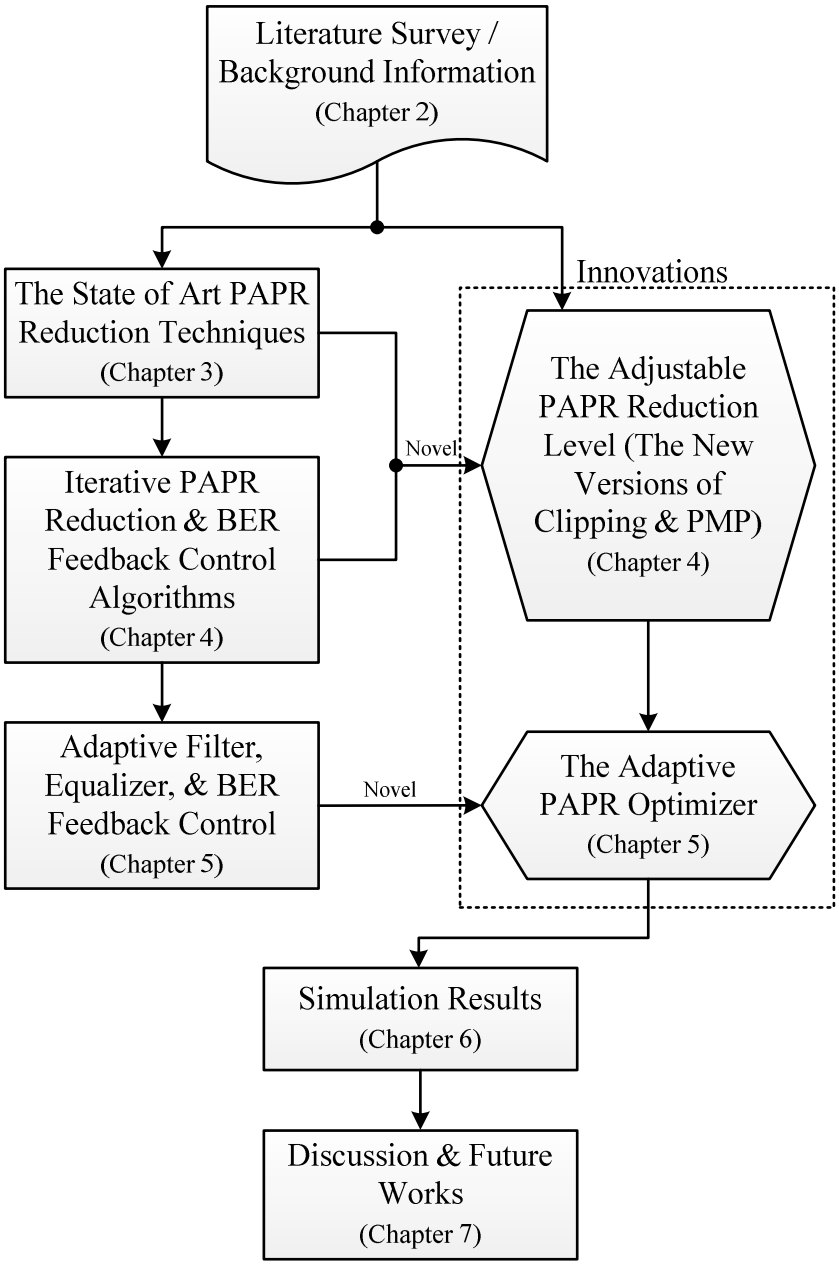


Figure 1.7 The organization of the thesis.

# Chapter 2

# Background Information

The main aim of this chapter is to provide an overview of the large-scale MIMO-OFDM systems. Moreover, the negative effects of the nonlinearities of amplification are also presented. The high peak of amplitude in transmitted signals causes ill-behaved power amplifiers in the systems such as in-band/out-of-band distortions, spectral regrowth effect, and adjacent channel interference. Finally, both benefits and drawbacks of the OFDM system are given at the end of this chapter.

An overview of the large-scale MIMO systems will be presented from 2.1 to 2.3 respectively. Then, revision of OFDM systems is presented in section 2.4. Finally, the nonlinearities of amplifiers are represented in section 2.5.

## 2.1 An Overview of MIMO Systems

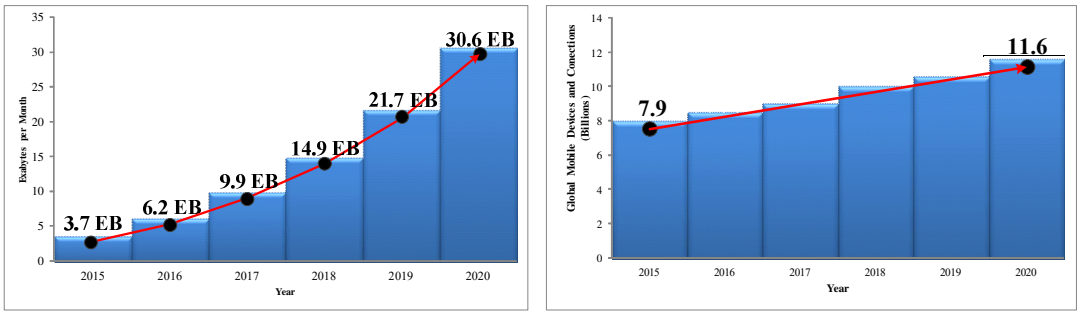


(a) Global mobile data traffic. (b) Global mobile devices and connections growth.

Figure 2.1 Demand for mobile data traffic and number of connected devices sourced by [36].

Data traffic has rapidly increased during the last few years, with growing numbers of wireless devices being connecting to mobile networks worldwide. This is one of the primary contributors to global mobile traffic increasing. Figure 2.1 shows the demand for mobile data traffic and the number of mobile devices. The mobile data traffic can be expected to reach to 30.6 exabytes per month by 2020, which is the 5 times increasing over 2016. Moreover, the expected number of mobile devices and connections will be around 11.6 billion by 2020. For these reasons, this demand requires the new technology to support its growth in the future [34-36].

$$\textit{Throughput} = \textit{Bandwidth}(\text{Hz}) \times \textit{Spectral Efficiency}(\text{bits/s/Hz}) \qquad (2.1)$$

As shown in (2.1), new technologies are required to gain the throughput for increasing either bandwidth or spectral efficiency. In this thesis, the technology for increasing the spectral efficiency is exploited. A common way to increase the spectral efficiency is the use of the multiple antennas at the transmission [37].

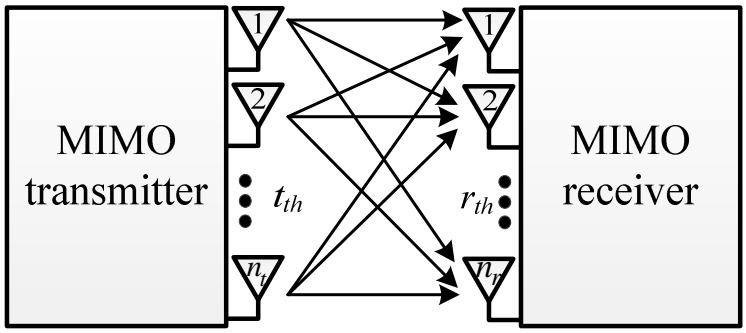


Figure 2.2 Point-to-point MIMO system.

In wireless communication systems, both multipath propagation and large obstacles attenuate transmitted signal by fading and shadowing respectively. By these problems, they affect the reliability of the communication between the transmitter and the receiver. The MIMO technique has been exploited to enhance the reliable communication with diversity antennas. In addition, many data streams can be sent by multiple antennas to gain the communication capacity in wireless channels, $\mathbf{H}$. For these reasons, the transmission with MIMO technology has attracted attention in wireless communications during the last decade and also been emerged into many new generation wireless standards (e.g., LTE-Advanced, 802.16e M-WiMax, WLAN 802.11ac) [2-3].

## 2.2 The MU-MIMO Systems

To enhance the wireless communications, the MU-MIMO has been shifted from MIMO to gain the spatial multiplexing among many users, which are concurrently served by the multiple antennas at a BS. Even though each user has a single antenna ($n_r = 1$), the spatial multiplexing gain can be achieved by MU-MIMO systems [38]. The important users' reasons are the limited physical size and cheap price requirements of the mobile devices. Some terminals cannot exploit the multiple antenna technologies, whereas the BS can be supported it. Moreover, the MU-MIMO is able to solve the poorly-behaved channels by using scheduling schemes. Also, the line-of-sight propagation, which causes significant reduction of the performance of MIMO systems, can be solved by MU-MIMO systems. Therefore, MU-MIMO has been becoming a hot research topic nowadays [38-43].

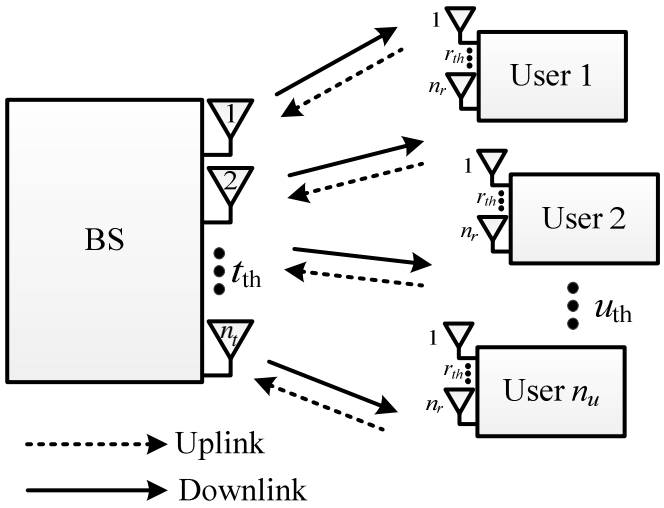


Figure 2.3 MU-MIMO systems.

The advantages and disadvantages of the MU-MIMO systems can be summarily described as sub-topics as follows:

- *MU interference*: the interference among all users significantly degrades the over performance of a given user. Many interference cancellation techniques can be used to solve this problem such as maximum likelihood MU detection for the uplink, dirty paper coding techniques for the downlink, and interference alignment [44-46]. Unfortunately, these techniques have high computational complexity and also are complicated.

- *The CSI's addition*: the BS needs to process the received signals coherently with CSI to achieve a high spatial multiplexing gain. It requires the accurate and timely addition of CSI and has been challenging for all researchers in this issue [32].
- *Users' schedules*: the user's scheduling gains the cost of the system implementation. Due to the limited time and frequency resource, the BS serves many users at the same time. So, some groups of the user are only chosen by BS. This can be challenging, especially the high-demand for data traffic growth scenario [47].

## 2.3 The Large-Scale MIMO Systems

The large-scale MIMO is a type of MU-MIMO systems, where the number of BS antennas and the number of users are large. The more antennas the BS is installed with, the more degrees of freedom are afforded. Additionally, many terminals can simultaneously communicate with the same frequency resource by different time slots. As a result, a gigantic total throughput can be gotten with the large-scale of antennas and ordinary signal processing methods. On the other hand, it also increases the complexity because of the high signal dimensions. The primary inquiry is to reduce the complexity signal processing and high-cost hardware implementation with the achievement of the huge multiplexing gain on a large scale multiple antenna system. In the large-scale MIMO system, each antenna is expected to install a cheap radio frequency module (e.g., simple processing, a low-power amplifier) [3].

The primary advantages of the large-scale MIMO systems are [5, 48]:

- *Gigantic spectral efficiency and high communication reliability*: by adding with $n_t$ – antenna BS and $n_u$ – single antenna users, the communication system obtains increased spectral efficiency and very high communication reliability.
- *High energy efficiency*: for the large-scale MIMO transmission in uplink, a very high array gain can be reached by the coherent combining. It permits for the substantial reduction in transmitted power of each user. For the large-scale MIMO transmission in downlink, each terminal can be served with the

focusing energy by a BS, where each user is spatially located. Therefore, the radiated power can be increased by an order of magnitude with the large-scale of antenna arrays. Then, all users can obtain high energy efficiency. In the case of the fixed number of terminals, doubling the number of BS antennas, and reducing the transmit power by half, the radiated energy efficiency is doubled, whereas the original the spectral efficiency is still maintained.

- *Low complexity of the signal processing*: in the large-scale MIMO circumstances over the number of terminals, the favourable propagation is served while the channel vectors between a BS and terminals are nearly orthogonal. Moreover, the negative effects from both inter-user interference and thermal noise can be reduced by simple signal processing (e.g., linear precoding in the downlink, linear decoding in the uplink) under the favourable propagation. For this reason, all simple linear processing methods are optimal.

  Another advantage of the large-scale MIMO systems is channel hardening. The off-diagonal terms of the $\mathbf{H}^{H}\mathbf{H}$ matrix become dramatically weaker compared to the diagonal terms as the size of the channel gain matrix $\mathbf{H}$ increases. By this reason, the negative effects of the small-scale fading are sharply eliminated. For the large-scale fading, the simple signal processing methods such as system scheduling, power control, etc., are able to solve all problems from the large-scale fading as well.

For all the above reasons, they may drive the large-scale MIMO to be one of the promising candidate technologies for 5G of the wireless systems. Nowadays, it is becoming a hot topic for researchers in a wireless communication field. Moreover, it can be compatible with modern digital multi-carrier modulation methods such as OFDM, millimetre-wave, or heterogeneous cellular network. Then, the large-scale MIMO worked with an OFDM is chosen for studying in this thesis.

### 2.3.1 Zero-Forcing Precoding

In this thesis, the downlink transmission of the large-scale MIMO systems is focussed. The simple zero-forcing (ZF) processing is used for precoding the 16-*QAM* modulated vector, $\boldsymbol{s} \in \mathbb{C}^{n_u \times 1}$, as

$$\boldsymbol{x} = \mathbf{G}_{ZF}\boldsymbol{s}, \tag{2.2}$$

where $\boldsymbol{x} \in \mathbb{C}^{n_t \times 1}$ is the precoded vector and $\mathbf{G}_{ZF} \in \mathbb{C}^{n_t \times n_u}$ is the ZF precoding matrix.

The matrix $\mathbf{G}_{ZF}$ is employed for eliminating inter-user interference. It can be represented as

$$\mathbf{G}_{ZF} = \Omega_{ZF}\mathbf{H}^{\dagger} = \Omega_{ZF}\mathbf{H}^{H}\left(\mathbf{H}\mathbf{H}^{H}\right)^{-1}, \tag{2.3}$$

where [1] $\Omega_{ZF}$ is the normalization factor, $\left(\cdot\right)^{H}$ is a Hermitian transposition, and $\mathbf{H}^{\dagger}$ is the pseudo-inversion of $\mathbf{H}$.

Vice versa, the $\Omega_{ZF}$ can be shown in the term of $\mathbf{G}_{ZF}$ as

$$\Omega_{ZF} = \sqrt{\frac{n_u}{Tr\left[\mathbf{G}_{ZF}^{H}\mathbf{G}_{ZF}\right]}}, \tag{2.4}$$

where $Tr\left[\cdot\right]$ is a trace operator [49].

## 2.4 Orthogonal Frequency Division Multiplexing

OFDM is a kind of the frequency division multiplexing modulation. It is utilised as a digital multi-carrier modulation method. A large number of orthogonal subcarriers, $n_c$, are employed to transport the precoded data, $\boldsymbol{x}$. This precoded data is then divided into many several parallel streams by using a serial-to-parallel converter to each $n_c$ subcarrier. Each subcarrier is [2] orthogonal to each other (or they are totally independent of one anther). Finally, the data stream is converted to frequency

[1] The normalization factor is used for averaging the fluctuations in the transmit power.

[2] For the case of discrete time, two subcarriers are orthogonal as: $\sum_{c=0}^{n_c} \cos(2\pi ca / n_c)\cos(2\pi cb / n_c) = 0,\ a \neq b.$

domain by employing an inverse discrete Fourier transform (IDFT). In this stage, each IDFT creates the high peak amplitude of PAPR into the data stream after reverting into a single data stream, $\tilde{\boldsymbol{x}} \in \mathbb{C}^{n_t \times 1}$ [11, 15].

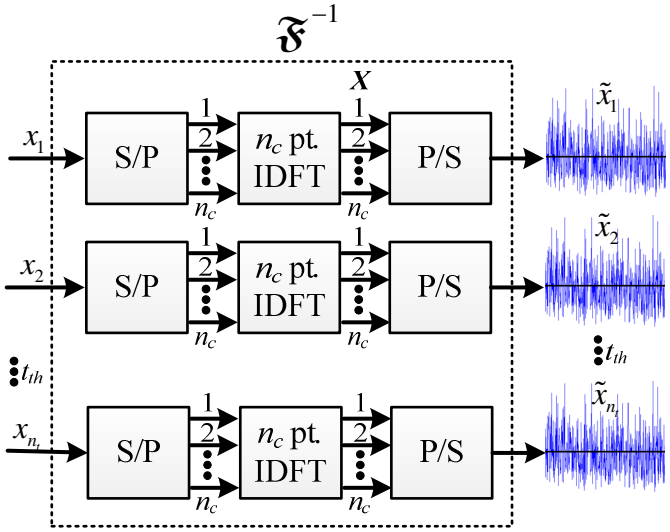


Figure 2.4 Block diagram of an OFDM system for $n_t$ antennas.

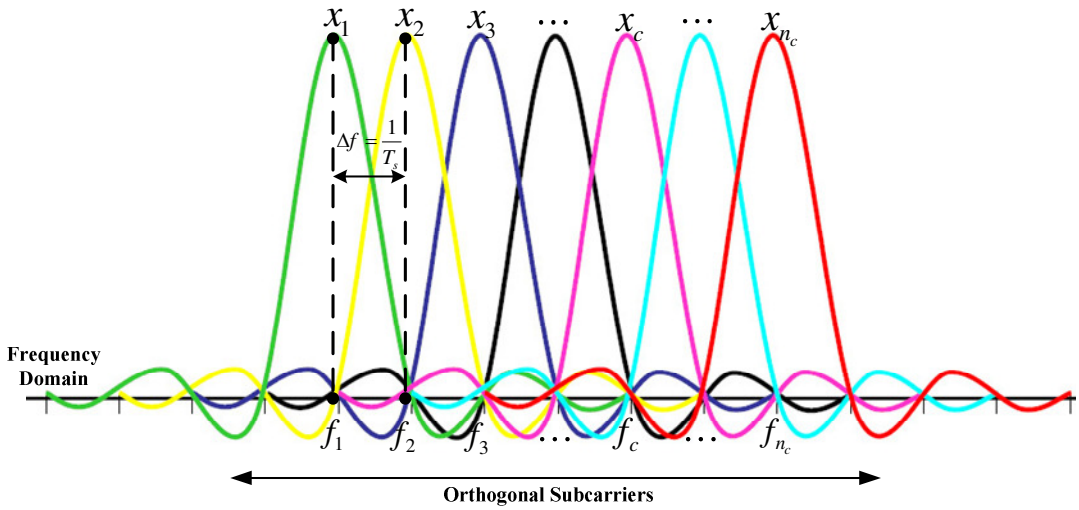


Figure 2.5 The OFDM spectrum.

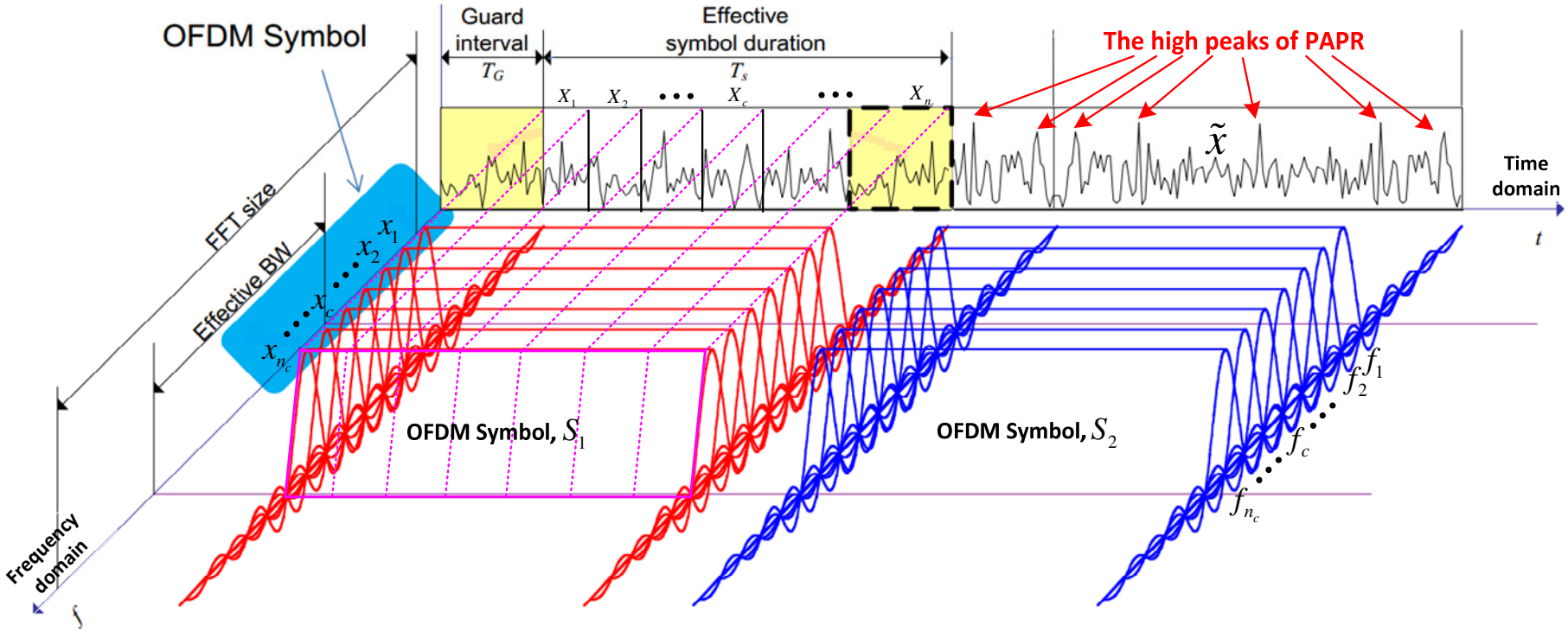


Figure 2.6 Time/frequency-domain description of OFDM symbols (adapted from [50]).

Figure 2.4 shows the block diagram of the IDFT process that is used for $n_t$ antennas. Also, both Figures 2.5 and 2.6 show the OFDM spectrum in frequency domain relating to the time domain. A block of $n_c$ data complex symbols is defined by $X_c$. Then, the OFDM modulated signal can be represented as

$$x(t) = \frac{1}{\sqrt{n_c}} \sum_{c=-\frac{n_c}{2}}^{\frac{n_c}{2}} X_c e^{j2\pi f_c t}, \quad (1 < t \le T_s), \tag{2.5}$$

where $T_s$ is the duration of one OFDM symbol, the distance between subcarriers in the frequency domain can be symbolised as $\Delta f = 1/T_s$. Each subcarrier is located as

$$f_c = \frac{c}{T_s}, \quad (1 < c \le n_c). \tag{2.6}$$

To maintain the orthogonality among all OFDM symbols, $x(t)$ is needed to sample in every $\Delta f = T_s / n_c$. Therefore, [3]the sampled signal can be shown as the mathematical expression as

$$\tilde{x} = x[kT_s] = \sum_{c=-\frac{n_c}{2}}^{\frac{n_c}{2}} X_c e^{j2\pi f_c \frac{kT_s}{n_c}}, \tag{2.7}$$

where $c = f_c T_s$, and $f_1 = 0$, and then $\tilde{x}$ can be shown as

$$\tilde{x} = \mathfrak{F}^{-1}\left[x\right] = \sum_{c=-\frac{n_c}{2}}^{\frac{n_c}{2}} X_c e^{j2\pi \frac{kc}{n_c}}, \tag{2.8}$$

where $\mathfrak{F}^{-1}\left[\cdot\right]$ is an IDFT operator [50].

The main advantages of OFDM system can be listed as [2, 8-11, 51]:

- *More efficient assistance in multipath environments*: the high-speed serial data will be transmitted by dividing up into many much lower-speed serial data signals. This technique makes the bit or symbol periods longer, therefore multipath time delays have less of an impact. In order to resist the multipath

[3] Because of (2.4), an average power of the OFDM symbol, $1/\sqrt{n_c}$, may be skipped (2.7) and (2.8) respectively.

effects, the system needs to add more subcarriers over a wider bandwidth. It means that the higher frequencies can be used with fewer multipath effects.

- *Low-complexity processing*: By the benefits of the advances in a digital signal processing, the low- complexity processing can be used with a simple and efficient implementation.
- *Low-complexity at receivers*: for the above reason, it can reduce the physical size of the terminals. Furthermore, it can decrease the power consumption on the wireless devices.
- *A variety of the modulation techniques*: for a given chunk of spectrum space, the many modulation techniques are used for widely varying maximum data rates. Simple digital modulations can be employed on OFDM such as amplitude shift keying (ASK), frequency shift keying (FSK), binary phase shift keying (BPSK), quadrature phase shift keying (QPSK), and quadrature amplitude modulation (QAM).

On the other hand, the disadvantages can also be listed as:

- *Doppler shifts*: a special form of multicarrier modulation by OFDM systems is more sensitive to Doppler spreads than the single-carrier schemes. They influence the carrier frequency offsets, affecting in intercarrier interference (ICI).
- *Synchronisation accuracy*: another problem of OFDM is the inaccurate synchronisation. Even though the effective OFDM synchronisation enables the data error rates to be kept to a minimum, error rates are exponentially increased by this problem.
- *Noise sensitiveness*: OFDM is sensitive to high amplitude impulsive noise because the noise energy spreads among all OFDM subcarriers increasing bit error rate (BER) in the overall systems.
- *The high amount of PAPR*: the main drawback of an OFDM signal is a high peak of PAPR. Subsequently, the transmitted signal needs to gain itself with the expensive power amplifiers. That means the greater efficiency in the radio frequency (RF) power amplifiers, the higher cost and the more power consumption in the systems.

# 2.5 Power Amplifier - Nonlinearities

The results of this thesis are based on simulation. The introduction and overview of RF amplifiers are given in order to provide an understanding of the important theories. Then, those fundamental theories will be written for the simulation program to study its impact on PAPR problems.

An ideal output signal from amplifiers should take any input signal and proportionally gain the output amplitude. In other words, the output should be scaled by the input accurately. Nevertheless, in practical systems, amplifiers cannot scale output signal as the same characteristics as the input signal perfectly. Due to many negative aspects the amplifiers' characteristics are unavoidably affected. One of them is the ill-behaved signals of PAPR.

Figure 2.7 illustrates a mathematical response of the amplifiers, while Figure 2.8 (a) shows the negative effect of a non-linear amplification of signals in the time domain, and Figure 2.8 (b) shows the typical response of an ideal amplifier compared with a real amplifier [52].

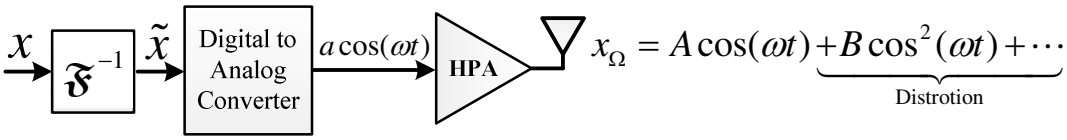


Figure 2.7 A mathematical response of a non-linear power amplifier.

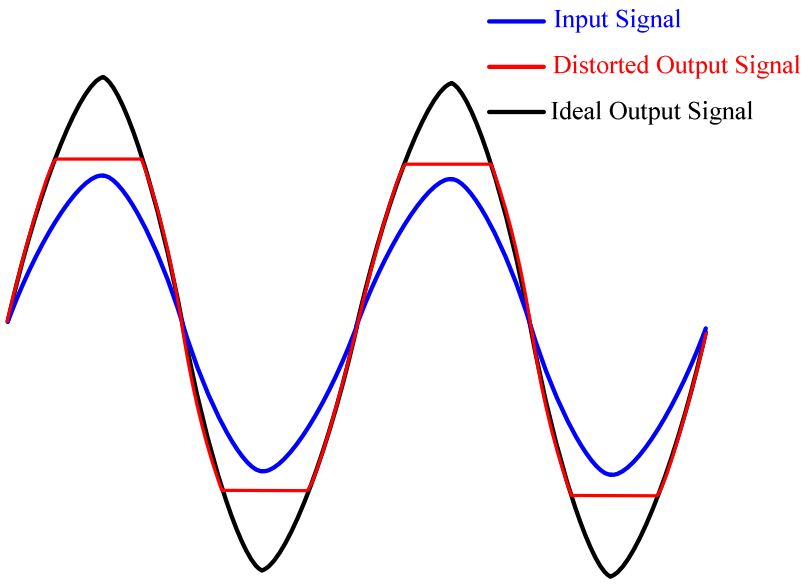


(a) A distortion in a non-ideal amplifier in the time domain.

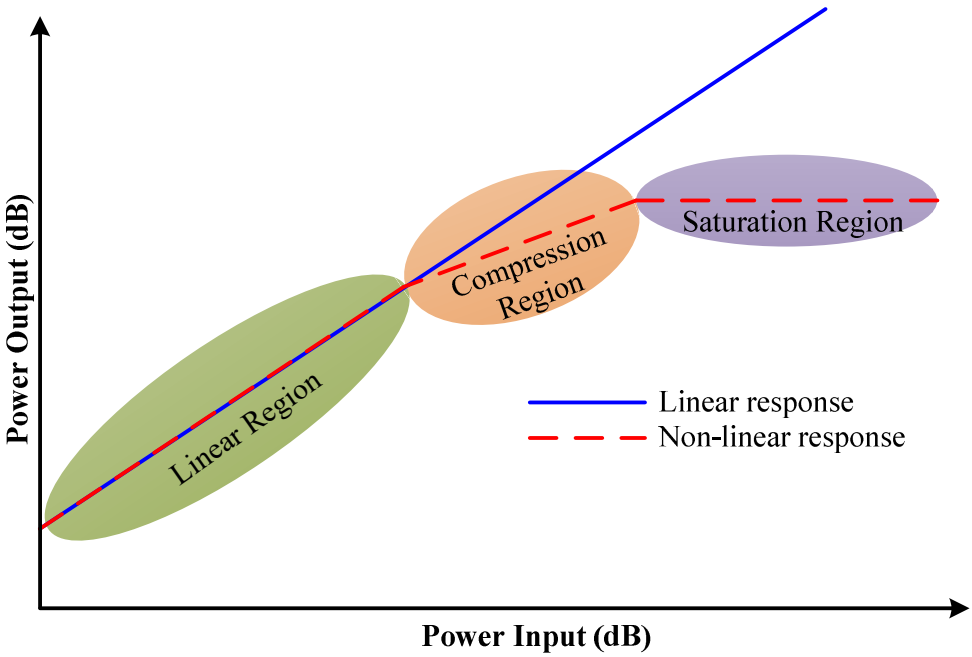


(b) An amplification response of both linear and non-linear amplifiers taken from [53].

Figure 2.8 An effecting of a non-linear amplifier.

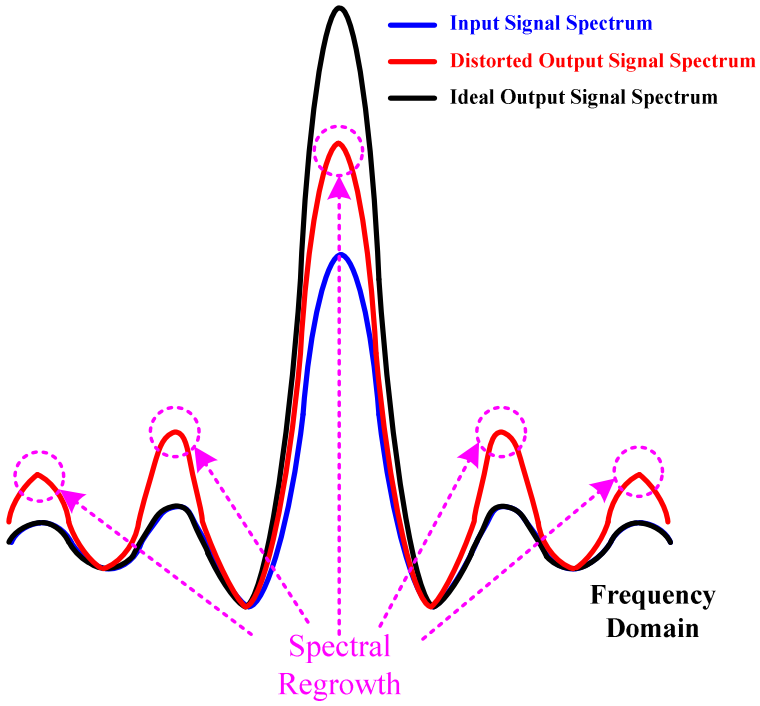


Figure 2.9 The spectral regrowth effect in an OFDM spectrum.

Figure 2.8 (b) shows that initially the gain of the amplifier is linear. For this region, the output signal is proportional to the input without any distortion. In the compression region, the response has a non-linearity and therefore there is some distortion. Finally, in the saturation region, the output amplitude is truncated

independent of the magnitude of the input gain [53]. Both compression and saturation regions will expand each spectral OFDM signal adding up more frequencies in the output signal. Figure 2.9 shows that all frequency spectrums are plotted from signals in Figure 2.8 (a). This leads both an out-of-band distortion and an in-band distortion in the received signal as shown in Figure 2.10 respectively [54].

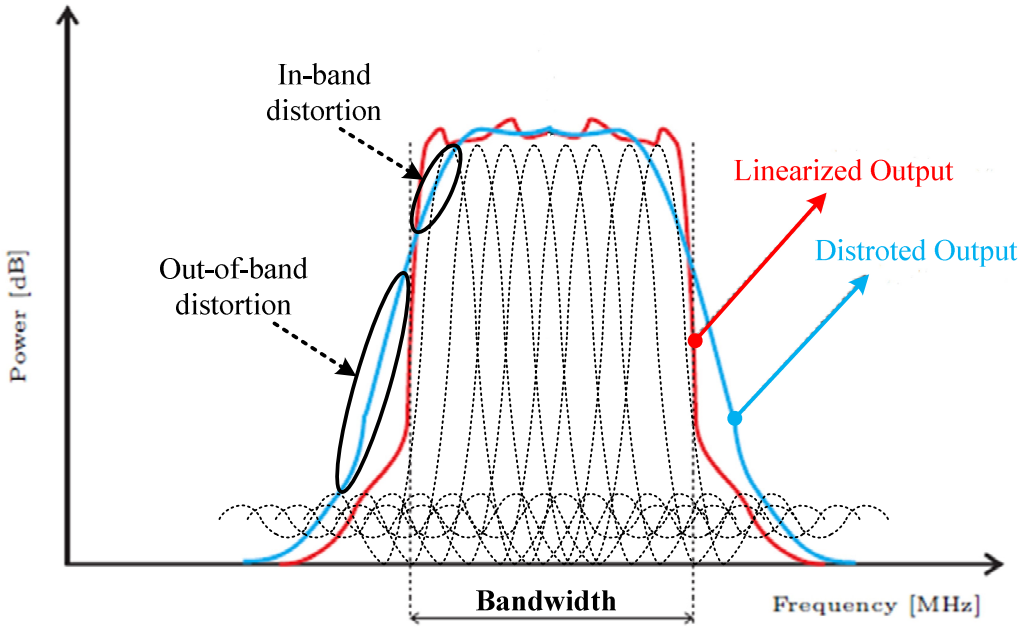


Figure 2.10 An in-band/out-of-band distortion creates spectral broadening in an OFDM bandwidth taken from [55].

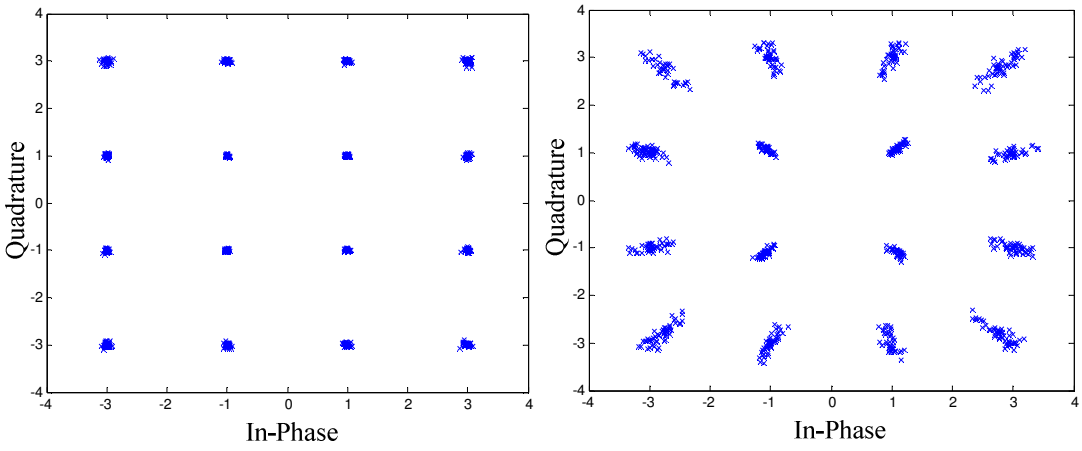


(a) The received signals without an in-band distortion. (b) The received signals with an in-band distortion.

Figure 2.11 The error vector magnitude effect on the 16-*QAM* constellation.

In the received signal, an in-band distortion leads to the error vector magnitude problem as shown in Figure 2.11. In addition, an out-of-band distortion leads to the spectral regrowth problem causing adjacent channel interference among OFDM spectrums, which can be shown in Figure 2.9 [55].

To solve these problems, the input signal needs to vary within the linear region by whether to reduce the input power or to require the expensive amplifiers (or the widely linear region amplifiers).

The nonlinearities of the amplifier degrade the transmitted signal in many ways. The most significant drawbacks are as following [56]:

- Additional non-linearity of amplifiers creates interference in the terminals.
- Spectral spreading of the OFDM signals causes adjacent channel interference.
- Both deformation and spreading are occurred in the signal constellation.

### 2.5.1 RF Amplifier Models

Many RF amplifier models are available in many pieces of literature. They can be mainly grouped into three types: the soft limiter, the solid state power amplifier, and the traveling-wave tube. All of them can be shortly described as follows:

- *Soft Limiter* [57]. The simplest type of the HPA is the soft limiter amplifier. It has no distortion in the input phase of the signal. It plainly cuts the signal magnitude if the signal surpasses a threshold.
- *Solid State Power Amplifier* (*SSPA*) [58]. The most widely used model for the amplifier in wireless communications. Its main drawback is that the distortion in amplitude always occurs, but it has no distortion in the signal phase.
- *Traveling-Wave Tube* [59-61] also known as Saleh model. The nonlinear distortion occurs in both amplitude and phase. The traveling-wave tube is wideband amplifiers widely used in satellite communications.

In this thesis, the downlink transmission of the large-scale MIMO systems is focussed. The simple zero-forcing processing is used for precoding the 16-*QAM* modulated vector to be the transmitted vector, $\boldsymbol{x}_{\Omega_{ZF}} \in \mathbb{C}^{n_t \times 1}$, where $E\left[\left\|\boldsymbol{x}_{\Omega_{ZF}}\right\|^2\right] = 1$. Then, the received vector, $\boldsymbol{y} \in \mathbb{C}^{n_u \times 1}$, is given by

$$\boldsymbol{y} = \sqrt{p}\mathbf{H}^H \boldsymbol{x}_{\Omega_{ZF}} + \boldsymbol{z}; \tag{2.8}$$

where $p$ is the average SNR, $z \in \mathbb{C}^{n_u \times 1}$ is the additive noise vector, and $(\cdot)^T$ is a transpose operator [37].

## 2.6 Summary

This chapter has provided an introduction to large-scale MIMO-OFDM systems as well as some definitions of the non-linear amplifiers. This non-linearity causes negative impacts for the transmitted signal. They include in-band/out-of-band distortions, spectral regrowth effect, and adjacent channel interference. These significant problems increase the overall error rates in the systems.

Some mathematical parameters have been represented in each section, and they are used to pave the way in the next chapter. In the next chapter, the PAPR problems are presented, and their existing solutions are also explained.

# Chapter 3

# Peak-to-Average Power Ratio (PAPR)

This chapter studies the existing PAPR reduction methods for large-scale MIMO-OFDM systems. The fundamental definitions of PAPR will be presented at the beginning of the chapter. Also, many parameters used for measuring the high amount of PAPR will be presented. Finally, the comparison of some PAPR reductions will be shown in the summary section.

Section 3.1 introduces fundamentals of the PAPR problems in OFDM system. Also, the complementary cumulative distribution function (CCDF) of PAPR will be described in its subsection. Section 3.2, PAPR reductions will be categorized. Some of the existing PAPR reductions are represented in this section. Finally, CCDF measurement is used to compare their reduction performance to be presented in section 3.3.

## 3.1 PAPR in OFDM

A large number of independent signals modulated onto orthogonal subcarriers are contained in the OFDM signals within bandwidths. In Figure 3.1, many subcarrier components are added by an IDFT operation causing high peak values in the time domain. As a result, OFDM systems are known to have a high amount of PAPR compared to single carrier systems [62-63].

This high PAPR causes the nonlinearity of the commonly employed high power amplifiers. The high dynamic range of PAPR leads to both in-band distortion which

degrades the BER, and out-of-band distortion interfering with neighbouring frequency bands. A high PAPR signal requires the RF amplifiers to have a wide range of linear response and therefore they tend to be expensive. In the downlink transmission, the PAPR problem put a high drain on the transmitted power at the BS. In contrast, therefore the uplink transmission, the efficiency of the amplifier is critical due to the limited battery power in a mobile terminal. This is the main requirement for the next generation of the wireless standard to tackle this problem especially in the multiple antenna OFDM systems [64-65].

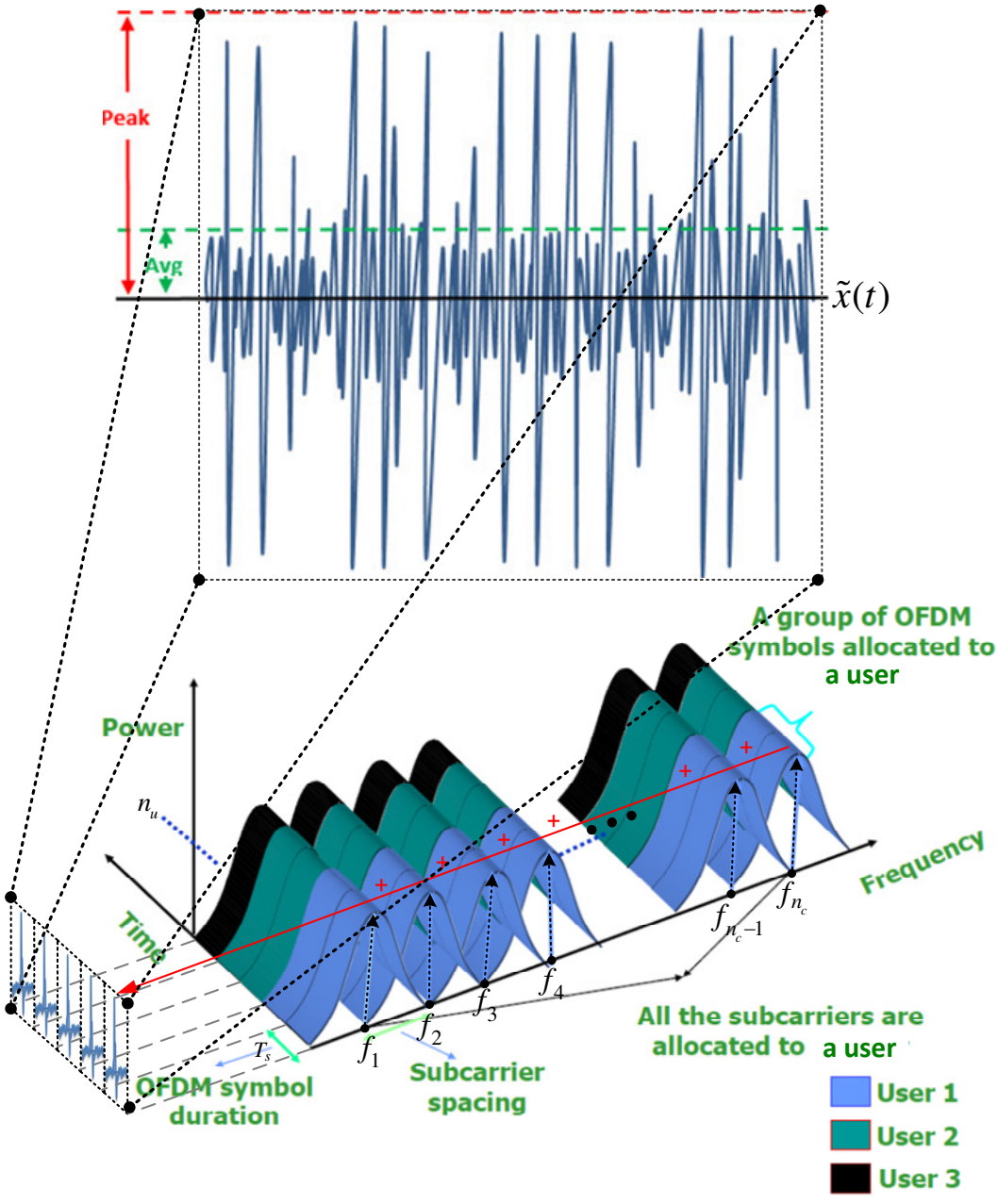


Figure 3.1 The high peak values of OFDM systems in the time domain adapted from [63].

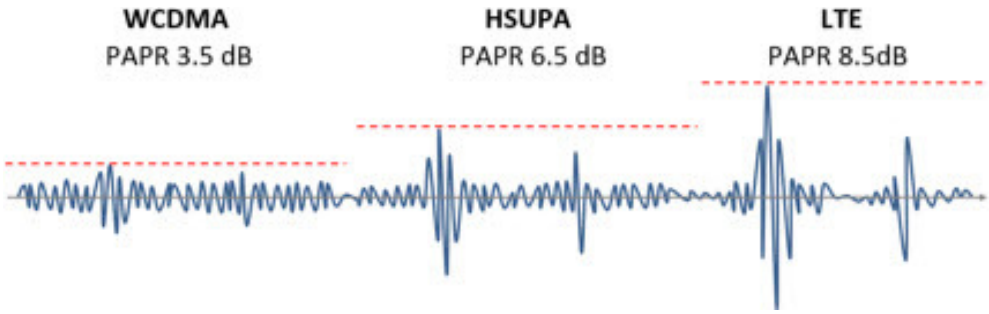


Figure 3.2 A comparison of the high PAPR in WCDMA, HSUPA, and LTE standards taken from [66].

Figure 3.2 shows the typical PAPR in [1]WCDMA, HSUPA and LTE signals: WCDMA is about 3.5 decibels (dB), the HSUPA is around 3.5 dBs, and LTE around 8.5 dBs respectively. Both the WCDMA and HSUPA are employed in the third generation of the wireless communication standard, but for LTE is only a standard that is used in the fourth generation. Looking forward at the trend, the multiple antenna systems using OFDM technology will have a higher value of PAPR [66]. Thus, PAPR reduction still remains one of the hot topic research areas in the next generation of the OFDM systems [14, 21-27].

In both [67] and [68], the PAPR for a continuous-time signal, $\tilde{x}(t)$, in one symbol duration, $T_s$, is defined as:

$$PAPR = \frac{\max\left[\left|\tilde{x}(t)\right|^2\right]}{E\left[\left|\tilde{x}(t)\right|^2\right]}, \quad 1 \le t < T_s. \tag{3.1}$$

On the other hand, the effect of the discrete-time nature of PAPR signals can be estimated by oversampling the data sequence $\boldsymbol{x}$. It can also be shown in Figure 2.4 by a factor $c$ and processing $cn_c$-points IDFT of the data block. Therefore, in this case, the PAPR is defined as

$$PAPR = \frac{\max\left[\left|\tilde{x}[k]\right|^2\right]}{E\left[\left|\tilde{x}[k]\right|^2\right]}, \quad k = 1, 2, \cdots, cn_c, \tag{3.2}$$

[1] WCDMA, HSUPA, and LTE stand for Wideband Code Division Multiple Access, High-Speed Uplink Packet Access, and Long Term Evolution respectively.

where $E(|\cdot|)$ is the expected value, denotes the average, and $c$ is an oversampling factor.

### 3.1.1 CCDF of PAPR

One of the most regularly used tools for measuring the efficiency of PAPR reduction methods is the cumulative distribution function (CDF). Usually, the [2]CCDF is employed instead of CDF because it measures the probability of the exceeding the reference value denoted as $PAPR_0$.

According to the Central Limit theorem for a multi-carrier signal with a large number of subcarriers, the real and imaginary value of the time domain signals have a mean of zero and a variance of 0.5. Therefore, Rayleigh distribution is given by the amplitude of the multi-carrier signal in a central chi-square distribution with two degrees of freedom. This is obeyed for the power distribution of the system [18]. From (2.5) to (2.8), the CDF of the IDFT signal, $\tilde{x}$, each $t_{th}$ antenna is given by

$$F(\tilde{x}) = 1 - e^{-\tilde{x}}, \tag{3.3}$$

where

$$\tilde{x} = \Im^{-1}[x] = \sum_{c=-\frac{n_c}{2}}^{\frac{n_c}{2}} X_c e^{j2\pi\frac{kc}{n_c}}.$$

Then, the probability of the PAPR for a non-oversampling data block can be written as

$$Pr[PAPR \le \tilde{x}] = F(\tilde{x})^{n_c} = \left(1 - e^{-\tilde{x}}\right)^{n_c}. \tag{3.4}$$

Moreover, the CCDF of the PAPR can be presented by

$$CCDF = Pr[PAPR > PAPR_0] = 1 - F(PAPR_0)^{n_c} = 1 - \left(1 - e^{-PAPR_0}\right)^{n_c}. \tag{3.5}$$

[2] CCDF = 1 - CDF.

Finally, all mathematical equations of the CCDF from Eq. (3.1) to Eq. (3.5) can be simply represented as in Figure 3.3.

## 3.2 Categorization of the PAPR Reductions

The studies of the PAPR reduction techniques can be divided into two types: signal scrambling techniques and signal distortion techniques [69]. Both categorizations of PAPR reductions can be represented in Figure 3.3.

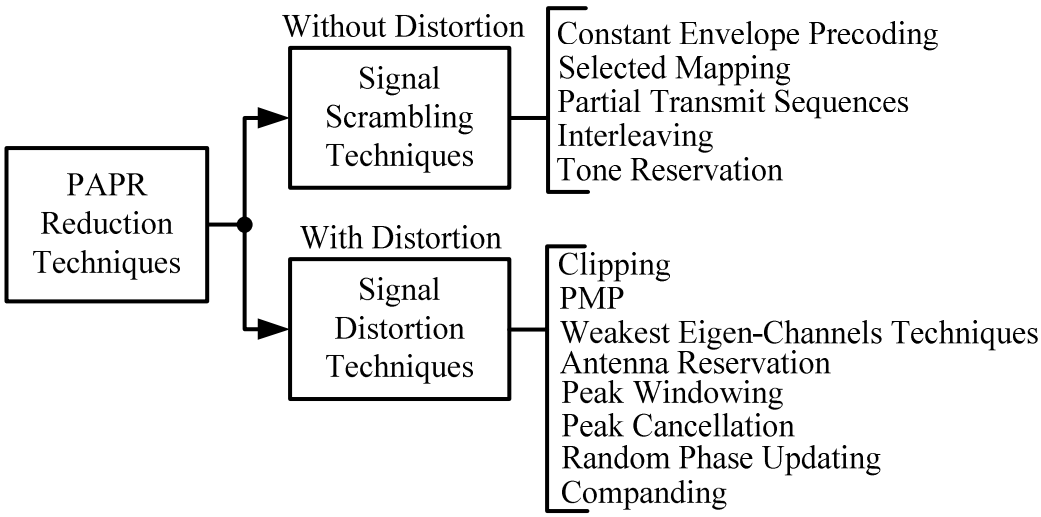


Figure 3.3 Categorization of the PAPR reduction schemes adapted from [69].

### 3.2.1 Signal Scrambling Techniques

Signal scrambling techniques scramble the codes or change the signal phases in order to reduce the high PAPR. The precoding techniques can be employed for signal scrambling. They include constant envelope precoding, selected mapping, partial transmit sequences, interleaving, tone reservation, etc. However, the drawback of these techniques is that they increase the number of carriers required to retain the side information.

The signal scrambling techniques can be summarized by the following subsections:

- *Constant Envelope Precoding*. Mohammed and Larsson [22] proposed the constant envelope by coding the chosen phase angles of the transmitted signal. By this technique, it reduces the interference between users, causing the reduction of the in-band distortion and high PAPR signals. However, this technique requires an extra 2 dB transmission power per antenna in order to send information to receivers without any distortions. Many researchers have been seeking ways to reduce its power of each antenna in large-scale antenna systems.
- *Selected Mapping*. Bauml et.al. [70] presented a technique for the PAPR reduction. By generating a whole set of candidate signals, it represents the same information, and then the most favourable signal as regards to minimum PAPR are chosen and transmitted. The chosen candidate signal needs to be sent along with the original information explicitly. A goal is to make the occurrence of the peaks less frequent, but not to eliminate the peaks. Nevertheless, an increase in overhead of transmitted signals is driving many researchers to seek ways to reduce its size.
- *Partial Transmit Sequences*. Muller and Huber [71] invented a novel technique that combines the partial transmit sequences. It is a flexible and an effective peak power reduction method. The main idea behind this technique is the data block. It is grouped into non-overlapping sub-blocks, and then each sub-block is rotated with a statistically independent rotation factor. The time domain signals with the lowest peak amplitude are generated by a rotation factor, which are sent to the receiver as side information. By this technique, the high peak of PAPR is minimized significantly.

  Actually, this technique is built from the select mapping technique. It is also found that the partial transmit sequences are more effective than select mapping in order to reduce PAPR problems. However, the same with the constant envelope precoding method, the reduction of the complexity of this technique is a challenge for future research.
- *Interleaving*. Jayalath and Tellambura [72] proposed an interleaving block data technique that can reduce the PAPR of the OFDM signal. This method shows that the highly correlated signal causes the large amount of PAPR. The main idea of this technique is to break up the long correlation patterns by

interleaving it. Therefore, the signal randomization technique for the reduction of the PAPR was invented. The advantage of this technique is that it is less complex than others with the same achievable performance. However, the future development of this method may aggravate a limitation due to the high order of the interleaved data frames.

- *Tone Reservation*. This technique was invented by Tellado [73]. The main idea of this technique is the reservation of the small group of the OFDM subcarriers for PAPR reduction. The value of the high peak signals in PAPR depends on the numbers of the reserved subcarriers, which are used for minimizing the PAPR formulated as a convex problem.

### 3.2.2 Signal Distortion Techniques

Signal distortion techniques have recently been studying to decrease the high peak levels of PAPR. In general, these techniques increase the complexity of the system. The clipping technique is therefore more popular than other signal distortion techniques because it is less complex. More practical solutions include PMP, weakest eigenchannels techniques, antenna reservation, peak windowing, peak cancellation, random phase updating, companding, and so on.

The signal distortion techniques can be summed up by the following subsections:

- *Clipping Scheme (CP)*. The most common tool is used for reducing the high amount of PAPR signal [74]. The high peaks of the amplitude are limited by a threshold. A predefined threshold is set for this technique to clip all high range signals in OFDM system. The aim of this method is to satisfy the constraints of the OFDM spectrum so that the transmitted signal does not interfere with neighbouring frequency bands. However, the in-band distortion cannot be avoided causing the increment of BER. The in-band distortion is small when the clipping threshold is high level because the probability of large peaks is small.

  The advantage of clipping PAPR technique is that it is the simplest and easiest method. It reduces the high degree of PAPR by setting a maximum

level for the transmission signal. On the other hand, the clipping PAPR reduction causes the in-band distortion. This increases the BER, especially in the large-scale MIMO-OFDM systems.

- *The Precoding Modulation PAPR Reduction Scheme (PMP).* A powerful tool for PAPR reduction technique was proposed by Studer and Larsson [21]. It combines the functionality of precoding, modulation, and PAPR reduction together. For the PAPR reduction, a FITRA algorithm was invented to iteratively shrink the high dynamic range of the PAPR in the frequency domain. The advantage of PMP technique is to highly reduce the high amount of PAPR signals without greatly diminishing BER performance compared with other schemes. Nevertheless, the FITRA algorithm involves the great complexity base on the cycle of the iterative loop. There is a challenge to reduce its complexity.
- *Weakest Eigen-channels Techniques.* This technique uses the last eigenchannels of a massive MIMO channel to approximate the peaks exceeding a given target value in the least squares fashion [23]. Subtracted from the original signal in the time domain, then approximate exceedance model is created.

  The advantage of this technique is that it is the iterative reducing PAPR level. It is suitable for the flexible systems needed to be adjusted the speed of the processing. However, this method requires a highly accurate estimation. Otherwise, it will degrade the entire system by causing serious BER degradation.
- *Antenna Reservation.* This technique employs a low complex approach to tackling the PAPR problems. The main idea is to intentionally clip signals sent to a set of reserved antennas. It is used for recompensing by transmitting correction signals on one set of antennas. By reserving 25% of transmitted antennas, the high PAPR signal can be reduced about 4 dB with a 15% complexity overhead [75-76].

  The advantage of the antenna reservation is that it is less complex. Its speed when deliberately clipping signals is impressive. However, the reserved antennas have to increase in proportion to the available antennas 25%. To

implement this technique, it would be better to able to adjust those reserved antennas depending on system channel circumstances.

- *Peak Windowing.* This technique was proposed by Nee and Wild [64]. The main idea of this scheme is to remove high PAPR peaks by multiplying those peaks with peak windowing techniques. They include Gaussian shaped window, cosine, Kaiser, and Hamming windows. Compared with the CP, the peak window technique provides better high PAPR removing with better spectral efficiency.
- *Peak Cancellation.* The peak cancellation method was introduced by May and Rohling [77]. This main idea of this technique is to use a time-shifted and scaled reference function by subtracting from the original signal. Then, each subtracted reference function will be used to reduce the high dynamic range of PAPR signals. However, the main focus for many current scientific fields is to find ways to decrease the processing times by adding the correcting function.
- *Random Phase Updating.* A novel technique that randomizes the phase of transmitting signals by updating algorithm was invented by Nikookar and Lidsheim [78]. It can reduce the high PAPR signals of the OFDM signal by assigning a random phase to each subcarrier. This process continues until the high amount of PAPR is reduced bellow the referencing threshold. Both threshold and the number of iterations can be adjusted by BS. The advantage of this method is that it is flexible; BS can adjust some parameters that affect the quality of the BER in the cell. On the other hand, when the number of iterations is increased, the complexity increases substantially. A research challenge for this technique is to minimize the complexity from a large iteration.

  Many researchers are seeking to reduce the complexity of this method.
- *Companding.* A simple technique for PAPR reduction was proposed by Wang et.al. [79]. The effective companding scheme assumes the OFDM signal as the Gaussian distributed, and the high peaks of PAPR signal occur infrequently. The main idea of this technique is to convert the baseband OFDM signal before converting into an analog waveform. Both companding and quantizing are used for the OFDM signal after taking IDFT process. To

sum up, this technique focuses on improving the quantization solution of the low-level of PAPR signals. Due to the low PAPR signals are more likely to occur in transmitted signal than the high PAPR signals.

This thesis focuses on improving the proposed technique on the part of the signal distortion techniques, which are the CP and the PMP scheme. Their details will be thoroughly explained in Chapter 4 and Chapter 5 respectively.

## 3.3 Summary

The main goal of this chapter is to review the existing tools that are used for solving the PAPR problems. Several techniques to reduce the PAPR have been invented from many researchers. All of them have the potential to provide a substantial reduction in PAPR. A Comparison of CCDF performance of those techniques will be shown in Figure 3.5. They include CP, PMP, antenna reservation, weakest eigenchannels, constant envelope precoding will be shown in this section. The simulation model of the large-scale MIMO-OFDM downlink system will be used in this comparison with their similar complexity.

In Figure 3.5, the main system parameters are defined as follows: length of transmitted data, $n_s$, 216 bits per 1 user/packet and a number of the packets are 1000 packets, the channel taps $n_d$ = 4, the single antenna terminals $n_u$ = 10, the number of the antennas at BS $n_t$ = 100, a number of OFDM subcarriers $n_c$ = 128. Also, we utilize 16-QAM constellation to map the coded bits at the BS.

For the channel encoder, a convolution encoder is employed with these parameters: channel code rate = 0.5, code generator polynomials = $[133_0\ 171_0]$ applying with puncturing and random interleaving, constraint length = 7, the Bahl, Cocke, Jelinek, and Raviv (BCJR) decoder is used for channel decoding for each user.

For the parameters for all PAPR reductions, the clipped signal vector $\tilde{\boldsymbol{x}}_{\beta}$ for clipping PAPR scheme is the 80% below the threshold of the original vector $\tilde{\boldsymbol{x}}$. A regularization parameter of PMP scheme $\lambda_{PMP}$ = 0.25; a number of FITRA iterations

$Z_{PMP}$ = 2000. For the weakest eigenchannels techniques, a weighting factor is 30; the number of iteration is 2. For antenna reservation scheme, a tolerance level of 99% is used as a benchmark for transmitted antennas; the 25% reserved antennas are used for distortion prediction sending [21-23, 74-76, 80].

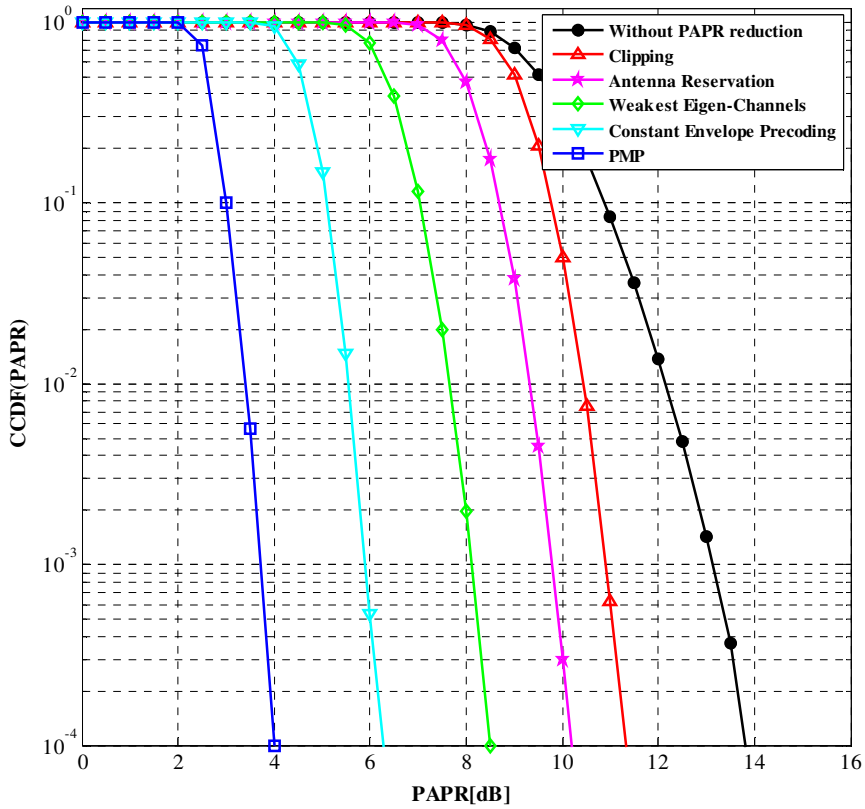


Figure 3.4 The CCDF performance comparisons for PAPR reduction schemes.

In Figure 3.4, it seems that the PMP (a blue squared-line) is the best PAPR reduction scheme, which can highly reduce large PAPR signal about 11dB. On the other hand, the worst case seems to be the clipping PAPR technique (a red triangle line). It only reduces the high dynamic range of PAPR approximately 1.5dB reduction. Finally, other PAPR reduction schemes can be arranged in term of descending order of CCDF, i.e., antenna reservation technique (a pink star line), weakest eigenchannels method (a green diamond line), and constant envelope precoding scheme (a light blue upside down triangle line) respectively.

For the next chapter, the iterative PAPR reductions controlled with SER will be presented. Both clipping technique and PMP are chosen for this proposed iterative methods. Both schemes will be modified for all users in the large-scale MIMO-

OFDM downlink systems in this thesis. After that, the comparison of the lowest performance (clipping) and the highest performance (PMP) cooperated with the APO will be tested in Chapter 5 and 6 respectively.

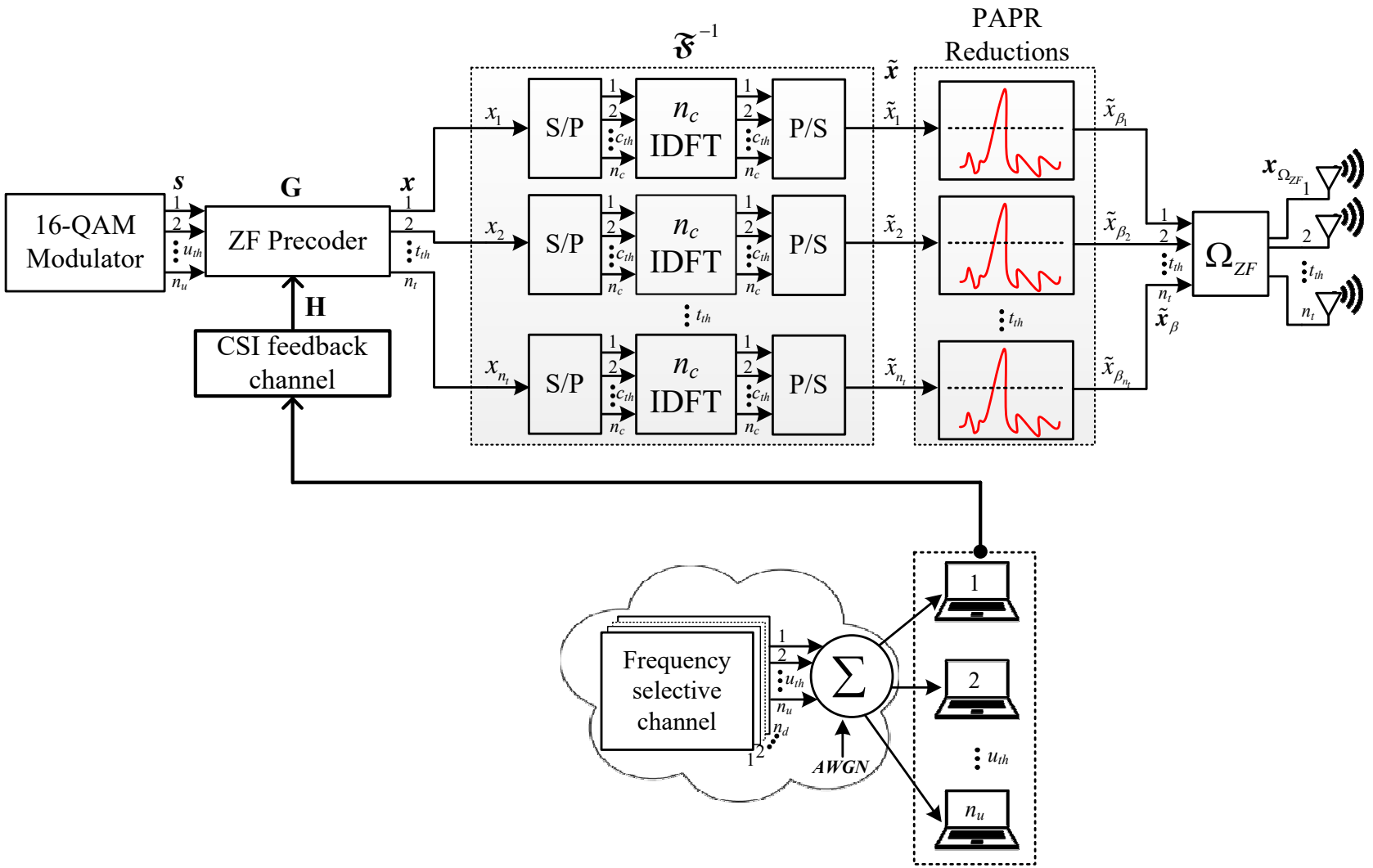


Figure 3.5 The existing PAPR reduction area on the large-scale MIMO-OFDM downlink system.

# Chapter 4

# The Adjustable PAPR Reduction Level Controlled with SER Feedback

In this chapter, the new versions of both clipping and precoding modulation PAPR reduction (PMP) for PAPR reduction are proposed. The aim of these novel techniques is to use SER feedback from all users to adjust the PAPR clipping level. With the benefit of the CSI in large-scale MIMO-OFDM systems, the feedback channel will be used in these techniques.

The classical work for the iterative PAPR reduction level was proposed by J. Armstrong [81]. The advantage of this approach is that a clipped signal level can be gradually adjusted to a higher or lower level by a control parameter. This thesis will utilize this benefit by using the users' SER feedback to control this level. From his idea, the developing versions of both clipping and PMP combined with the APO (in Chapter 5) are devised to improve the massive MIMO-OFDM system performance. Using our proposed approaches, both error rate and transmit power are reduced effectively. The simple block diagram of the proposed technique is presented in Figure 4.1.

In this chapter, section 4.1 will present the operational regime of the amplifier for using the adjustable PAPR level. The adjustable level of both the CP and the PMP will be proposed in section 4.2 and section 4.3 respectively. Finally, the summary of this chapter will be concluded in section 4.4.

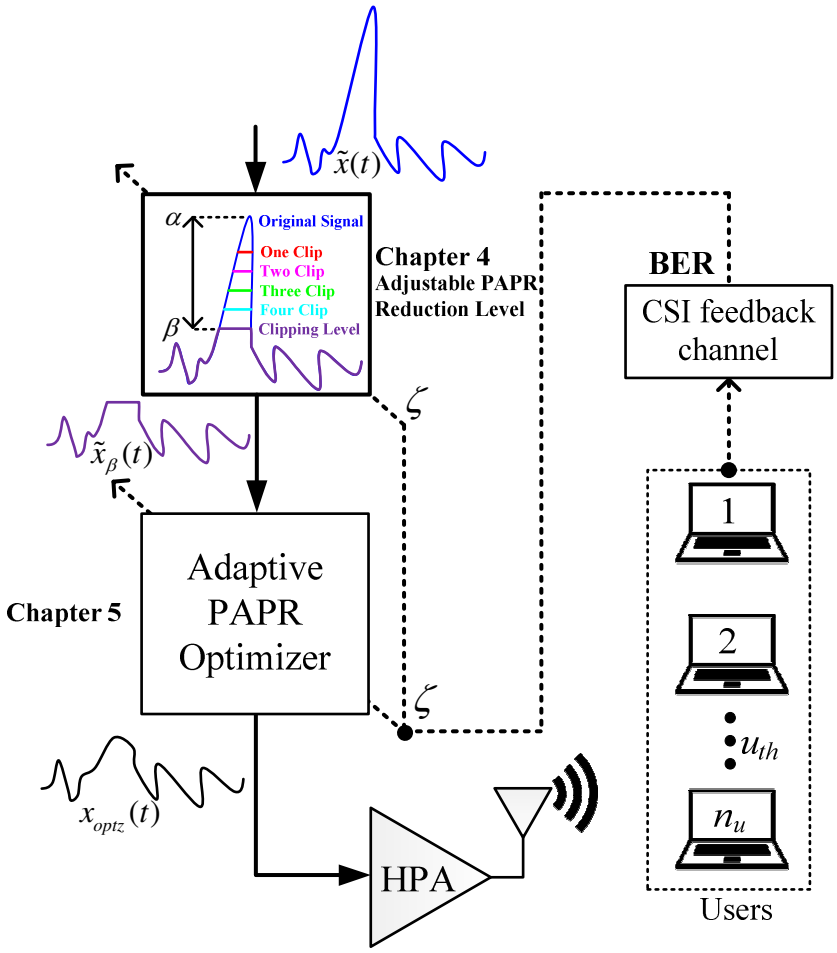


Figure 4.1 The adjustable PAPR reduction level working with the APO.

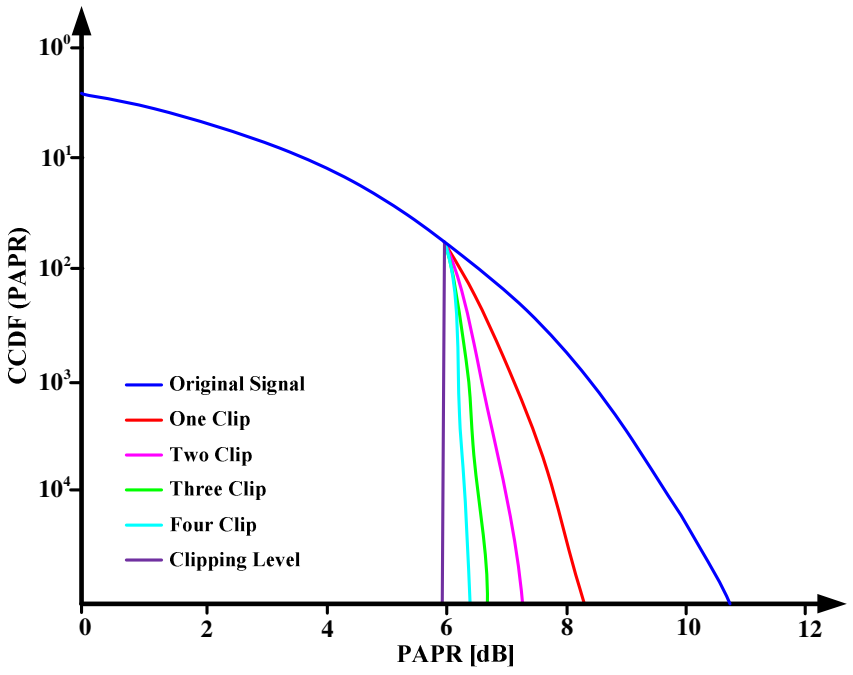


Figure 4.2 CCDF of transmitted signal after repeated PAPR clipping taken from [81].

# 4.1 The Range of Adjustable PAPR Level

The rough case of the large-scale MIMO–OFDM channel occurs when, a user in the WLAN cell requires higher dynamic range, $\alpha$, of the transmitted signal from BS. It means that the PAPR reductions have to progressively increase the threshold clipping level, $\beta$, in order to ensure a sufficient signal is being sent through the ill-behaving channel. By this idea, the average $\zeta$ of the SER from the terminals is used for identifying the state of the error rate in the WLAN cell from all terminals. In contrast, in the case of low noise in the WLAN channel, the PAPR reduction level could be decreased in response to SER feedback in order to reduce transmission power. As a result, this technique can help to efficiently save unnecessary energy in the large-scale OFDM-MIMO systems when $E_b/N_0$ is in the low power regime [82-92].

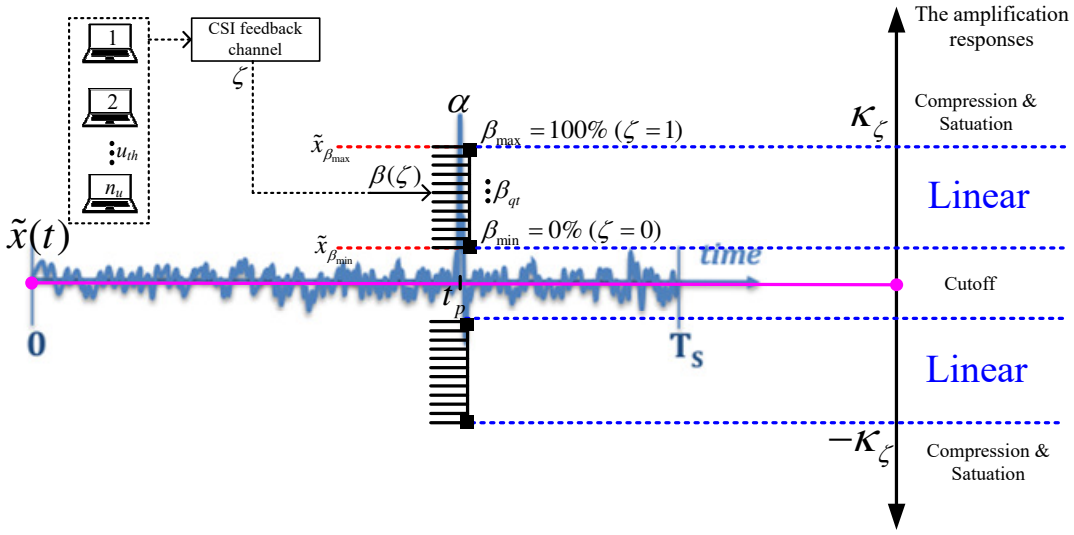


Figure 4.3 The range of adjustable PAPR level for the HPA characteristic[1].

As mentioned in Chapter 2, the practical RF amplifiers exhibit various magnitudes of nonlinearities. In this thesis, the RF amplifiers are assumed to operate in the linear region and all users in a WLAN cell communicate to BS under the same SNR circumstance. Therefore, the overall SER from all terminals can be expressed as

[1] In practical systems, $\kappa_\zeta$ is defined by a maximum input dynamic range of the HPAs that have a linear response, and in this thesis, a scaling factor is assumed to be equal a maximum clipping level (or $\kappa_\zeta = \tilde{x}_{\beta_{\max}}$).

$$\zeta = \frac{\left(\zeta_1 + \zeta_2 + \ldots + \zeta_{n_u}\right)}{n_u}, \quad 0 \le \zeta \le 1, \tag{4.1}$$

where $\zeta_{u_{th}}$ is a SER of $u_{th}$ user in a WLAN cell.

In (4.1), it is used to control the adjustable PAPR reduction level, $\beta(\zeta)$, varying within a range manual by maximum clipped signal level,

$$\tilde{x}_{\beta_{\max}} = \frac{\alpha\beta_{\max}}{100}; \text{when } \zeta = 1, \tag{4.2}$$

and minimum clipped signal level,

$$\tilde{x}_{\beta_{\min}} = \frac{\alpha\beta_{\min}}{100}; \text{when } \zeta = 0, \tag{4.3}$$

where $\beta_{\max}$ and $\beta_{\min}$ are the percentages of the maximum quantized PAPR level and the minimum quantized PAPR level respectively.

Therefore, the adjustable PAPR level can be represented as

$$\beta(\zeta) = \alpha\beta_{qt}, \quad \begin{matrix} 0 < \tilde{x}_{\beta_{\min}} \le \beta(\zeta) \le \tilde{x}_{\beta_{\max}} \\ 0 < \beta_{min} \le \beta_{qt} \le \beta_{max} \end{matrix}, \tag{4.4}$$

where $\alpha$ is the highest peak level of $\tilde{x}(t)$, $\beta_{qt}$ is the percentage of the quantized PAPR level.

## 4.2 The Adjustable PAPR Level for the CP

A clipping PAPR reduction scheme is the simplest technique to reduce the high PAPR signals [93]. A predefined threshold is set to clip all high range signals in the OFDM system. The aim of this method is to satisfy the constraints of the OFDM spectrum so that the transmitted signal does not interfere with neighbouring frequency bands. However, the in-band distortion cannot be avoided, causing an increase in BER. The in-band distortion is large when the clipping level threshold is low because the probability of large peaks is high. The in-band distortion may be

limited to a predefined strength with the degradation of PAPR-reduction performance [94-97]. For the clipping PAPR reduction scheme, the clipping operation is defined as

$$\left|\tilde{x}_{\beta_{CP}}(t)\right| = \begin{cases} \left|\tilde{x}(t)\right|, & \text{if } \left|\tilde{x}(t)\right| < \beta \\ \beta, & \text{if } \left|\tilde{x}(t)\right| \geq \beta \end{cases}, \tag{4.5}$$

and the percentage of the clipping threshold is defined as

$$ClippingThreshold = \frac{\beta}{max\left[\tilde{x}(t)\right]} \times 100\%. \tag{4.6}$$

The advantage of a clipping PAPR technique is that it is the simplest and easiest method to reduce the high PAPR. It is powered by setting a maximum level threshold for the high PAPR transmitted signal as shown in Figure 4.4. On the other hand, some disadvantages occur when clipping is employing to reduce high PAPR. It causes the in-band distortion degrading the BER performance in the large-scale MIMO-OFDM systems [98].

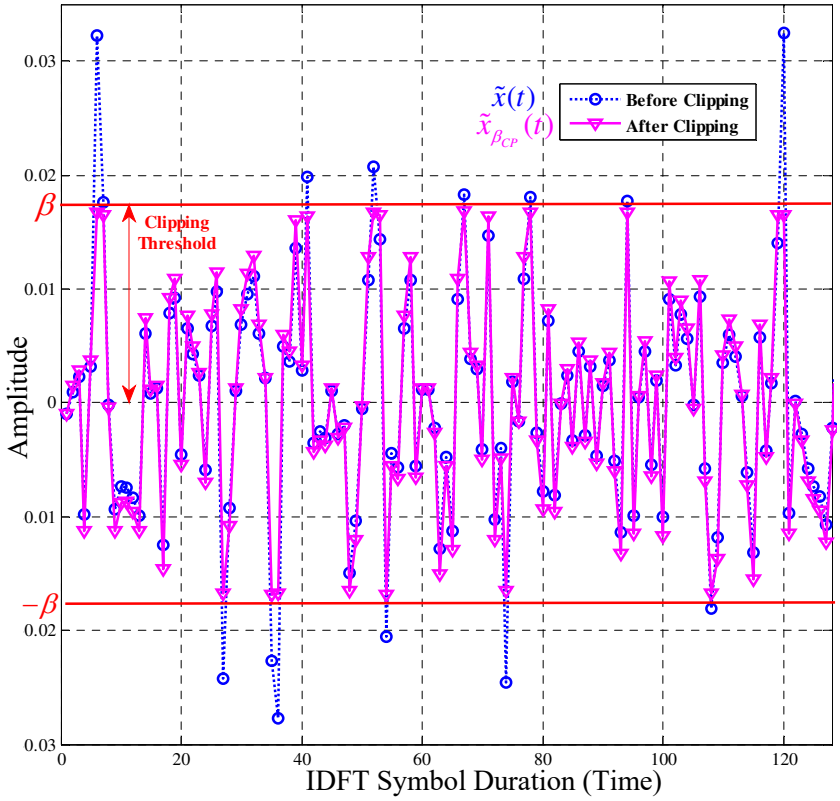


Figure 4.4 The fixed level of PAPR peak clipping.

As mentioned above, the drawback of the CP is the in-band distortion caused by the low level of clipping. Unfortunately, the situation will be worse than this if the in-band distortion occurs at the same time as a high value of AWGN in the MIMO channel.

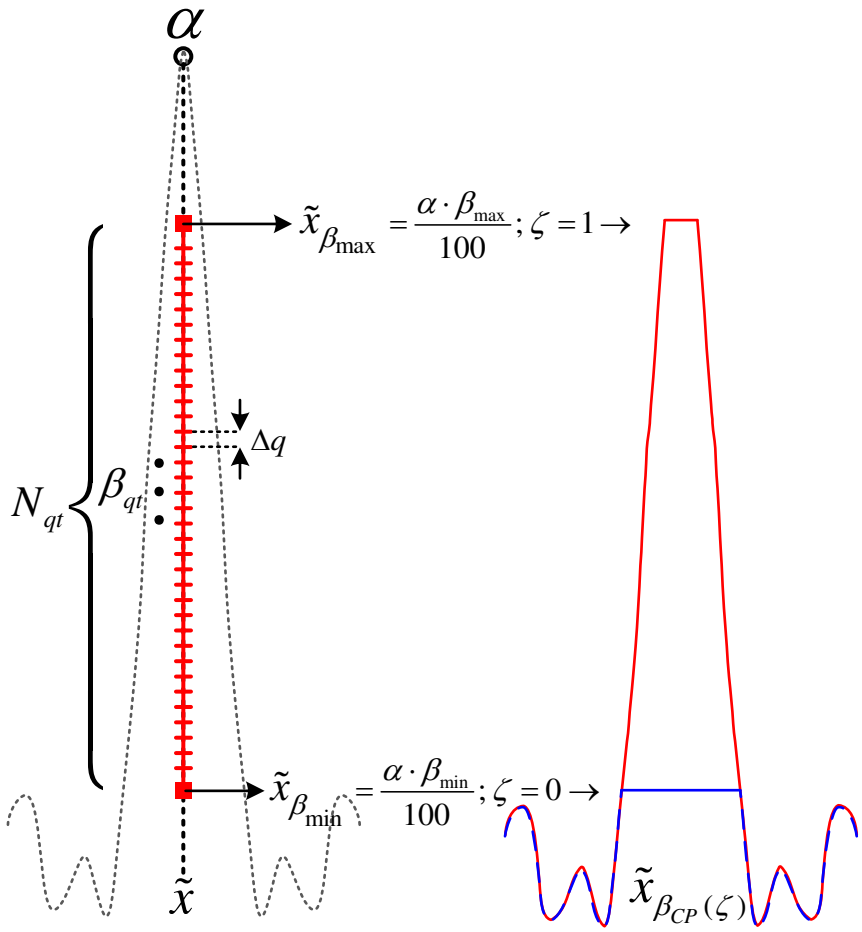


Figure 4.5 Adjustable PAPR-CP.

To solve this problem, the BS needs to know the situation of the channels from all terminals in the WLAN cell. As a benefit of the CSI, all users are able to send each SER back to the BS to adjust the PAPR clipping level in order to avoid both in-band distortion and negative effects from the ill-behaved channel. Then, the clipped signal in Eq. (4.5) can be rewritten as *the adjustable clipping level controlled with SER feedback* as

$$\left|\tilde{x}_{\beta_{CP}(\zeta)}(t)\right| = \begin{cases} \left|\tilde{x}(t)\right|, & \text{if } \left|\tilde{x}(t)\right| < \beta(\zeta) \\ \left|\alpha\beta_{qt}\right|, & \text{if } \left|\tilde{x}(t)\right| \geq \beta(\zeta) \end{cases}, \quad \left|\tilde{x}_{\beta_{\min}}\right| \leq \left|\tilde{x}_{\beta_{CP}(\zeta)}(t)\right| \leq \left|\tilde{x}_{\beta_{\max}}\right|. \tag{4.7}$$

Then, a quantized step of the adjustable PAPR clipping can be presented as

$$\Delta q = \frac{\tilde{x}_{\beta_{\max}} - \tilde{x}_{\beta_{\min}}}{N_{qt}}, \tag{4.8}$$

where [2] $N_{qt}$ is the total number of the quantising steps.

From Eq. (4.7) to Eq. (4.8), if the users' error rate is high, the $\tilde{x}_{\beta_{CP}(\zeta)}$ increases by an amount $|\alpha\beta_{qt}|$ with the step $\Delta q$. On the other hand, if the users' error rate is low, the $\tilde{x}_{\beta_{CP}(\zeta)}$ steps down toward $\tilde{x}_{\beta_{\min}}$. Both $\tilde{x}_{\beta_{\max}}$ and $\tilde{x}_{\beta_{\min}}$ are set to limit the highest and lowest threshold for the adjustable clipping level to work within the linear region of the RF amplifier. Finally, the process of the adjustable PAPR level for CP can be shown as Algorithm 1 in Appendix D.

## 4.3 The Adjustable PAPR Level for PMP

To reduce PAPR problems, the PMP method was invented by C. Studer and E. G. Larsson [21]. The integration between a MU Precoding, an OFDM Modulation, and a PAPR reduction is compatible with the MU-MIMO-OFDM downlink system. The FITRA is employed for shrinking the high dynamic range of the PAPR in the PMP. As a result, the high PAPR is reduced by approximately 11dB compared with the ZF precoder as shown in Figure 3.3.

The total process of the PMP technique combined with FITRA is shown in Figure 4.7. Furthermore, Algorithm 2 can also be presented in Appendix D. The PMP process starts with 16-QAM symbols, $\boldsymbol{s}$, to feed to the complex-to-real valued conversion. Then, the real stream signal $\hat{\boldsymbol{s}}$ is clipped by the FITRA with a slight clipping in the feedback loop, $Z_{PMP}$. When the number of $Z_{PMP}$ is high, the peak level of $\tilde{\boldsymbol{x}}_{\beta_{PMP}}$ is low. After that, the low PAPR signal $\boldsymbol{x}[Z_{PMP}]$ reverts back to the

[2] In this thesis, the initial value of $N_{qt}$ will be manually set to 10.

complex signal $\tilde{\boldsymbol{x}}$. Finally, the subsample and transpose processes are mapped as the stream signal $\tilde{\boldsymbol{x}}$ to be the transmitted signal $\tilde{\boldsymbol{x}}_{\beta_{PMP}}$.

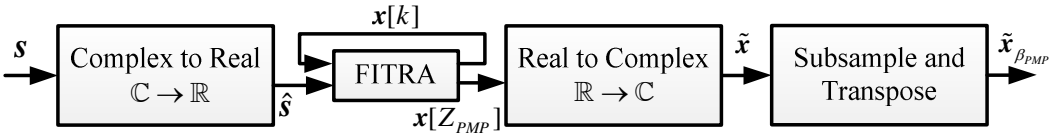


Figure 4.6 The PMP process (sourced from [21]).

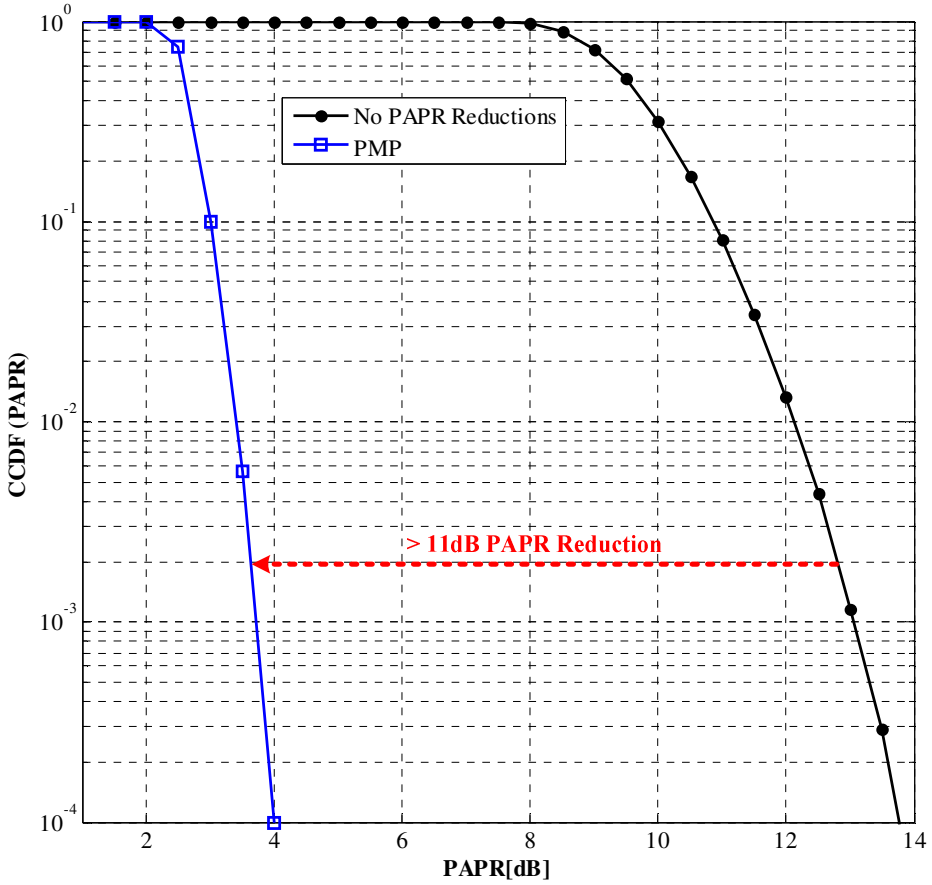


Figure 4.7 CCDF of PMP performance taken from [21].

From the Figure 4.6 and Algorithm 2, the most important part of PMP method is the FITRA process, which is adapted from [99-100]. It can be started with the general non-smooth convex optimisation model as:

$$\min_{\boldsymbol{x}} \left\{ F(\boldsymbol{x}) = g(\boldsymbol{x}) + h(\boldsymbol{x}) \right\}, \tag{4.9}$$

where both $g(\boldsymbol{x})$ and $h(\boldsymbol{x})$ are a real-valued *non-smooth convex* function and a real-valued *smooth convex* function respectively.

The Lipschitz constant of the gradient $\nabla h(\boldsymbol{x})$ is $\mathcal{L}$, where $\mathcal{L} = 2\sigma_{max}^2(\mathbf{H})$, and $\sigma_{max}(\cdot)$ is the largest singular value. The proximal map of the FITRA defined as:

$$\mathbf{p}_{\mathcal{L}}(\boldsymbol{y}) = \arg\min_{\boldsymbol{x}} \left\{ g(\boldsymbol{x}) + \frac{\mathcal{L}}{2} \left\| \boldsymbol{x} - \left( \boldsymbol{y} - \frac{1}{\mathcal{L}} \nabla h(\boldsymbol{y}) \right) \right\|^2 \right\}, \tag{4.10}$$

where the Euclidean norm is denoted by $\|\cdot\|$.

The algorithm for solving the Lagrangian variant of the convex optimisation problem, which reduces the magnitude of the largest of the entry vector, can be described as

$$\min_{\boldsymbol{x}} g(\boldsymbol{x}) + h(\boldsymbol{x}) = \min_{\boldsymbol{x}} \lambda_{PMP} \|\boldsymbol{x}\|_\infty + \left\| \hat{\boldsymbol{s}} - \mathbf{H}\boldsymbol{x} \right\|^2, \tag{4.11}$$

where [3] $\lambda_{PMP} = 2^v$ with $v \in \{-12, \cdots, 4\}$. $\|\cdot\|_\infty$ stands for the infinity norm (or $\|\cdot\|_\infty = \max|\cdot|$). The definition of the auxiliary vector for analysing the proximal map $\mathbf{p}_{\mathcal{L}}(\boldsymbol{y})$ is:

$$\boldsymbol{b} = \boldsymbol{y} - \frac{2}{\mathcal{L}} \mathbf{H}^H (\mathbf{H}\boldsymbol{y} - \hat{\boldsymbol{s}}). \tag{4.12}$$

To appraise the proximal map efficiently, both $\alpha$ and a clipping operator $trunc_\alpha(\boldsymbol{b})$ are employed to calculate the signal amplitude level as

$$\alpha = \arg\min_{\tilde{\alpha}} \left\{ \lambda_{PMP}\tilde{\alpha} + \frac{\mathcal{L}}{2} \sum_{i=1}^{N} ([|[\boldsymbol{b}]_i| - \tilde{\alpha}]^+)^2 \right\}, \tag{4.13}$$

$$\boldsymbol{x}[k] = trunc_\alpha(\boldsymbol{b}), \tag{4.14}$$

where $[\Delta]^+ = \max\{\Delta, 0\}$ for $\Delta \in \mathbb{R}$, and $trunc_\alpha(\boldsymbol{b}) = \min\{\max\{\boldsymbol{b}, -\alpha\}, +\alpha\}$. Then, the sequence of the vector $\boldsymbol{x}$ for a constant FITRA step-size is defined as:

$$\boldsymbol{x}[k] = \text{prox}(\boldsymbol{y}[k] - \nabla h(\boldsymbol{y}[k])), \tag{4.15}$$

[3] A regularization parameter, $\lambda_{PMP}$, is used to gain the clipping step in each loop of $Z_{PMP}$.

where $k = 1, 2, \ldots, Z_{PMP}$, and an appropriate step-size $t$ is defined by

$$t[k+1] = \frac{1}{2}(1 + \sqrt{1 + 4t[k]^2}. \tag{4.16}$$

Finally, the sequence of the vector $\boldsymbol{y}$ can be defined as:

$$\boldsymbol{y}[k+1] = \boldsymbol{x}[k] + \frac{t[k]-1}{t[k+1]}(\boldsymbol{x}[k] - \boldsymbol{x}[k-1]). \tag{4.17}$$

### 4.3.1 SNR, PAPR, and OBR Performance Trade-Offs

To modify a conventional PMP to be the adjustable clipping level, two values in the FITRA process need to be considered. Both the FITRA iterations $Z_{PMP}$ and a regularization parameter $\lambda_{PMP}$ have to be automatically adjusted by SER feedback from the terminals. These parameters importantly determine the PAPR signal, out-of-band (power) ratio (OBR), and signal-to-noise ratio (SNR) performance for the MIMO-OFDM systems.

To achieve minimum $E_b/N_0$ it is necessary to minimise SER within 1% with the SNR operating point. In order to measure the amount of signal power that is transmitted outside the active subcarriers $\varepsilon$, the OBR can be shown as:

$$\text{OBR} = \frac{|\varepsilon| \sum_{c \in \varepsilon^c} \|\boldsymbol{x}_c\|_2^2}{\left|\varepsilon^{inac}\right| \sum_{c \in \varepsilon} \|\boldsymbol{x}_c\|_2^2}, \tag{4.18}$$

where $\varepsilon^{inac}$ denotes the inactive OFDM subcarriers with zero-insertion at $\boldsymbol{x}_c = \boldsymbol{0}_{n_t \times 1}$, and $c \in \varepsilon^c$.

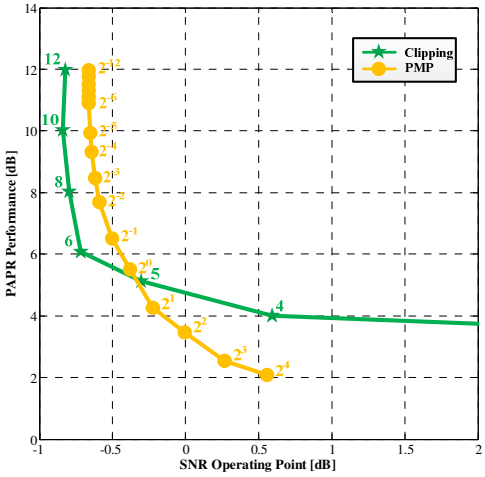


(a) $Z_{PMP} = 250$

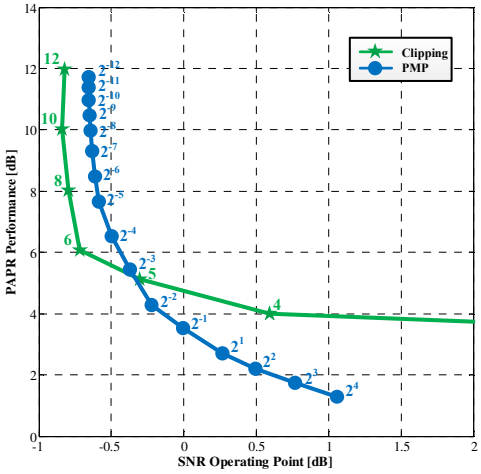


(b) $Z_{PMP} = 500$

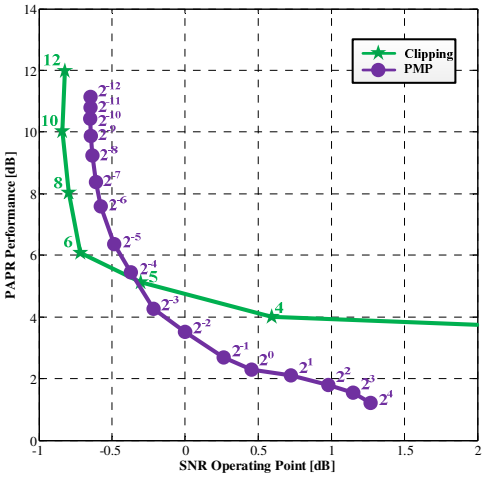


(c) $Z_{PMP} = 1000$

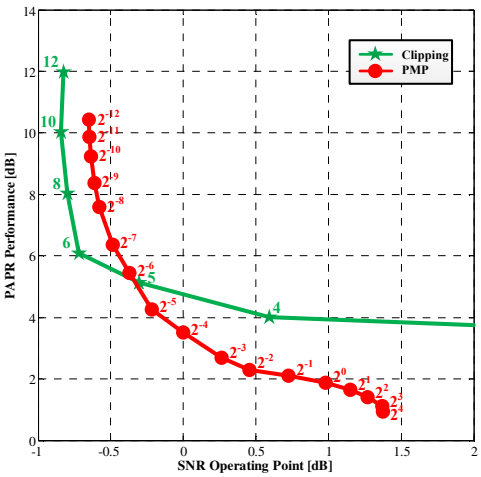


(d) $Z_{PMP} = 2000$

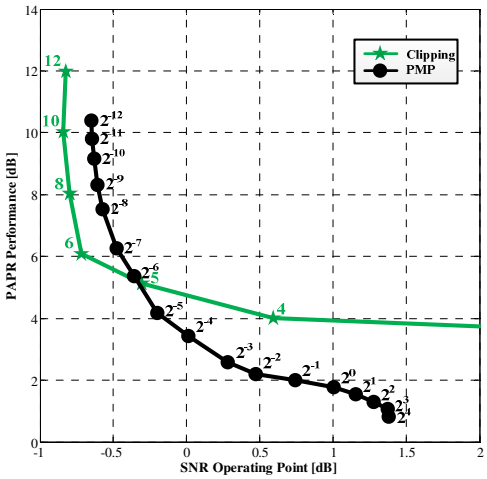


(e) $Z_{PMP} = 3000$

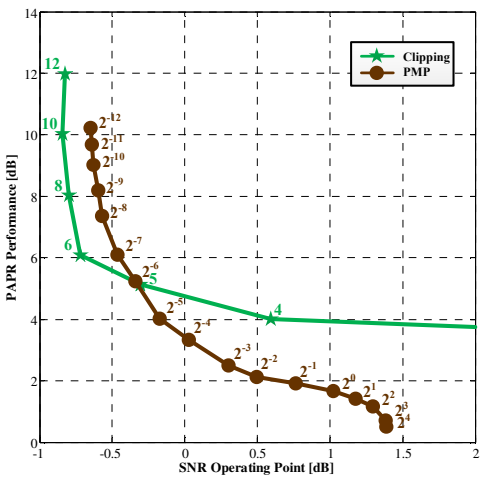


(f) $Z_{PMP} = 4000$

Figure 4.8 SNR and PAPR performance trade-offs of PMP with different FITRA iterations (sourced from [21]).

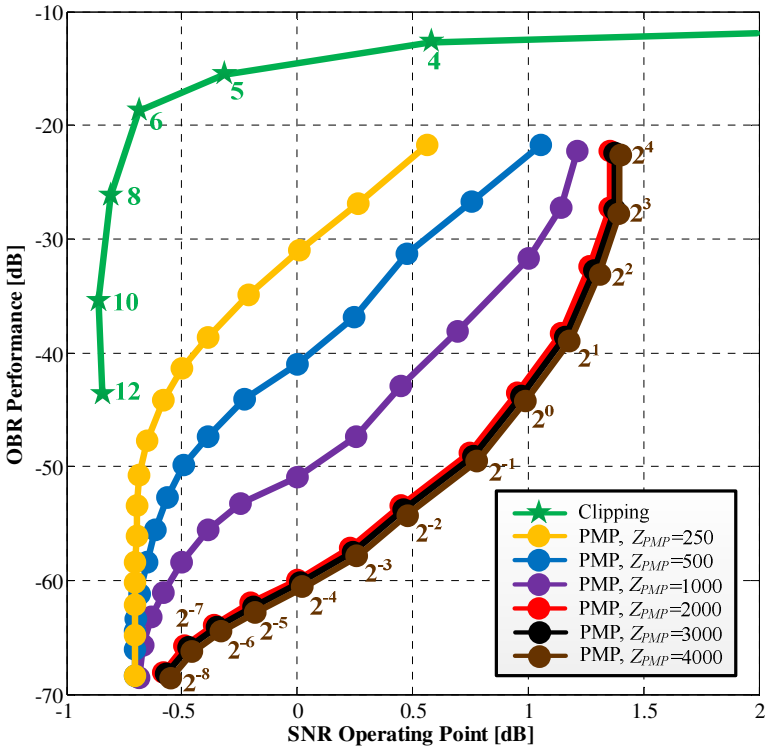


Figure 4.9 SNR and OBR performance trade-offs of PMP (sourced from [21]).

In Figures 4.8 and 4.9, the various FITRA iterations, $Z_{PMP}$, are set with 250, 500, 1000, 2000, 3000 and 4000 respectively. From these values, the PMP scheme can cover [4]a large trade-off region that can be adjusted by the regularization parameter $\lambda_{PMP}$ from $2^{-12}$ to $2^{4}$. In particular, when increasing the value of $\lambda_{PMP}$, the PMP scheme is able to reduce high value of the PAPR. It results in a graceful degradation of the SNR operating point.

In Figure 4.8, the PMP method gives the same performance of the SNR and PAPR trade-offs, whether the FITRA iterations are high or low. Note that in Figure 4.9, it can be clearly seen that the performance of the SNR and OBR trade-offs is different with those FITRA iterations. In case of low iterations (i.e. $Z_{PMP}$ = 250, 500, and 1000), they increase OBR, causing high error rate in the systems and causing $E_b/N_0$ to increase. On the other hand, the OBR performances are reduced by the high number of the FITRA iterations (i.e. $Z_{PMP}$ = 2000, 3000, and 4000). For this case, their OBR performance is nearly the same. As a result, the maximum loop of the

[4] A large trade-off region is where OBR ≈ -22 dB to -70 dB, and SNR ≈ -0.75 dB to 1.4 dB respectively.

FITRA iteration is assumed to be limited at 2000 because it gives the lowest complexity.

The trade-off between the high value and the low value of $\lambda_{PMP}$ is the exchange of performance between OBR and PAPR. When $\lambda_{PMP}$ is increased it negatively affects the system as a consequence of OBR distortion. Fortunately, a benefit is that the high dynamic range of $\tilde{x}(t)$ is also reduced by an amount $\lambda_{PMP}$. Therefore, by adjusting the $\lambda_{PMP}$ in response to the average SER from all users, the novel FITRA process is devised, to be described in the next section.

### 4.3.2 The FITRA Algorithm Controlled with SER Feedback

As shown in Figures 4.8 and 4.9, the range of the regularization parameter varies from $2^{-12}$ to $2^{4}$. When $\zeta$ is high, $\lambda_{PMP}$ needs to be low for decreasing the level of $\alpha$. Therefore, both Eq. (4.11) and Eq. (4.13), the variable clipping level of FITRA algorithm can be represented as

$$\beta(\zeta) = \arg\min_{\tilde{\alpha}} \left\{ \lambda(\zeta)_{PMP}\tilde{\alpha} + \frac{\mathcal{L}}{2}\sum_{i=1}^{N}([|[\boldsymbol{b}]_i| - \tilde{\alpha}]^{+})^2 \right\}, \tag{4.19}$$

where $\lambda(\zeta)_{PMP} = 2^{(4-16\zeta)}$.

In Eq. (4.19), it is the important equation that changes the conventional FITRA algorithm to be adjusted by users' SER. In the worst case of the MIMO channel ($E_b/N_0$ is in the low region), all users cannot send the SER feedbacks to a BS. In this case, the $\zeta$ is equal to one, and then the $\lambda(\zeta)_{PMP}$ is set to $2^{-12}$. The $\beta(\zeta)$ will be increased as the same level as $\tilde{x}_{\beta_{\max}}$. On the other hand, in the case of the low noise channel ($E_b/N_0$ is in the high region), the $\zeta$ is equal to zero, and then the $\lambda(\zeta)_{PMP}$ is set to $2^{4}$. The $\beta(\zeta)$ will be decreased as the same level as $\tilde{x}_{\beta_{\min}}$. Finally, the modified FITRA algorithm with the variable clipping level controlled with SER feedback can be shown as Algorithm 3 in Appendix D.

## 4.4 Summary

In this chapter are proposed the novel tools for variable PAPR clipping level by using feedback SER from all users in the WLAN cell. Both a CP and a PMP method are chosen to modify from the fixed clipping level to be the adjustable clipping level. By the advantage of the SER feedback, the new tools of the PAPR reduction can be adapted themselves to the situation of the MIMO channel effectively. The purpose of this chapter has been to provide the new tools to work with the APO, which are presented in the next chapter.

# Chapter 5

# The Adaptive PAPR Optimizer

This chapter presents a tool that is used for equalising the clipped signal from PAPR reductions. The Adaptive PAPR Optimizer (APO) is based on an adaptive filter that may be understood as a self-modifying digital filter. It adjusts itself by its coefficients in order to adjust an error function. This error function, also called the cost function, is a distance measurement between the reference or desired signal and the output of the adaptive filter.

The APO uses the CSI to adapt its algorithm by SER feedback from all users. It is also cooperated with the adjustable PAPR reduction level techniques in the previous chapter. Both LMS and RLS algorithms are modified to use in the APO in order to improve the SER performance in the large-scale MIMO-OFDM system.

## 5.1 The Adaptive Filter

The basic concept of an adaptive filter is illustrated in Figure 5.1. The input signal is denoted by $\tilde{x}_{\beta(\zeta)}[k]$, the reference signal $\tilde{x}[k]$ represents the desired output signal, $x_{optz}[k]$ is the output of the adaptive filter, and the error signal is defined as $e[k] = \tilde{x}[k] - x_{optz}[k]$ respectively.

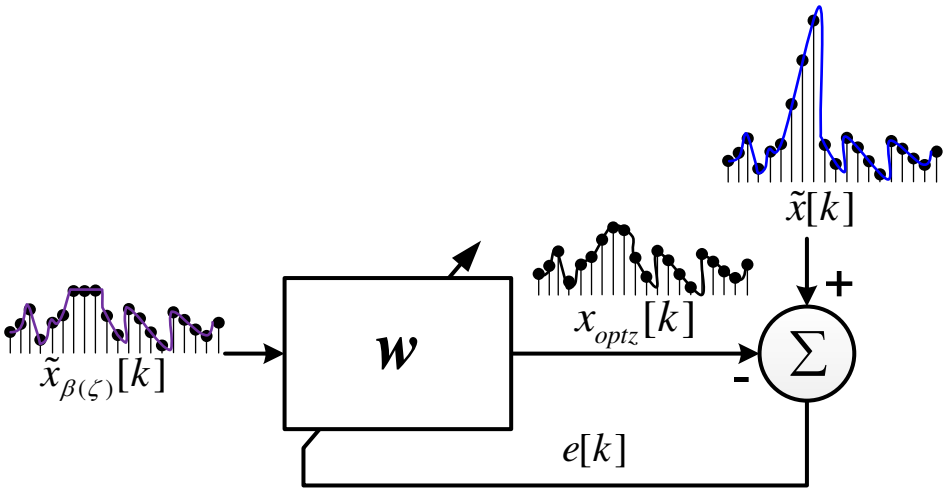


Figure 5.1 The simple block diagram of an adaptive filter.

In Figure 5.1, $e[k]$ is employed by the adaptive algorithm to update the adaptive filter coefficient, $\boldsymbol{w}[k]$. The whole adaptation process generally aims at optimising some metric of $e[k]$, producing the $x_{optz}[k]$ to approximate $\tilde{x}[k]$ in a statistical sense.

## 5.2 The Foundation of the APO

The classical research work between a PAPR reduction and a digital filter was presented by J. Armstrong in [81]. In this section, the proposed technique, called *an Adaptive PAPR Optimizer (APO)*, is developed from this idea. The difference between an adaptive filter and the APO is the operational area in the cost function of weight vectors, $J(\boldsymbol{w})$, based on the steepest-descent theory [101]. The cost function can be mathematically presented as the mean squared error between $\tilde{\boldsymbol{x}}$ and $\tilde{\boldsymbol{x}}_{\beta(\zeta)}$, multiplied with $\boldsymbol{w}$. It can be shown as

$$\begin{aligned} J(\boldsymbol{w}) &\triangleq E\left|\tilde{\boldsymbol{x}}-\tilde{\boldsymbol{x}}_{\beta(\zeta)}\boldsymbol{w}\right|^2 = E\left(\tilde{\boldsymbol{x}}-\tilde{\boldsymbol{x}}_{\beta(\zeta)}\boldsymbol{w}\right)\left(\tilde{\boldsymbol{x}}-\tilde{\boldsymbol{x}}_{\beta(\zeta)}\boldsymbol{w}\right)^* \\ &= \sigma_{\tilde{\boldsymbol{x}}}^2 - R^*_{\tilde{\boldsymbol{x}},\tilde{\boldsymbol{x}}_{\beta(\zeta)}}\boldsymbol{w} - \boldsymbol{w}^* R_{\tilde{\boldsymbol{x}},\tilde{\boldsymbol{x}}_{\beta(\zeta)}} + \boldsymbol{w}^* R_{\tilde{\boldsymbol{x}}_{\beta(\zeta)}}\boldsymbol{w} \\ &= \begin{bmatrix} 1 & \boldsymbol{w}^* \end{bmatrix} \cdot \begin{bmatrix} \sigma_{\tilde{\boldsymbol{x}}}^2 & -R_{\tilde{\boldsymbol{x}}_{\beta(\zeta)},\tilde{\boldsymbol{x}}} \\ -R_{\tilde{\boldsymbol{x}},\tilde{\boldsymbol{x}}_{\beta(\zeta)}} & R_{\tilde{\boldsymbol{x}}_{\beta(\zeta)}} \end{bmatrix} \cdot \begin{bmatrix} 1 \\ \boldsymbol{w} \end{bmatrix}, \end{aligned} \tag{5.1}$$

where $\sigma_{\tilde{\boldsymbol{x}}}^2 = E\left|\tilde{\boldsymbol{x}}\right|^2$ is the variance of $\tilde{\boldsymbol{x}}$, $R_{\boldsymbol{A}} \triangleq E\left[\boldsymbol{A}^*\boldsymbol{A}\right]$ is the covariance of $\boldsymbol{A}$, and $R_{\boldsymbol{A},\boldsymbol{B}} \triangleq E\left[\boldsymbol{A}^*\boldsymbol{B}\right]$ is the cross-covariance of $\boldsymbol{A}$ and $\boldsymbol{B}$.

In the last line of (5.1), the centre matrix can be factored into a product of upper-triangular, diagonal, and lower-triangular block matrices as

$$\begin{bmatrix} \sigma_{\tilde{\boldsymbol{x}}}^2 & -R_{\tilde{\boldsymbol{x}}_{\beta(\zeta)},\tilde{\boldsymbol{x}}} \\ -R_{\tilde{\boldsymbol{x}},\tilde{\boldsymbol{x}}_{\beta(\zeta)}} & R_{\tilde{\boldsymbol{x}}_{\beta(\zeta)}} \end{bmatrix} = \begin{bmatrix} 1 & -R_{\tilde{\boldsymbol{x}}_{\beta(\zeta)},\tilde{\boldsymbol{x}}} R_{\tilde{\boldsymbol{x}}_{\beta(\zeta)}}^{-1} \\ 0 & 1 \end{bmatrix} \cdot \begin{bmatrix} \sigma_{\tilde{\boldsymbol{x}}}^2 - R_{\tilde{\boldsymbol{x}}_{\beta(\zeta)},\tilde{\boldsymbol{x}}}^{-1} R_{\tilde{\boldsymbol{x}}_{\beta(\zeta)}}^{-1} R_{\tilde{\boldsymbol{x}},\tilde{\boldsymbol{x}}_{\beta(\zeta)}} & 0 \\ 0 & R_{\tilde{\boldsymbol{x}}_{\beta(\zeta)}} \end{bmatrix} \cdot \begin{bmatrix} 1 & 0 \\ -R_{\tilde{\boldsymbol{x}}_{\beta(\zeta)}}^{-1} R_{\tilde{\boldsymbol{x}},\tilde{\boldsymbol{x}}_{\beta(\zeta)}} & 1 \end{bmatrix}. \tag{5.2}$$

Substituting from (5.2) into (5.1), the cost function of the optimum weight vector of the APO can be shown as

$$\begin{aligned} J\left(\boldsymbol{w}^o\right) \triangleq J\left(\boldsymbol{w}[0]\right) \leftrightarrow J\left(\boldsymbol{w}_{\beta'(\zeta)}\right) \\ = \left(\boldsymbol{w} - R_{\tilde{\boldsymbol{x}}_{\beta(\zeta)}}^{-1} R_{\tilde{\boldsymbol{x}},\tilde{\boldsymbol{x}}_{\beta(\zeta)}}\right)^* R_{\tilde{\boldsymbol{x}}_{\beta(\zeta)}} \left(\boldsymbol{w} - R_{\tilde{\boldsymbol{x}}_{\beta(\zeta)}}^{-1} R_{\tilde{\boldsymbol{x}},\tilde{\boldsymbol{x}}_{\beta(\zeta)}}\right) + \left(\sigma_{\tilde{\boldsymbol{x}}}^2 - R_{\tilde{\boldsymbol{x}}_{\beta(\zeta)},\tilde{\boldsymbol{x}}} R_{\tilde{\boldsymbol{x}}_{\beta(\zeta)}}^{-1} R_{\tilde{\boldsymbol{x}},\tilde{\boldsymbol{x}}_{\beta(\zeta)}}\right), \\ \boldsymbol{w}[0] \le \boldsymbol{w} \le \boldsymbol{w}_{\beta'(\zeta)}, \end{aligned} \tag{5.3}$$

where $\boldsymbol{w}^o$ is the optimum weight vector, $\boldsymbol{w}[0]$ is the initial weight vector where $\boldsymbol{x}_{optz}$ is the same as $\tilde{\boldsymbol{x}}_{\beta(\zeta)}$, and $\boldsymbol{w}_{\beta'(\zeta)}$ is the weight vector where $\boldsymbol{x}_{optz}$ is the same level as $\tilde{\boldsymbol{x}}_{\beta(\zeta)}$ and also the same characteristic as $\tilde{\boldsymbol{x}}$.

The $J\left(\boldsymbol{w}\right)$ is approximated to zero by selecting $\boldsymbol{w}$ as $\boldsymbol{w}_{min}$ with $R_{\tilde{\boldsymbol{x}}_{\beta(\zeta)},\tilde{\boldsymbol{x}}} > 0$ [101]. Then, the result of the minimum error is given by

$$J_{min} \triangleq J\left(\boldsymbol{w}_{min}\right) = \sigma_{\tilde{\boldsymbol{x}}}^2 - R_{\tilde{\boldsymbol{x}}_{\beta(\zeta)},\tilde{\boldsymbol{x}}} R_{\tilde{\boldsymbol{x}}_{\beta(\zeta)}}^{-1} R_{\tilde{\boldsymbol{x}},\tilde{\boldsymbol{x}}_{\beta(\zeta)}}. \tag{5.4}$$

For the adaptive filtering task, $\boldsymbol{w}^o$ is the minimum value found for $J_{min}$; however, for the APO, $\boldsymbol{w}^o$ is the weight vector around the operational area that varies from $J\left(\boldsymbol{w}[0]\right)$ to $J\left(\boldsymbol{w}_{\beta'(\zeta)}\right)$.

$J_{min}$ has a unique minimum at $\boldsymbol{w}_{min} = R^{-1}_{\tilde{\boldsymbol{x}}_{\beta(\zeta)}} R_{\tilde{\boldsymbol{x}},\tilde{\boldsymbol{x}}_{\beta(\zeta)}}$ with minimum value given by Eq. (5.4).

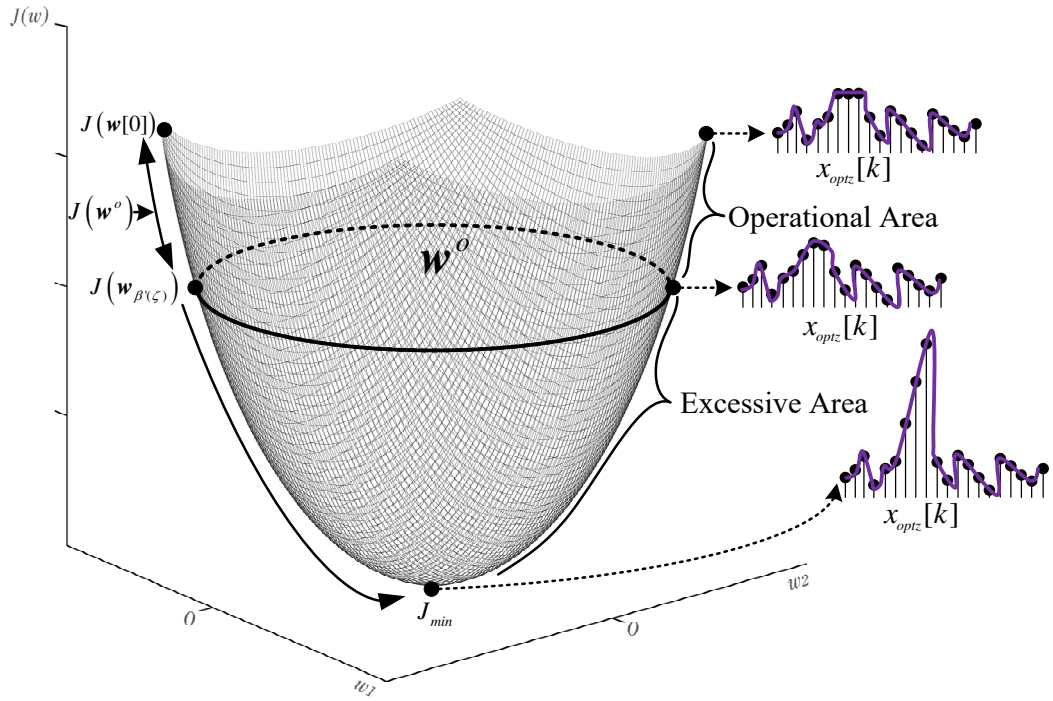


Figure 5.2 Operational area of the APO.

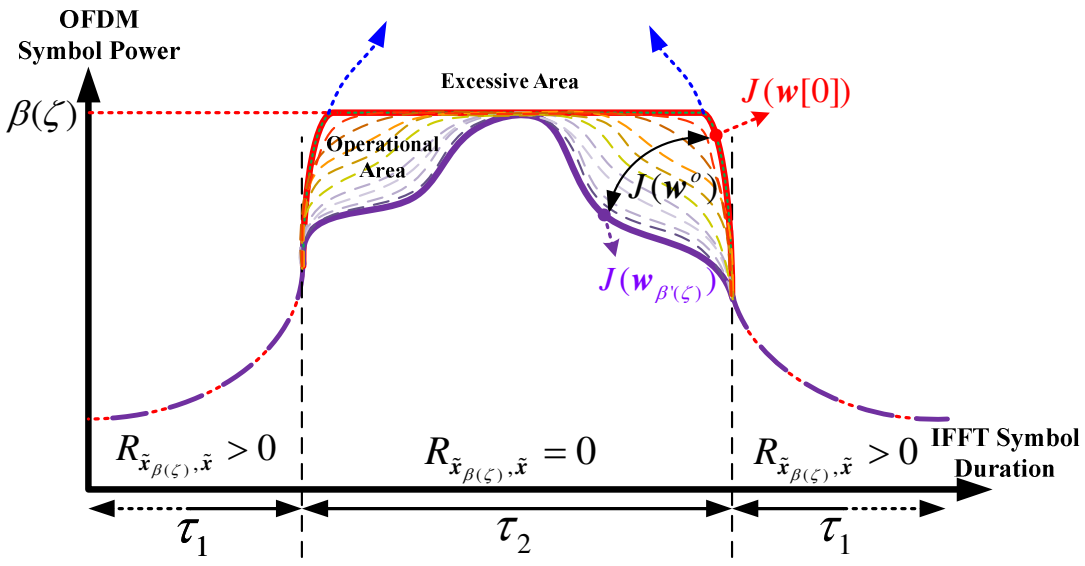


Figure 5.3 OFDM-PAPR adjustment over a symbol interval.

Figure 5.2 shows both the operational area and the excessive area of an adaptive filter in a typical plot of $J(\boldsymbol{w})$ for the case in which $\boldsymbol{w}$ is two-dimensional. While $\boldsymbol{x}_{optz}$ peaks are higher than the level $\beta(\zeta)$ in the excessive area that varies from $J(\boldsymbol{w}_{\beta'(\zeta)})$ to $J_{min}$, they increase the average power of PAPR in systems affecting to power amplifiers at the transmitter. Therefore, a threshold value with $J(\boldsymbol{w}^o)$ to limit the adaptive filter to operate in the operational area is set.

In the adjustable peak period, $\tau_2$, there are different characteristics between $\tilde{\boldsymbol{x}}_{\beta(\zeta)}$ and $\tilde{\boldsymbol{x}}$ (or orthogonal) that need to optimise for $\boldsymbol{x}_{optz}$ in this time because the cross-correlation $R_{\tilde{\boldsymbol{x}}_{\beta(\zeta)},\tilde{\boldsymbol{x}}} = 0$. It affects $J(\boldsymbol{w})$ operated in the operational area limited with $J(\boldsymbol{w}^o)$.

Figure 5.3 demonstrates the adjustable peak period and the unaltered peak period, $\tau_1$, of the APO in the time domain of $\tilde{\boldsymbol{x}}$, $\tilde{\boldsymbol{x}}_{\beta(\zeta)}$, and $\boldsymbol{x}_{optz}$. There is the duration at $\tau_1$ that both $\tilde{\boldsymbol{x}}$ and $\tilde{\boldsymbol{x}}_{\beta}$ are completely correlated (or non-orthogonal). For this time, the APO works with $J(\boldsymbol{w})$ that is moved to $J(\boldsymbol{w}_{min})$. In other words, both $\tilde{\boldsymbol{x}}$ and $\tilde{\boldsymbol{x}}_{\beta}$ are the same as $\boldsymbol{x}_{optz}$ in $\tau_1$ at the beginning $\boldsymbol{w}[0]$. Therefore, the synthesized output signal by the APO is processed in $\tau_2$ only. The cost function of the APO can be expressed as

$$J(\boldsymbol{w}) = \begin{cases} J(\boldsymbol{w}^o), & \text{if } \tau = \tau_1 \\ J(\boldsymbol{w}_{min}), & \text{if } \tau = \tau_2 \end{cases}. \tag{5.5}$$

There are many algorithms to update the weighted coefficient of APO. The time duration of the convergence is the important parameter for choosing an algorithm for the APO. The main focus of this thesis is to study two algorithms, being the LMS algorithm and the RLS algorithm.

## 5.3 The Variable Step-size LMS Algorithm

The LMS algorithm was devised by Widow and Hoff to use in the training neural networks [102]. It is based on the steepest-descent method, in that weights are adapted by repeatedly minimising the mean square error. The important part of the LMS algorithm is to employ a rough approximation for the gradient, instead of using a calculation for the gradient at every step [103].

The updated error of the conventional LMS algorithm (or fixed-step-size (FS)), operating in the discrete-time domain $k$, can be expressed as

$$e[k] = \tilde{x}[k] - \boldsymbol{w}^T[k]\tilde{x}_{\beta(\zeta)}[k], \tag{5.6}$$

and an approximation of the gradient by using the updated error multiplied with the desired output is found by

$$\Delta_{LMS} = e[k]\tilde{x}_{\beta(\zeta)}[k]. \tag{5.7}$$

Substituting (5.7) into (5.6), the updated weight coefficient based on steepest-descent can be shown by

$$w[k+1] = w[k] - \mu e[k] * \tilde{x}_{\beta(\zeta)}[k]. \tag{5.8}$$

where $\mu$ is the FS of the LMS algorithm.

For the variable step-size (VS) LMS algorithm controlled with SER feedback, it is firstly proposed from [30-31]. It means that a step-size, $\mu$, in (5.8) is controlled with average SER. Then, a weight coefficient of VS-LMS can be expressed as

$$\begin{aligned} w[k+1] &= w[k] + \mu[k]e[k] * \tilde{x}_{\beta(\zeta)}[k], \quad k \geq 0, \\ \mu[k+1] &= \delta\mu[k] + \rho\varphi^2[k], \\ \varphi[k+1] &= \xi\varphi[k] + \upsilon[1-\zeta], \end{aligned} \tag{5.9}$$

where $\mu[k]$ is the variable step-size of the LMS algorithm; $\delta, \rho, \xi,$ and $\upsilon$ are non-negative values that are in the range from 0 to 1, $\zeta$ is the average SER from all terminals.

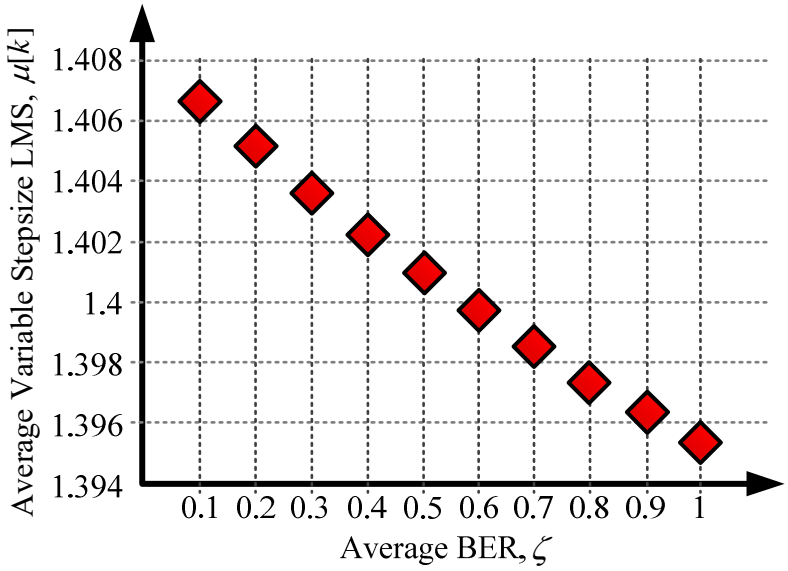


Figure 5.4 Relationship between average variable step-size and average SER ( $\mu[0] = 0, \varphi[0] = 1, \delta = 0.999,$ $\zeta[0] = 1, \rho = 0.001, \xi = 0.999,$ and $\vartheta = 0.00001$ ).

Figure 5.4 shows that the average variable step-size of the proposed LMS algorithm decreases as the average SER increases. It means that the updated weight vector $w[k+1]$ in (5.9) is slightly changed when the transmission channel is more ill-behaved. By this situation, it affects its weight vector changing towards a new updated value. Finally, $J(\boldsymbol{w})$ is precisely converged to the $J(\boldsymbol{w}^o)$.

Finally, the FIR is utilized as the main structure of the APO. Then, the optimised signal is shown as

$$x_{optz} = \sum_{l=0}^{L-1} w_l \tilde{x}_{\beta(\zeta)}[k-l], \tag{5.10}$$

where $L$ denotes the length of the APO.

## 5.4 The Variable Forgetting Factor RLS Algorithm

It has been widely known that the convergence rate of the RLS algorithm is faster than the LMS algorithm [101]. Moreover, the variable forgetting factor RLS is useful when its filter coefficients which are close to the $J_{\min}$; a small step of the forgetting

factor is used for this case; otherwise a large step-size of the forgetting factor is applied instead. The conventional RLS algorithm is based on the least squares method. The mathematical procedure of least squares method is employed for finding the best fitting curve to a given set of the data points [102-103]. The aim of the RLS algorithm is to minimize the sum of the offset squares from the fitting curve.

The constants of both a fixed-forgetting factor (FFF), $\chi$, and a regularization parameter, $\delta$, are initially set by the BS. Normally, the forgetting factor should be less than one ($\delta < 1$). Therefore, the FFF-RLS algorithm can be shown as follows [104-106]:

$$k[k] = \frac{\Theta[k-1]\tilde{x}_{\beta(\zeta)}[k]}{\chi + \tilde{x}_{\beta(\zeta)}[k]\Theta[k-1]\tilde{x}_{\beta(\zeta)}[k]}, \tag{5.11}$$

where $k[k]$ is the Kalman gain, [1] $\Theta[k]$ is an inverse correlation matrix of the input signal.

The complex conjugate of an estimation error, $e[k]^*$, for RLS is based on

$$\begin{aligned} e[k] &= \tilde{x}[k] - w[k-1]\tilde{x}_{\beta(\zeta)}[k], \\ w[k] &= w[k-1] + k[k]e[k]^*, \\ \Theta[k] &= \frac{\Theta[k-1] - k[k]\tilde{x}[k]\Theta[k-1]}{\chi}, \end{aligned} \tag{5.12}$$

where $w[k]$ is the weight vector of the RLS algorithm.

To modify the conventional RLS algorithm to be the variable forgetting factor (VFF) RLS algorithm [30-31, 107-109], the Kalman gain from (5.11) can be replaced as

$$k[k] = \frac{\Theta[k-1]\tilde{x}_{\beta(\zeta)}[k]}{\chi[k] + \tilde{x}_{\beta(\zeta)}[k]\Theta[k-1]\tilde{x}_{\beta(\zeta)}[k]}, \tag{5.13}$$

where $\chi[k]$ is the variable forgetting factor.

The value of $\Theta[k]$ should be controlled by the average SER that can be used for controlling the gain of $\chi[k]$ through

[1] An initial values of $\Theta[0]$ is $\delta^{-1}\mathbf{I}_{L\times L}$; and $\delta$ is small positive constant.

$$\varphi[k] = \xi\varphi[k-1] + \vartheta(1-\zeta), \tag{5.14}$$

where $\xi$ is a front gain, and $\vartheta$ is a back gain.

Finally, the updated inverse correlation matrix for the VFF-RLS algorithm can be proposed as follows

$$\begin{aligned}
&\text{sign}\left[z[k]\right] = \text{sign}\left[e[k]e[k-1]\right]\cdot\text{sign}\left[\tilde{x}_{\beta(\zeta)}[k]k[k-1]\right],\\
&\psi[k] = \left(1+\rho\,\text{sign}\left[z[k]\right]\right)\left(1-\chi[k-1]\right),\\
&\chi[k] = 1-\psi[k],\\
&\Theta[k] = \frac{\varpi}{\varphi^2[k-1]\chi[k]}\left(\Theta[k-1]-k[k]\tilde{x}[k]\Theta[k-1]\right),
\end{aligned} \tag{5.15}$$

where $\text{sign}[\cdot]$ is the sign function; $\rho$ and $\varpi$ are the positive values that are in the range of 0 to 1.

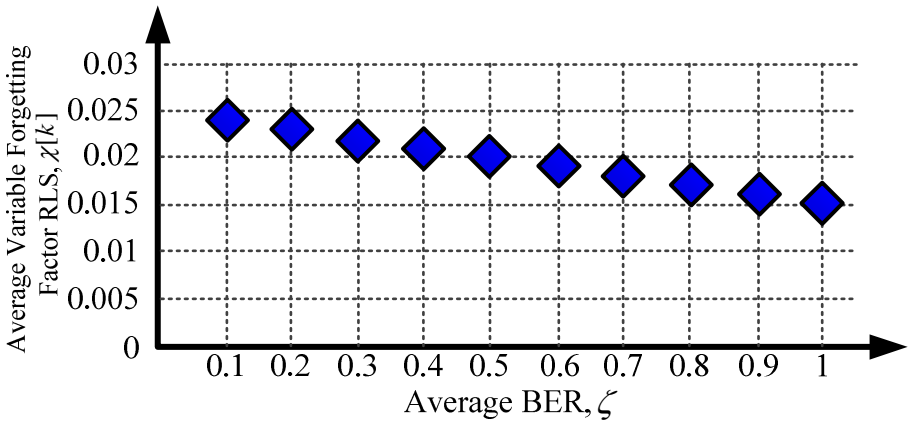


Figure 5.5 Relationship between average variable forgetting factor and average SER ( $\chi[0] = 0, \varphi[0] = 1, \delta = 0.999,$ $\xi = 0.999, \vartheta = 0.00001,$ and $\zeta[0] = 1$ ).

As shown in (5.14) and Figure 5.5, both $\xi$ and $\vartheta$ are the non-negative values that are in the range of 0 to 1. The $\xi$ is used to amplify the previous value of $\varphi[k]$, which is varied by the term $\vartheta(1-\zeta)$. When the channel has a lot of noise and the $\zeta$ is high, $\varphi[k]$ is adjusted itself by the reduced gain of $\chi[k]$ in (5.15) appropriately. Then, $\Theta[k]$ is increased by the term of $\varphi^2[k-1]\chi[k]$. By this situation, it affects the $k[k]$ in (5.13) and the $w[k]$ in (5.12) changing dramatically towards the new appropriate value. As the results, $J(\boldsymbol{w})$ is converged to the $J(\boldsymbol{w}^o)$ correctly [110-111].

This chapter presents a tool to improve the function of the variable PAPR reductions in the MU large-scale MIMO-OFDM systems. The APO is based on the adaptive FIR filter worked with the variable PAPR reductions. It can be shown in Figure 5.6. It is not a PAPR reduction by itself but it optimises different signals. This difference is between the outputs of PAPR reduction schemes and the original input with high dynamic range. The proposed algorithms of this chapter are both the VS-LMS algorithm and the VFF-RLS algorithm. As mentioned above, these algorithms utilize users' feedback to adjust themselves to be compatible with the environment of the channel effectively.

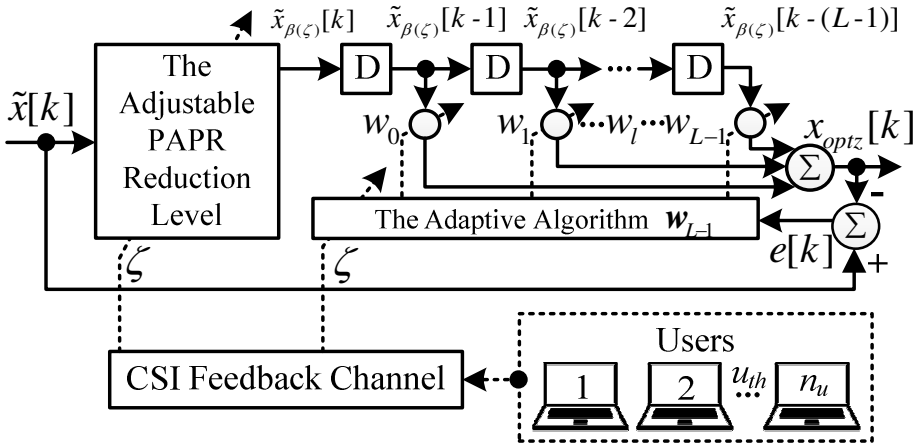


Figure 5.6 [2]The APO cooperated with the adjustable PAPR reduction level.

## 5.5 The Overhead by the Signal Repetition of the Algorithms

In the case of the implementation process, the transient behaviour duration (or convergent duration) needs to be avoided in the initial period of the adaptive algorithm. The longer initial time that it takes, the higher is the error caused by the imperfection of the transmitted signal, $x_{optz}$, which it gets. To prevent the resulting error, in this thesis we will only consider the output signal at the steady state period. Therefore, a number of the repetitions of both $\tilde{x}$ and $\tilde{x}_{\beta(\zeta)}$ are added by modifying in (5.10) be the concatenated form as

[2] A block diagram of 'D' is symbolised as a discrete-time delay.

$$x_{optz} = \sum_{l=0}^{L-1} w_l \left[ \sum_{n=1}^{N_{rep}} \tilde{x}_{\beta(\zeta),n}[k-l] \right], \tag{5.16}$$

where $N_{rep}$ is the total number of the signal repetitions; and $\sum_{n=1}^{N_{rep}} \tilde{x}_{\beta(\zeta),n}[k] = \left[ \tilde{x}_{\beta(\zeta),1}[k], \tilde{x}_{\beta(\zeta),2}[k], \cdots, \tilde{x}_{\beta(\zeta),N_{rep}}[k] \right]$.

The transmitted vector for the total number of antennas $n_t$ at the BS is expressed as

$$\boldsymbol{x}_{optz} = \sum_{l=0}^{L-1} \boldsymbol{w}_l \left[ \sum_{t=1}^{n_t} \sum_{n=1}^{N_{rep}} \tilde{\boldsymbol{x}}^t_{\beta,n}[k-l] \right] = \begin{bmatrix} \sum_{l=0}^{L-1} w_l \left[ \tilde{x}^1_{\beta(\zeta),1}[k-l], \tilde{x}^1_{\beta(\zeta),2}[k-l], \cdots, \tilde{x}^1_{\beta(\zeta),N_{rep}}[k-l] \right] \\ \sum_{l=0}^{L-1} w_l \left[ \tilde{x}^2_{\beta(\zeta),1}[k-l], \tilde{x}^2_{\beta(\zeta),2}[k-l], \cdots, \tilde{x}^2_{\beta(\zeta),N_{rep}}[k-l] \right] \\ \vdots \\ \sum_{l=0}^{L-1} w_l \left[ \tilde{x}^{n_t}_{\beta(\zeta),1}[k-l], \tilde{x}^{n_t}_{\beta(\zeta),2}[k-l], \cdots, \tilde{x}^{n_t}_{\beta(\zeta),N_{rep}}[k-l] \right] \end{bmatrix}. \tag{5.17}$$

Concurrently, to compare the complexities between the conventional systems in [37, 49] and our proposed scheme, the output of the transmission in (5.17) is substituted into

$$\boldsymbol{x}_{\Omega_{ZF}} = \Omega_{ZF} \boldsymbol{x}_{optz} = \sqrt{\frac{n_u}{Tr\left( \left( \mathbf{G}\mathbf{G}^H \right)^{-1} \right)}} \Gamma \left[ \mathfrak{F}^{-1} \left[ \mathbf{H}^{\dagger} \boldsymbol{s} \right] \right], \tag{5.18}$$

where $\boldsymbol{x}_{optz} = \Gamma\left[\tilde{\boldsymbol{x}}\right]$, which is the optimised signal vector. Then, the output of the transmission can be expressed as

$$\boldsymbol{x}_{\Omega_{ZF}} = \underbrace{\sqrt{\frac{n_u}{Tr\left( \left( \mathbf{G}\mathbf{G}^H \right)^{-1} \right)}}}_{\Omega_{ZF}} \underbrace{\sum_{l=0}^{L-1} \boldsymbol{w}_l \left[ \sum_{t=1}^{n_t} \sum_{n=1}^{N_{rep}} \tilde{\boldsymbol{x}}^t_{\beta(\zeta),n}[k-l] \right]}_{\sum_{t=1}^{n_t} \tilde{\boldsymbol{x}}^t_{\beta(\zeta),n}[k]}. \tag{5.19}$$

Due to the initial value of $J\left(\boldsymbol{w}\left(0\right)\right)$ for the APOs, a PMP approach is closer to $J\left(\boldsymbol{w}^o\right)$ than a clipping approach. In other words, the APO-PMP method converges to the steady state by using a number of iterations less than those of APO-CP. Therefore, APO-CP uses more signal repetitions than those of APO-PMP. Moreover, with the enhancement of step-size controlled by SER, the variable step-size adaptive

algorithm is able to find the appropriated weights deploying the least iteration compared with the FS algorithm. As a result, the number of signal repetitions from the variable step-size is less than the FS adaptive algorithm for both the CP and the PMP scheme. The variations of the average coefficient of both a FS-LMS and a variable step-size LMS are described in Figure 5.7 (a). The advantage of CSI by using feedback SER is employed from all terminals to control the step-size of the LMS algorithm. By this technique, the speed of the convergent process with the VS-LMS (solid-lines) consumes the iteration number less than the FS-LMS (dashed lines) in the term of both a CP (red lines) and a PMP scheme (blue lines). Therefore, the redundancy of the number of $N_{rep}$ in the system from the variable step-size is less than the FS for all APOs ($N_{rep}$ = 4, $N_{rep}$ = 3, $N_{rep}$ = 2, and $N_{rep}$ = 1 for the FS-LMS-CP, the VS-LMS-CP, the FS-LMS-PMP, and the VS-LMS-PMP respectively).

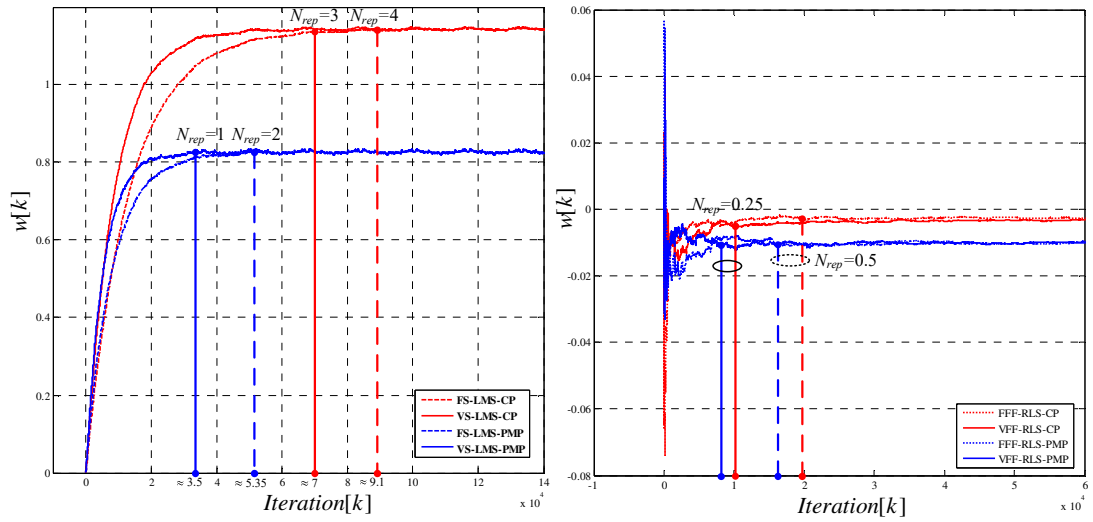


(a) LMS Algorithm (b) RLS Algorithm

Figure 5.7 The convergence process of APOs both the FS and the variable step-size.

For similar reasons to those used for the LMS algorithm, in Figure 5.7 (b), it appears clear that the variable forgetting factor RLS is superior to the FFF-RLS. They can be shown as $N_{rep}$ = 0.25 for both the VFF-RLS-CP and the VFF-RLS-PMP (solid-lines); $N_{rep}$ = 0.5 for both the FFF-RLS-CP and the FFF-RLS-PMP (dashed-lines). Moreover, both Figure 5.7 (a) and Figure 5.7 (b), the RLS algorithm apparently reduces the total number of the signal repetition more than 75% at the same number of the iteration of the LMS algorithm.

One disadvantage of the APO is that it is more complex than regular PAPR reductions. Note that in (5.17), the key factors for the apparent complexity come from both the length of the APO, $L$, and the total number of the signal repetition, $N_{rep}$. First, the length of the APO depends on its main structure. If its length is short, the complexity of its system is less. Secondly, the signal repetition, $N_{rep}$, will be reduced in the adaptive algorithm. When its algorithm is more intelligent, the convergent period is short. In other words, if the convergent duration is reduced, the number of $N_{rep}$ is decreased accordingly. In summary, the key solutions for reducing the system complexity depend on both the main structure and the adaptive algorithm. This should be improved in the future.

To simplify the process of the APO, both FS and variable step-size of the LMS algorithms controlled with SER feedback can be expressed as Algorithm 4 in Appendix D.

Moreover, both the FFF-RLS and the proposed variable forgetting factor RLS algorithm can be simply expressed as Algorithm 5 in Appendix D.

Finally, the large-scale MIMO-OFDM system, which is used in this thesis, can be shown in Figure 5.7.

## 5.6 Summary

This chapter provided a novel tool to assist the variable PAPR reduction schemes which were presented in Chapter 4. The proposed technique, an APO for equalising the clipped signals was shown in this chapter. Section 5.1 reviewed the basic concept of an adaptive filter, which is the foundation of the APO. Both VS-LMS and VFF-RLS were invented in section 5.2 and 5.3 respectively. Moreover, in the case of imperfect CSI mode, both section 5.2 and 5.3 also provided the FS algorithms for this situation.

With cooperation between the variable clipping PAPR level techniques in chapter 4 and the APO in this chapter, this cooperation can improve the system performance of the MU large-scale MIMO-OFDM systems effectively. All simulation results will be shown in Chapter 7.

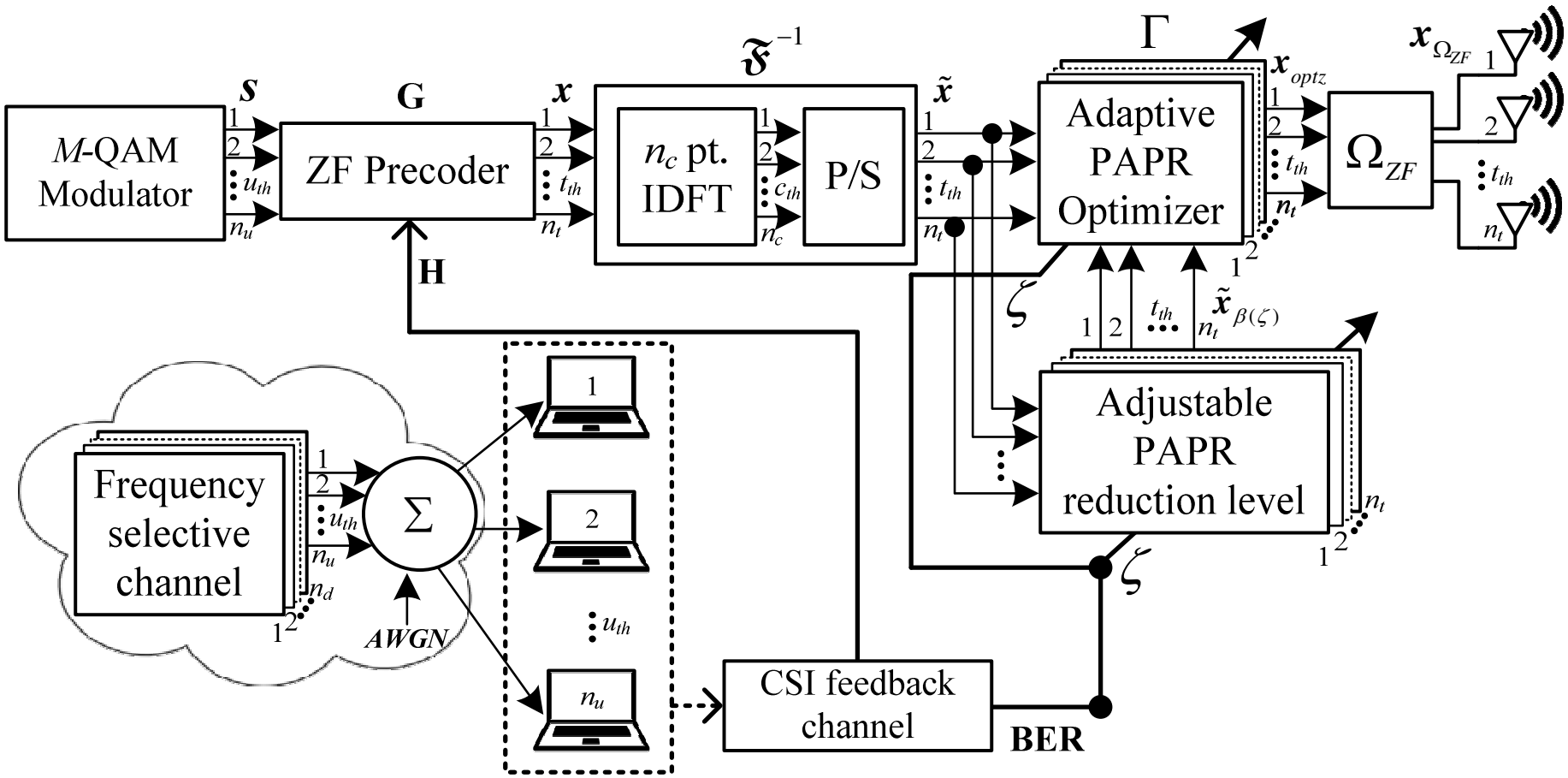


Figure 5.8 The system model of the large-scale MIMO-OFDM system using the proposed technique.

# Chapter 6

# System Performance Analysis

This chapter provides the system analysis of the APO cooperated with the adjustable PAPR clipping level for the large-scale MIMO-OFDM downlink systems. The SER performance is analysed by the clipping noise distribution for both a CP and a PMP scheme. All SER analyses will be used to compare the mathematical analyses and the simulation results of the SER performance in the next chapter.

Section 6.1 introduces the meaning of the clipping noise. The adjustable clipping level of both the CP and the PMP scheme will be analysed in section 6.2 and section 6.3 respectively. Their SER performance analysis will also be expressed in section 6.4. Finally, the summary of this chapter will be shown in section 6.5.

## 6.1 The Clipping Noise of the PAPR Reductions

The clipping noise of the PAPR reductions, $f[k]$, consists of the segments of the $\tilde{x}[k]$ that the high peak values exceed a PAPR target value. It can be represented as

$$f[k] = \tilde{x}[k] - \tilde{x}_{\beta(\zeta)}[k], \tag{6.1}$$

where $|\tilde{x}[k]|$ exceeds $|\beta(\zeta)|$. Then, the $f[k]$ can be shown as a series of pulses as

$$f[k] = \sum_{p=1}^{n_p} f_p[k], \tag{6.2}$$

where $f_p[k]$ is the number of the $p_{th}$ clipping pulse in pulse duration $\tau_p$ with its amplitude maximum at $k_p$, and $n_p$ is the number of clipping pulses [84-92].

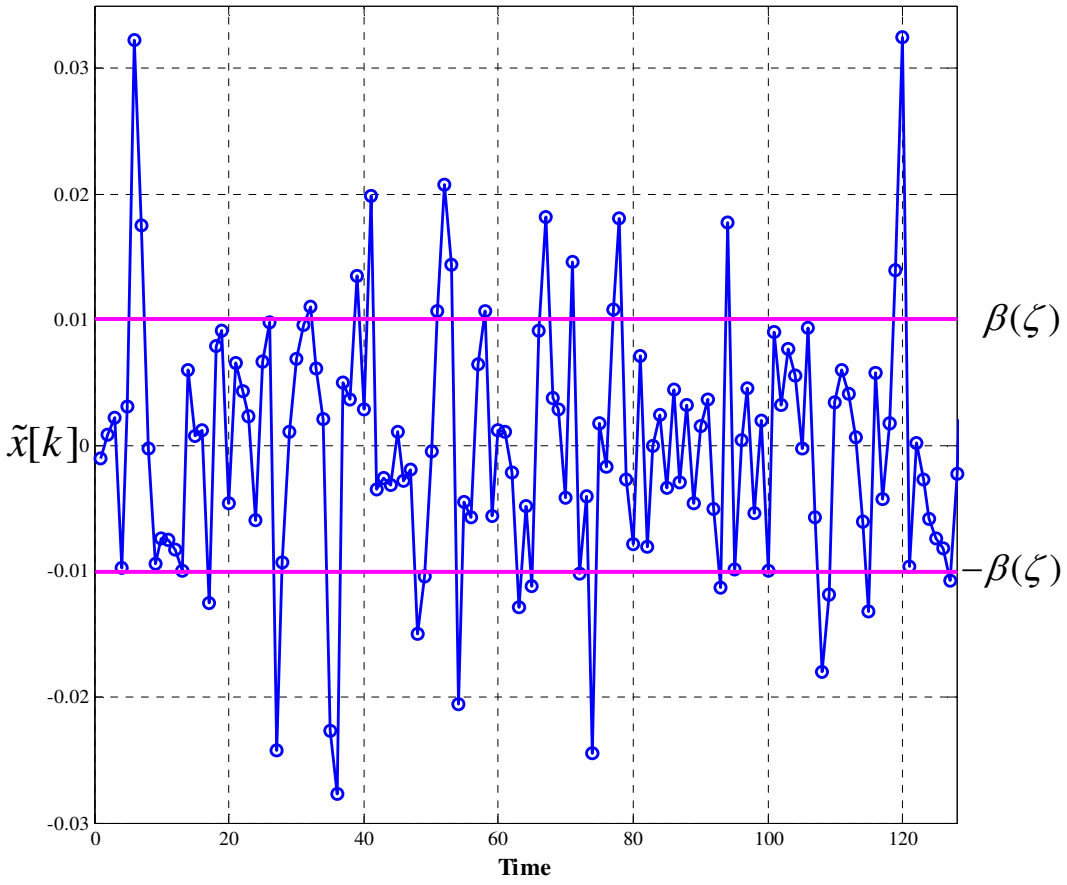


Figure 6.1 Transmitted signal $\tilde{x}[k]$ with a clipped level threshold.

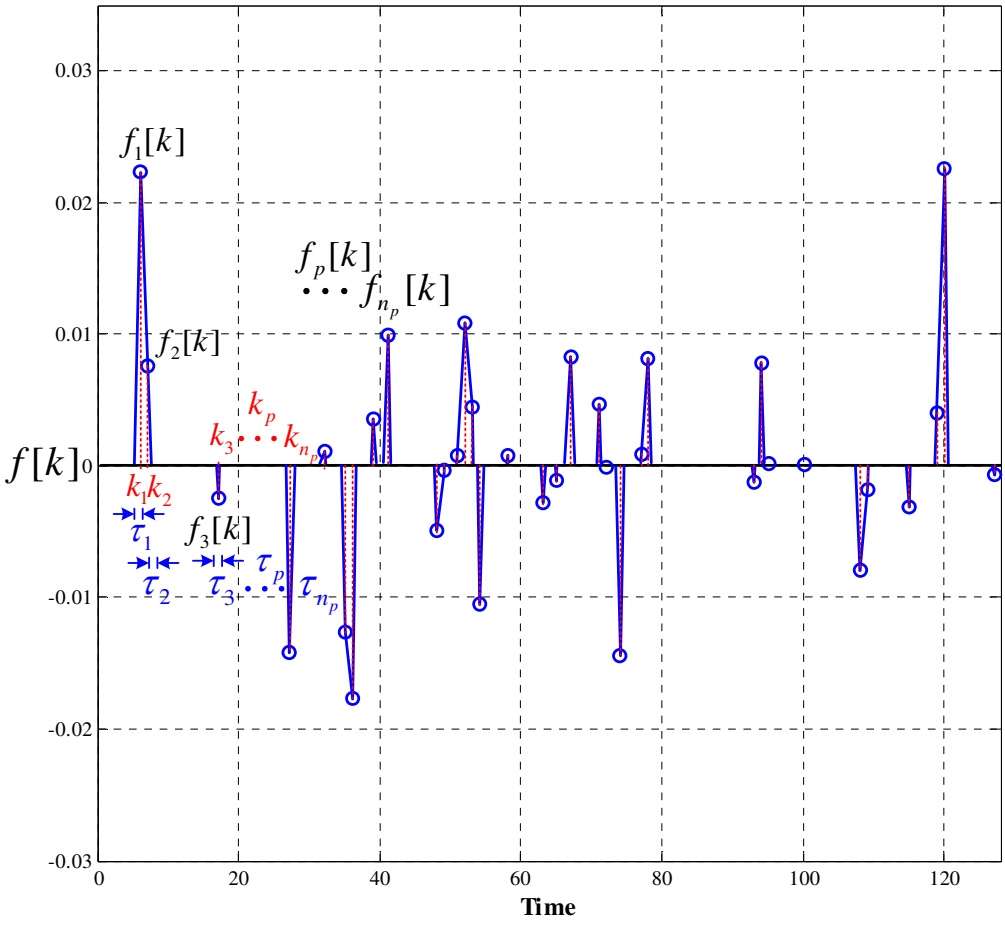


Figure 6.2 The representation of the exceedance values.

## 6.2 The Adjustable Clipping Level Analysis of the CP

The real and imaginary values of input data symbol $X_c$ are assumed to be independent and identically distributed (i.i.d.) and complex Gaussian random variable with variance, $\sigma_{X_c}^2$ . The adjustable clipping threshold, $\beta_{CP}(\zeta)$, and the number of subcarriers, $n_c$, are also assumed to be large, but the time duration of an OFDM block, $T_b$, is assumed to be small, and the OFDM bandwidth $BW = n_c / T_b$ respectively.

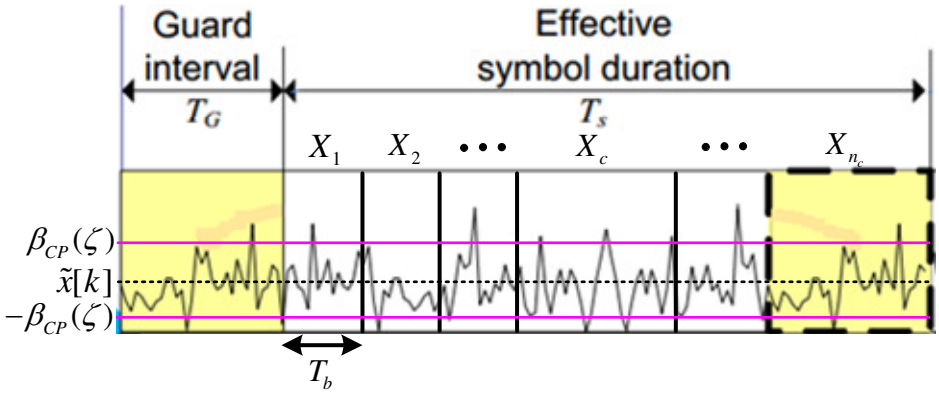


Figure 6.3 An OFDM symbol duration.

In discrete time, $\tilde{x}[k]$ is a real number with the Gaussian random distribution based on the Central Limit Theory. [1]Then, the clipping noise $f_{CP}[k]$ is the consequence of the upward level across the variable level $\beta_{CP}(\zeta)$ of the $\tilde{x}[k]$ and downward level across the level $-\beta_{CP}(\zeta)$ of the $-\tilde{x}[k]$ (or equivalently, of $\tilde{x}^2[k]$ at level $\beta_{CP}^2(\zeta)$ ).

The expected number of crossings of the adjustable threshold level $\left|\beta_{CP}(\zeta)\right|$ per second can be shown as [112-113]

$$\lambda_{\beta_{CP}(\zeta)} = \frac{\beta_{CP}(\zeta)\dot{\sigma}}{\sigma_{X_c}^2\sqrt{2\pi}} e^{\frac{-\beta_{CP}^2(\zeta)}{2\sigma^2}}, \tag{6.3}$$

where $\lambda_{\beta_{CP}(\zeta)}$ is the variable level crossing rate, and [114]

$$\dot{\sigma} = \frac{1}{2\pi}\sum_{\omega=0}^{n_p} \omega^2 S[\omega]\Delta\omega, \tag{6.4}$$

and $S[\omega]$ is the discrete power spectral density (PSD) of $\tilde{x}[k]$, $\omega$ is the frequency spectrum of $k$ by using the discrete Fourier transform, and $\left|\omega\right| \le \frac{\pi n_c}{T_b}$.

While $n_c$ is assumed to be large, the $S(\omega)$ is an approximate constant over a fixed frequency band between $-BW/2$ and $BW/2$. Then, Eq. (6.4) can be written in the form of squares as

[1] The across level of the Gaussian distribution can extensively study in [57, 115-124], the clipped signal in the OFDM spectrum is also provided in [125], and the error rate of the clipped signal in discrete time is given in [126].

$$\dot{\sigma}^2 = \frac{\left(\pi n_c\right)^2 \sigma_{X_c}^2}{3T_b^2} = \frac{\pi^3}{3} BW^2 \sigma_{X_c}^2 . \tag{6.5}$$

Substituting (6.5) into (6.3), the adjustable crossing level rate can be shown as

$$\lambda_{\beta_{CP}(\zeta)} = \sqrt{\frac{\pi}{6}} \cdot \frac{n_c \beta_{CP}(\zeta)}{\sigma_{X_c} T_b} e^{\frac{-\beta_{CP}^2(\zeta)}{2\sigma_{X_c}^2}} . \tag{6.6}$$

Therefore, the average number of the clipping pulses in an OFDM signal duration can be expressed as

$$\overline{n}_p = E\left[n_p\right] = \lambda_{\beta_{CP}(\zeta)} T_b = n_c \sqrt{\frac{\pi}{6}} \cdot \frac{\beta_{CP}(\zeta)}{\sigma_{X_c}} e^{\frac{-\beta_{CP}^2(\zeta)}{2\sigma^2}} . \tag{6.7}$$

The total pulse duration of the clipping signal, $\tau$ , is the random variable with the Rayleigh distribution. It can be written as a probability density function as [112]

$$p(\tau) = \frac{\pi\tau}{2\overline{\tau}^2} e^{\frac{\pi\tau^2}{4\overline{\tau}^2}}, \tag{6.8}$$

where $\tau = \tau_1 + \tau_2 + \cdots + \tau_p + \cdots + \tau_{n_p}$ , and $\overline{\tau}$ is the mean of $\tau$ .

Due to $\lambda_{\beta_{CP}(\zeta)} \overline{\tau} = Pr\left[\tilde{x}[k] > \beta_{CP}(\zeta)\right]$, $\overline{\tau}$ can be presented as

$$\overline{\tau} = \frac{Pr\left[\tilde{x}[k] > \beta_{CP}(\zeta)\right]}{\lambda_{\beta_{CP}(\zeta)}} = \frac{\sigma_{X_c}^2 \sqrt{2\pi}}{\dot{\sigma}\beta_{CP}(\zeta)} = \sqrt{\frac{6}{\pi}} \cdot \frac{\sigma_{X_c}^2}{\beta_{CP}(\zeta) \cdot BW} . \tag{6.9}$$

From (6.8) to (6.9), it can probably imply that $\tau$ is so small in the large-scale MIMO-OFDM systems. By using Taylor's series expansion at $k = k_p$ , $\tilde{x}[k]$ can be expressed as a parabolic function as

$$\begin{aligned} \tilde{x}[k] = \tilde{x}[k_p + \Delta k_p] &\approx \tilde{x}[k_p] + \underbrace{\dot{\tilde{x}}[k_p]\Delta k_p}_{\approx 0} + \frac{1}{2}\ddot{\tilde{x}}[k_p]\Delta k_p^2 \\ &= \tilde{x}[k_p] + \frac{1}{2}\ddot{\tilde{x}}[k_p]\Delta k_p^2 . \end{aligned} \tag{6.10}$$

where $\Delta k_p = k - k_p$, $\dot{\tilde{x}}[k_p] \approx 0$, and $\ddot{\tilde{x}}[k_p] < 0$.

With the approximation in (6.10), $\tilde{x}[k_p + \Delta k_p]$ is assumed to be systematic of $k_p$. Then,

$$\tilde{x}\left[k_p - \frac{\tau_p}{2}\right] \approx \tilde{x}\left[k_p + \frac{\tau_p}{2}\right] \approx \beta_{CP}(\zeta), \tag{6.11}$$

where each clipping pulse $f_p^{CP}[k]$ has a time duration $\tau_p$ when it reaches maximum magnitude at $k_p$, and

$$\tau_p \approx \sqrt{-\frac{8\left(\tilde{x}[k_p] - \beta_{CP}(\zeta)\right)}{\ddot{\tilde{x}}[k_p]}}. \tag{6.12}$$

Finally, each clipping pulse can be approximated as

$$\tilde{x}[k_p + \Delta k_p] - \beta_{CP}(\zeta) \approx \frac{1}{2}\ddot{\tilde{x}}[k_p]\Delta k_p^2 - \frac{1}{8}\ddot{\tilde{x}}[k_p]\tau_p^2, \quad -\frac{\tau_p}{2} \le \Delta k_p < \frac{\tau_p}{2}. \tag{6.13}$$

At the phase $\theta[k] = \theta[k_p + \Delta k_p]$, it narrowly varies within $-\tau_p / 2 \le \Delta k_p < \tau_p / 2$, and all the component frequencies of $\tilde{x}[k]$, which is limited in a band-limited signal, define the phase of $f_p^{CP}[k_p + \Delta k_p]$. Therefore, the phase change of the $c_{th}$ frequency component from $k = k_p$ to $k = k_p + \tau_p / 2$ can be calculated as

$$\Delta\theta[c] = \sum_{c=-\frac{n_c}{2}}^{\frac{n_c}{2}-1} 2\pi c \frac{\tau_p}{2T_b}. \tag{6.14}$$

By substituting (6.9) into (6.14), the phase change can be rewritten as

$$\Delta\theta[c] = \sum_{c=-\frac{n_c}{2}}^{\frac{n_c}{2}-1} \frac{\sqrt{6\pi}c\sigma_{X_c}}{n_c\beta_{CP}(\zeta)}. \tag{6.15}$$

The largest phase change is occurred on $c = -n_c / 2$, and it does not relate to $n_c$. The phase of $f_p^{CP}[k]$ varies from $k = k_p$ to $k = k_p + \tau_p / 2$, which is called upper-bounded, by letting $\theta[c] = \theta\left[\frac{n_c}{2}\right]$ for all $c$. Due to this upper-bounded is so small

while $\beta_{CP}(\zeta)$ is very high, the phase change can be estimated by using Taylor's series expansion at $k = k_p$ as

$$\theta[k_p + \Delta k_p] \approx \theta_p + \gamma_p \Delta k_p, \tag{6.16}$$

where $\theta_p = \theta[k_p],$ and

$$\gamma_p = \frac{imaginary\left[\dot{\tilde{x}}[k_p]\right]}{real\left[\left|\tilde{x}[k_p]\right|\right]}. \tag{6.17}$$

Afterwards,

$$\begin{aligned} f_p^{CP}[k] = f_p^{CP}[k_p + \Delta k_p] &= \left(\tilde{x}[k_p + \Delta k_p] - \beta_{CP}(\zeta)\right) e^{j\theta[k_p + \Delta k_p]} \\ &\approx \left(\frac{1}{2}\ddot{\tilde{x}}[k_p]\Delta k_p^2 - \frac{1}{8}\ddot{\tilde{x}}[k_p]\tau_p^2\right) e^{j\theta[k_p + \Delta k_p]}, \quad -\frac{\tau_p}{2} \le \Delta k_p < \frac{\tau_p}{2}. \end{aligned} \tag{6.18}$$

The absolute value of the phase in terms of $\gamma_p \Delta k_p$ can be skipped because it is probably much too small. According to Appendix B.2, it can prove that

$$E\left[\left|\gamma_p\right|\right] E\left[\tau_p\right] = \frac{\sqrt{2\pi}\sigma_{X_c}}{\beta_{CP}(\zeta)} \operatorname{erfc}\left(\frac{\beta_{CP}(\zeta)}{\sqrt{2}\sigma_{X_c}}\right) e^{\frac{\beta_{CP}^2(\zeta)}{2\sigma_{X_c}^2}}, \tag{6.19}$$

where

$$\begin{aligned} \operatorname{erfc}(x) &= \frac{1}{\sqrt{\pi}} e^{-x^2} \sum_{n=0}^{\infty} \frac{(2x)^{2n+1}}{(2n+1)!} \\ &= \frac{2}{\sqrt{\pi}} e^{-x^2} \left[ x + \frac{2x^3}{1 \cdot 3} + \frac{4x^5}{1 \cdot 3 \cdot 5} + \cdots \right]. \end{aligned}$$

According to Appendix B.4, it proves that $\gamma_p$ and $\tau_p$ are orthogonal. Therefore, in (6.19), the value of $\gamma_p \tau_p$ is so small. A strict justification of $\left|\gamma_p \Delta k_p\right|$ requires the joint CDF of $\gamma_p \tau_p$. Unfortunately, this CDF is difficult to express as a closed form, however, an upper-bounded of the phase change $f_p^{CP}[k]$ can be found.

As the phase change $\left|f_p^{CP}[k]\right|$ is close to zero, the $\left|\Delta k_p\right|$ is gradually converged to $\tau_p / 2$. Then, the time duration is equal to $\tau_p / \sqrt{2}$ and the $\left|f_p^{CP}[k]\right|$ is no less than half of the highest magnitude. By employing the Chebyshev's inequality,

$$Pr\left[\left|\frac{\gamma_p \tau_p}{\sqrt{2}}\right| \geq \delta\right] \leq \frac{\sigma_0^2}{\delta^2}, \tag{6.20}$$

where $\delta > 0$, and the variance of the $\frac{\gamma_p \tau_p}{\sqrt{2}}$ can be symbolised as $\sigma_0^2$. Nevertheless, by using the Cauchy-Schwarz inequality,

$$\sigma_0^2 = E\left[\frac{\gamma_p^2 \tau_p^2}{2}\right] \leq \frac{\sqrt{E\left[\gamma_p^4\right] E\left[\tau_p^4\right]}}{2}. \tag{6.21}$$

By using the results of both Appendix A.1 and Appendix B.2, the right-hand side of the inequality as $\sigma_1^2$. It can be calculated as

$$\sigma_1^2 = \frac{2\sqrt{6}\sigma_{X_c}^3}{\beta_{CP}^3(\zeta)} \sqrt{2 - \left(\sum_{k=0}^{\infty} \frac{e^{-k\left(\frac{\beta_{CP}^2(\zeta)}{2\sigma_{X_c}^2}\right)}}{k} \Delta k\right) \cdot \frac{\beta_{CP}^2(\zeta)}{\sigma_{X_c}^2} e^{\frac{\beta_{CP}^2(\zeta)}{2\sigma_{X_c}^2}}}. \tag{6.22}$$

Then,

$$Pr\left[\left|\frac{\gamma_p \tau_p}{\sqrt{2}}\right| \geq \delta\sigma_1\right] \leq \frac{1}{\delta^2}. \tag{6.23}$$

Finally, the phase term $\gamma_p \tau_p$ can be skipped, and then the clipping pulse of the CP can be approximated as a constant phase parabolic function:

$$f_p^{CP}[k] = f_p^{CP}[k_p + \Delta k_p] \approx \left(\frac{1}{2}\ddot{\tilde{x}}[k_p]\Delta k_p^2 - \frac{1}{8}\ddot{\tilde{x}}[k_p]\tau_p^2\right) e^{j\theta_p}, \quad -\frac{\tau_p}{2} \leq \Delta k_p < \frac{\tau_p}{2}. \tag{6.24}$$

## 6.3 The Adjustable Clipping Level Analysis of the PMP Scheme

The PMP reduction technique employs a FITRA algorithm to decrease the high amount of PAPR amplitude, which is operated in the frequency domain [21]. Therefore, the clipping noise of the PMP analysis is presented in this section in the frequency domain. The frequency spectrum of the clipping noise with the Nyquist-rate sampled discrete-time is presented in [126]. In discrete time, the clipping noise of the adjustable PMP can be shown as

$$f^{PMP}[k] = \tilde{x}[k] - \tilde{x}_{\beta_{PMP}(\zeta)}[k], \tag{6.25}$$

where $\tilde{x}_{\beta_{PMP}(\zeta)}[k]$ is the clipped signal from the adjustable clipping level of the PMP, and its clipping noise can be shown as a series of pulses as

$$f^{PMP}[k] = \sum_{p=1}^{n_p} f_p^{PMP}[k], \tag{6.26}$$

and also shown as the frequency spectrum by using the discrete Fourier transform of (6.26); i.e.,

$$F_p^{PMP}[\omega] = -e^{j[\theta_p - \omega k_p]} \frac{\ddot{\tilde{x}}[k_p]\tau_p}{\omega^2}\left(\operatorname{sinc}\frac{\omega\tau_p}{2} - \cos\frac{\omega\tau_p}{2}\right), \tag{6.27}$$

where $\operatorname{sinc} x = \dfrac{\sin x}{x}$.

$F_p^{PMP}[\omega]$ is distributed over the whole spectral range from $-\infty$ to $\infty$, and it also can be shown in the discrete time as Figure 6.4. This figure shows that the $F_p^{PMP}[\omega]$ contributes the large portion of the out-of-band radiation, and the in-band clipping noise is the small portion of $F_p^{PMP}[\omega]$.

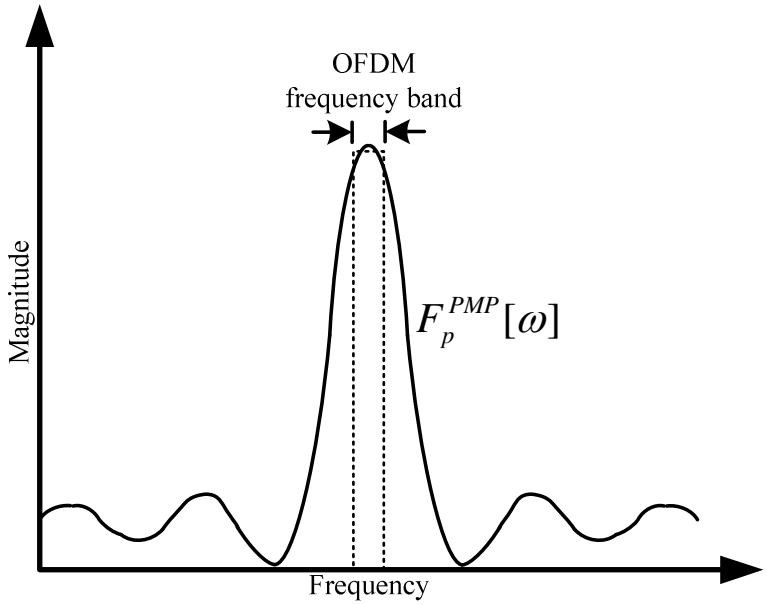


Figure 6.4 Frequency spectrum of $f_p^{PMP}[k]$.

Therefore, the PSD of the $F_p^{PMP}[\omega]$ for multiple pulses can be shown as

$$S_{PMP}[\omega]=\frac{1}{T_b}E\left[\left|F_p^{PMP}[\omega]\right|^2\right]=\frac{1}{T_b}E\left[\sum_{p=1}^{n_p}\left|F_p^{PMP}[\omega]\right|^2\right]+\frac{1}{T_b}E\left[\sum_{p=1}^{n_p}\sum_{\substack{c=1\\c\neq p}}^{n_c}F_p^{PMP}[\omega]F_c^{PMP*}[\omega]\right]. \tag{6.28}$$

In Eq. (6.28), the order of summation and expectation cannot be exchanged because $n_p$ is a random value. Nevertheless, by this definition,

$$\begin{aligned}\frac{1}{T_b}E\left[\sum_{p=1}^{n_p}\left|F_p^{PMP}[\omega]\right|^2\right]&=\frac{1}{T_b}\lim_{n\to\infty}\frac{1}{n}\sum_{l=1}^{n}\sum_{p=1}^{n_{c,l}}\left|F_{p,l}^{PMP}[\omega]\right|^2\\&=\frac{1}{T_b}\lim_{n\to\infty}\frac{\sum_{l=1}^{n}\sum_{p=1}^{n_{c,l}}\left|F_{p,l}^{PMP}[\omega]\right|^2\sum_{l=0}^{n}n_{c,l}}{n\sum_{l=1}^{n}n_{c,l}}\\&=\frac{\overline{n}_p}{T_b}E\left[\left|F_p^{PMP}[\omega]\right|^2\right]=\lambda_{\beta_{PMP}(\zeta)}E\left[\left|F_p^{PMP}[\omega]\right|^2\right],\end{aligned} \tag{6.29}$$

where the $l_{th}$ trial is symbolised as the subscript $l$. As a result,

$$S_{PMP}[\omega] = \lambda_{\beta_{PMP}(\zeta)} E\left[\left|F_p^{PMP}[\omega]\right|^2\right] + \frac{1}{T_b} E\left[\binom{n_p}{2}\right] E\left[F_p^{PMP}[\omega] F_c^{PMP*}[\omega]\right], \quad (6.30)$$

where $p \neq c$, and

$$F_p^{PMP}[\omega] F_c^{PMP*}[\omega] = \sum_{\tilde{k}=-\infty}^{\infty} \sum_{\hat{k}=-\infty}^{\infty} f_p^{PMP}[\tilde{k}] f_c^{PMP*}[\hat{k}] \Delta\hat{k} \Delta\tilde{k}, \quad (6.31)$$

and in the term of $E\left[F_p^{PMP}[\omega] F_c^{PMP*}[\omega]\right]$, it can be determined by

$$\begin{aligned} &E\left[f_p^{PMP}[\tilde{k}] f_c^{PMP*}[\hat{k}]\right] \\ &= E\left[\left(\tilde{x}[k_p + \Delta k_p] - \beta_{PMP}(\zeta)\right) e^{j\theta[k_p + \Delta k_p]} \left(\tilde{x}[k_c + \Delta k_c] - \beta_{PMP}(\zeta)\right) e^{-j\theta[k_c + \Delta k_c]}\right]. \end{aligned} \quad (6.32)$$

However, both $\tilde{x}[k]$ and $\theta[k]$ are independent, and then,

$$\begin{aligned} &E\left[f_p^{PMP}[\tilde{k}] f_c^{PMP*}[\hat{k}]\right] \\ &= E\left[\left(\tilde{x}[k_p + \Delta k_p] - \beta_{PMP}(\zeta)\right)\left(\tilde{x}[k_c + \Delta k_c] - \beta_{PMP}(\zeta)\right)\right] E\left[e^{j\theta[k_p + \Delta k_p]} e^{-j\theta[k_c + \Delta k_c]}\right]. \end{aligned} \quad (6.33)$$

In Appendix B.1, both $\tilde{x}[k_p + \Delta k_p]$ and $\tilde{x}[k_c + \Delta k_c]$ are independent, when $[k_p + \Delta k_p]$ and $[k_c + \Delta k_c]$ are also independent. Then, both $\theta[k_p + \Delta k_p]$ and $\theta[k_c + \Delta k_c]$ are orthogonal. Therefore, $E\left[F_p^{PMP}[\omega] F_c^{PMP*}[\omega]\right] = 0$, and

$$S_{PMP}[\omega] = \lambda_{\beta_{PMP}(\zeta)} E\left[\left|F_p^{PMP}[\omega]\right|^2\right]. \quad (6.34)$$

The out-of-band radiation will be solved by equalising with the APO. Thus, the in-band distortion by adjustable clipping is only focused. In the case of $|\omega| \leq \frac{\pi n_c}{T_b}$, $\frac{\omega \tau_p}{2}$ is approximate to be small, when the level of $\beta_{PMP}(\zeta)$ is high. As the results, the $F_p^{PMP}[\omega]$ can be estimated as

$$F_p^{PMP}[\omega] \approx -e^{j[\theta_p - \omega k_p]} \frac{\dddot{\tilde{x}} \tau_p^3}{12}, \quad (6.35)$$

where $\operatorname{sinc} x - \cos x \approx \frac{x^3}{3}$ [126].

Finally, $S_{PMP}[\omega]$ is an approximated constant over the OFDM band because $F_p^{PMP}[\omega]$ is independent of the frequency $\omega$.

## 6.4 SER Performance Analysis

The closed-form expressions of the SER performance analysis is derived in this section. The ratio of the adjustable clipping level, $\varpi$, of both a CP and a PMP scheme can be shown as

$$\varpi \triangleq \frac{\beta(\zeta)}{\sqrt{2E\left|f[k]\right|^2}} = \frac{\beta(\zeta)}{\sqrt{2}\sigma_{f[k]}}, \tag{6.36}$$

where $\sigma_{f[k]}$ is a variance of the clipping noise either the CP or the PMP scheme.

The stream of the $\tilde{\boldsymbol{x}}$ vector is assumed to distribute as a Rayleigh distribution, it can be shown as the PDF as

$$p(\tilde{\boldsymbol{x}}) = \frac{\tilde{x}}{\sigma_{\tilde{x}}^2} e^{-\frac{\tilde{x}^2}{2\sigma_{\tilde{x}}^2}}. \tag{6.37}$$

The optimised signal, $x_{optz}$, is supposed to be the complex number as

$$x_{optz} = a_{optz} + b_{optz} j, \tag{6.38}$$

with the complex input signal,

$$\tilde{x} = \tilde{a} + \tilde{b}j, \tag{6.39}$$

where

$$\begin{aligned} a_{optz} &= \kappa\tilde{a} + d_r, \\ b_{optz} &= \kappa\tilde{b} + d_i, \end{aligned} \tag{6.40}$$

,[2] $d = d_r + d_i$ is the distortion from the APO cooperated with the adjustable PAPR clipping level, and a constant $\kappa_\zeta$ is given in the term of expectations by

$$\kappa_\zeta = \frac{E\left[a_{optz}\tilde{a}\right]}{E\left[\tilde{a}\tilde{a}\right]} = \frac{E\left[b_{optz}\tilde{b}\right]}{E\left[\tilde{b}\tilde{b}\right]}.$$

The IDFT signal $\tilde{x}$ can be transformed to be the polar coordinate form as

$$\begin{aligned} \tilde{a} &= \tilde{x}\cos\theta, \\ \tilde{b} &= \tilde{x}\sin\theta, \end{aligned} \tag{6.41}$$

where the angle $\theta$ has a uniform distribution on the interval [0, 1].

Therefore, a value of $\kappa_\zeta$ can also be presented in the term of the complementary error function of $\varpi$ as

$$\kappa_\zeta = \frac{E\left[\tilde{x}\cos\theta\tilde{x}_{\beta(\zeta)}\cos\theta\right]}{\sigma_{\tilde{x}}^2} = 1 - e^{-\varpi^2} + \frac{\sqrt{\pi}\varpi}{2}\operatorname{erfc}\left(\varpi\right), \tag{6.42}$$

then, the signal to noise plus distortion ratio (SNDIR) is given by

$$\gamma_0 = \frac{\lambda\dfrac{E_{optz}}{\sigma_{\tilde{x}}^2}}{\left(1-\lambda\right)\dfrac{E_{optz}}{\sigma_{\tilde{x}}^2}+1}, \tag{6.43}$$

where $E_{optz}/\sigma_{\tilde{x}}^2$ is the ratio of the energy of $x_{optz}$ to the noise power spectral density, and $\lambda$ is a signal attenuation factor,

$$\lambda = \frac{\kappa_\zeta^2}{1-e^{-\varpi^2}}.$$

According to [49], an equivalent channel matrix can be demonstrated as $\mathbf{Q} = \mathbf{H}\mathbf{G}_{ZF}$. In MIMO systems, the CSI at the BS can be received by the pilot-based training in the uplink. Therefore, $\left|q_{de}\right|^2 = 0$ if $d \neq e$, where $q_{de}$ is the element of $\mathbf{Q}$ in the $d_{th}$ row and $e_{th}$ column. Then, the SNDIR of each user $u_{th}$ can be shown as

[2] Both $d_r$ and $d_i$ are independent from $\tilde{a}$ and $\tilde{b}$ respectively.

$$\gamma_u = \frac{\frac{\gamma_0}{n_u}\left|q_{ee}\right|^2}{\frac{\gamma_0}{n_u}\sum_{d\neq e}^{n_u}\left|q_{de}\right|^2 + 1} = \frac{\gamma_0}{n_u}\left|q_{ee}\right|^2 = \frac{\gamma_0}{Tr\left(\left(\mathbf{G}_{ZF}\mathbf{G}_{ZF}^H\right)^{-1}\right)} \approx \gamma_0\left(\frac{n_t}{n_u} - 1\right). \quad (6.44)$$

Finally, the probability of SER over frequency-selective fading channels for *M-QAM* signal can be expressed as

$$P_e = \frac{1}{M}\left(M - 1 - \frac{2\psi\left(\sqrt{M}-1\right)}{\sqrt{1+\psi^2}} - \frac{4\psi\left(\sqrt{M}-1\right)^2}{\pi\sqrt{1+\psi^2}}\tan^{-1}\frac{\psi}{\sqrt{1+\psi^2}}\right), \quad (6.45)$$

where

$$\psi = \sqrt{\frac{3\overline{\gamma}_u}{2\left(M-1\right)}},$$

$M = 2^m$ is a symmetrical form of *QAM* when $m$ is even, and $\overline{\gamma}_u$ is the average signal-to-noise-plus-distortion-and-interference ratio per channel. In (6.44), the dimension of the approximated matrix $Tr\left(\left(\mathbf{G}_{ZF}\mathbf{G}_{ZF}^H\right)^{-1}\right)$ is large [127].

In (6.44), it can be seen that if the output of the APO, $x_{optz}$, cooperated with a PMP method, has the same characteristics as the original input signal, $\tilde{x}$, the expectation between them, $E_{PMP}\left[a_{optz} + b_{optz}j, \tilde{a} + \tilde{b}j\right]$, will be closed to one (or non-orthogonal). On the other hand, the expectation between the outputs of the APO worked with the CP, $E_{CP}\left[a_{optz} + b_{optz}j, \tilde{a} + \tilde{b}j\right]$, is close to zero (or orthogonal). In this case, the initial cost function $J_{CP}\left(w[0]\right)$ in the operational area has the distance that is further from $J\left(w^o\right)$ than $J_{PMP}\left(w[0]\right)$. Therefore, a constant $\kappa_\zeta$ in (6.42) from the APO with a PMP scheme is higher than a CP. Finally, from (6.42) to (6.45), they affect to the probability of SER from the APO with a PMP scheme, $P_{e,PMP}$, is lower than the probability of SER from the APO with a CP, $P_{e,CP}$, in every $\gamma_u$ (or $P_{e,PMP} < P_{e,CP}$).

## 6.5 Summary

This chapter provided the system analysis based on the clipping noise, which is used for comparing the SER performances of both the CP and the PMP scheme. As the SER performance analysis, the results show that the adjustable PAPR clipping level with the PMP scheme is superior to the CP undoubtedly, and all theoretical proofs of those will be used for SER performance plotting in the next chapter.

# Chapter 7

## Numerical Results and Discussion

This chapter provides simulation results from our proposed schemes that divided into four cases; first two cases of both clipping (CP) and the PMP cooperated with the proposed least mean square (LMS) algorithms and another two cases of those worked with recursive least squares (RLS) algorithms respectively.

The channel situations are all assumed to switch between the two modes as shown in Figure 7.1; Figure 7.1 (a) shows that the perfect CSI mode is considered while the BS has the availability of the SER feedback from all users in WLAN channel, where all variable values controlled by the SER feedback can be used. On the other hand, Figure 7.1 (b) shows that the imperfect CSI mode is when the channel is corrupted by a worst-case scenario, where all users cannot send the SER feedback to a transmitter perfectly. In this case, the proposed technique is switched to be the fixed-value mode in both an adjustable PAPR reduction level and an APO [30-33].

Both the variable step-size (VS) LMS and the variable forgetting factor (VFF) RLS are used to the perfect CSI mode, and both the FS-LMS and the FFF-RLS are used to the imperfect CSI mode respectively.

The main comparison of all performances is based on the sided-leakage power, the SER performance, the CCDF, and the complexity of the FLOPs. The simulation results are obtained from the communication system over a frequency-selective channel modeled as a tap-delay line with both i.i.d complex Gaussian noise and MUI of the MU large-scale MIMO-OFDM downlink system.

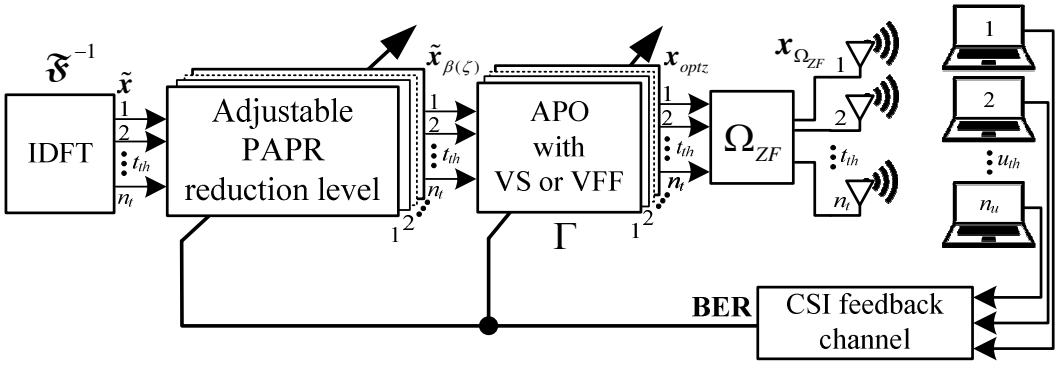


(a) The perfect CSI Mode for either a variable step-size LMS or a variable forgetting factor RLS.

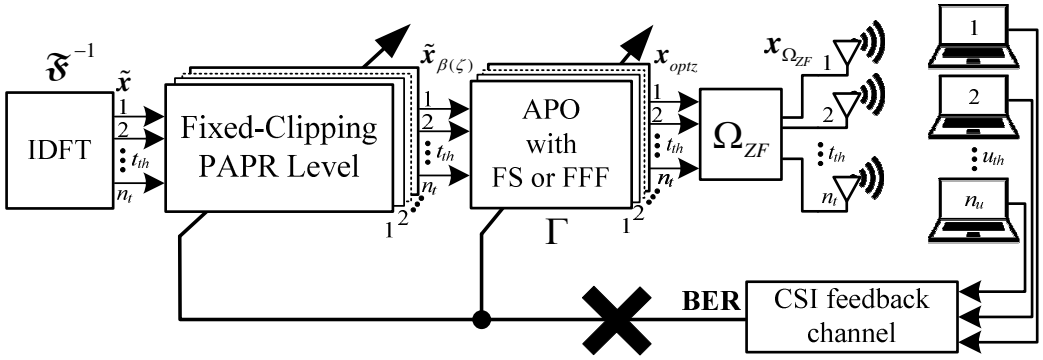


(b) The imperfect CSI Mode for either a FS-LMS or a FFF- RLS.

Figure 7.1 The perfect CSI and the imperfect CSI of the proposed schemes.

The main system parameters are defined as follows: length of transmission information, $n_s$, 216 bits per 1 user/packet and the number of the packets are 1000 packets, the channel taps $n_d = 4$, the single antenna terminals $n_u = 10$, the number of the antennas at BS $n_t = 100$, a number of OFDM subcarriers $n_c = 128$. Also, we utilize 16-*QAM* constellation to map the coded bits at the BS.

For the channel encoder, a convolution encoder is employed with these parameters: channel code rate = 0.5, code generator polynomials = $\left[133_0 \quad 171_0\right]$ applying with puncturing and random interleaving, constraint length = 7, the BCJR decoder is used for channel decoding for each user.

The parameters from the adjustable PAPR clipping level of both the CP and PMP with these follows: the limited upper-range $\beta_{\max}$ is 80% of the $\alpha$ and the limited

lower-range $\beta_{\min}$ is 30% for both $\kappa_\zeta$ and $-\kappa_\zeta$ with the total number of the quantizing step $N_{qt} = 64$. On the other hand, the clipped signal vector $\tilde{\boldsymbol{x}}_\beta$ is the 80% below the threshold of the original vector $\tilde{\boldsymbol{x}}$ for the fixed clipping level. For the PMP, both a number of iterations $Z_{PMP} = 2000$, and a regularization parameter $\lambda_{PMP} = 0.25$. Finally, from the section 5.5, the total number of the signal repetition $N_{rep}$ of each method can be shown in Table 7.1.

Table 7.1 The total number of the signal repetition of each scheme.

| **Methods** | $N_{rep}$ |
|---|---|
| CP-FS-LMS | 4 |
| CP-VS-LMS | 3 |
| PMP-FS-LMS | 2 |
| PMP-VS-LMS | 1 |
| CP-FFF-RLS | 0.5 |
| CP-VFF-RLS | 0.25 |
| PMP-FFF-RLS | 0.5 |
| PMP-VFF-RLS | 0.25 |

All parameters of the APO can be shown in this section. The mean squared error threshold $J(\boldsymbol{w}^o)$ is 0.00000625, an optimizer length $L = 5$, an initial of the weight coefficient $w_l[0] = 0$. For the LMS algorithm, a FS $\mu = 0.9$, an initial variable step-size $\mu[0] = 0$, $\varphi[0] = 1$, $e[0] = 1$, $\zeta[0] = 1$, $\delta = 0.999$, $\rho = 0.001$, $\xi = 0.999$, and $\upsilon = 0.00001$. For the RLS algorithm, an initial variable forgetting factor $\chi[0] = 1$, $e[0] = 1$, $\varphi[0] = 1$, $\zeta[0] = 1$, $\delta = 0.004$, $\xi = 0.999$, $\vartheta = 0.00001$, $\varpi = 0.001$, and $\rho = 0.9996$.

# 7.1 Out-of-Band Distortion of Each Scheme

The first comparison of each scheme can be illustrated by the power spectral density (PSD). It is the frequency response of a transmitted signal $x_{optz}$, where the clipped signal is sent through a power amplifier. This thesis employs the solid-state power amplifier (SSPA) for studying the out-of-band distortion of the proposed techniques [16]. The reason is that it provides higher performance and reliability than other types of RF-amplifiers. Moreover, the flexibility of its design provides the ability to extend to adjacent frequency bands requiring only a short development time at very low risk [128]. The output of SSPA can be presented as

$$x_{\Omega}[k] = \frac{\left|x_{optz}[k]\right|}{\left(1+\left(\frac{\left|x_{optz}[k]\right|}{C}\right)^{2a}\right)^{\frac{1}{2a}}} e^{j\theta[k]}, \tag{7.1}$$

where $x_{optz}$ is the input, and $x_{\Omega}$ is the output of the SSPA. Both $C$ and $a$ are set to equal 6dB and 3 respectively.

Figure 7.2 shows the PSDs results of each scheme. The PMP-RLS leads to only minus 21dB out-of-band radiation. It is 1.5dB lower than the PMP-LMS, and 4dB lower than the original PMP scheme [21]. On the other hand, the CP-RLS leads to minus 18dB out-of-band radiation. It is 2.5dB lower than the CP-LMS, and 4dB lower than the conventional clipping technique [28].

The results clearly show that the proposed techniques can reduce the sided-leakage power approximately 4dB for the RLS algorithm, and 2dB for the LMS algorithm compared with the conventional PAPR reduction schemes respectively.

In the further sections, the comparisons of each scheme, which are the CP-LMS, the CP-RLS, the PMP-LMS, and the PMP-RLS, are described in the term of the SER performance, the CCDF of PAPR performance, and their complexity. Finally, the summary section of this chapter will be presented at the end of the chapter.

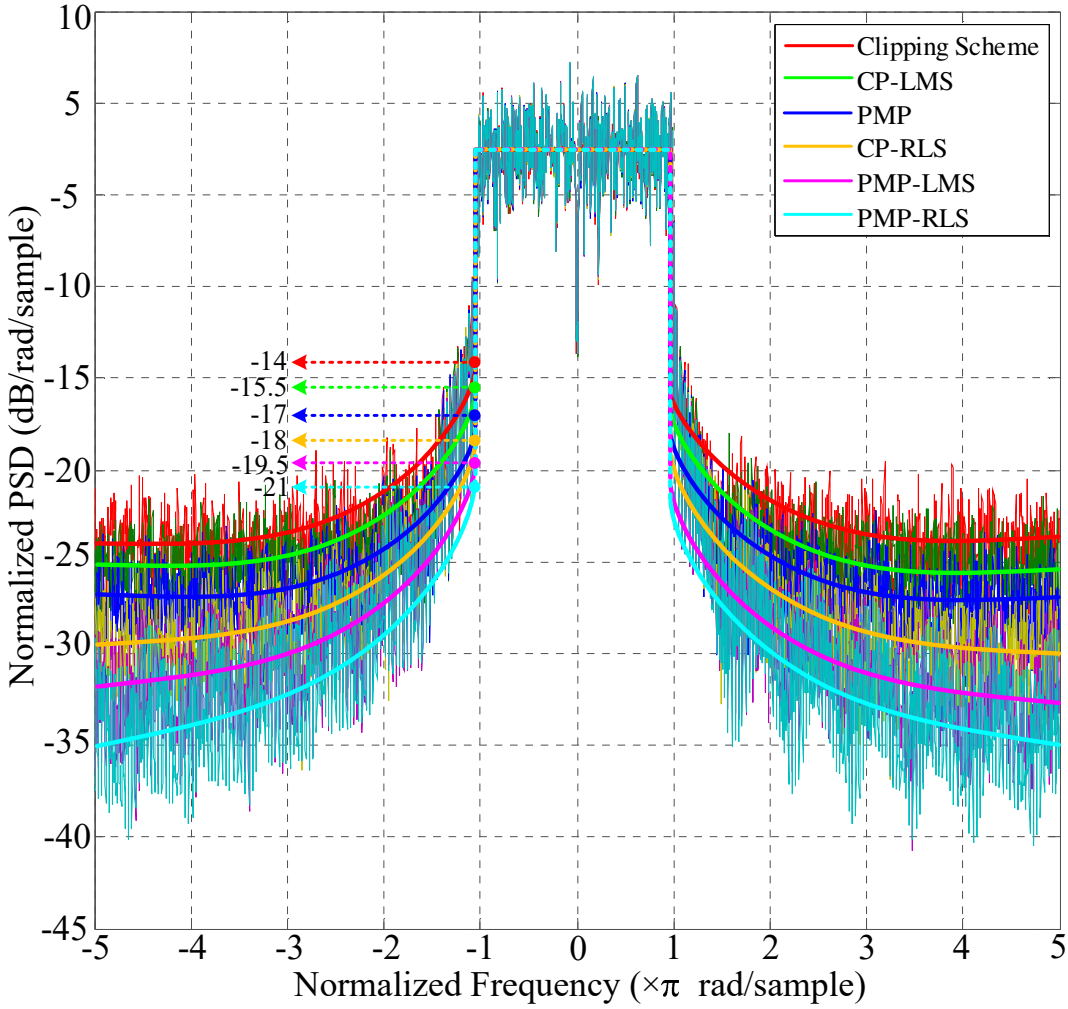


Figure 7.2 PSDs of signals transformed by conventional and proposed schemes for WLAN with 16-QAM.

## 7.2 The CP with the LMS Algorithm (The CP-LMS)

This section is the CP scheme cooperated with the proposed LMS algorithm, which is used with Eq. (5.8) and Eq. (5.9). The performance comparison of whether a FS and a variable step-size are shown in the case of both the SER performance and the CCDF comparisons.

Figure 7.3 shows the SER performance of both simulation results and the analytical results of each scheme, which are the [1]FCL-CP-FS-LMS and the ACL-CP-

[1] The acronym FCL stands for the fixed-clipping level used in the imperfect CSI, and the acronym ACL stands for the adjustable-clipping level used in the perfect CSI respectively.

VS-LMS respectively. It obviously shows that the ACL-CP-VS-LMS is superior to the FCL-CP-FS-LMS.

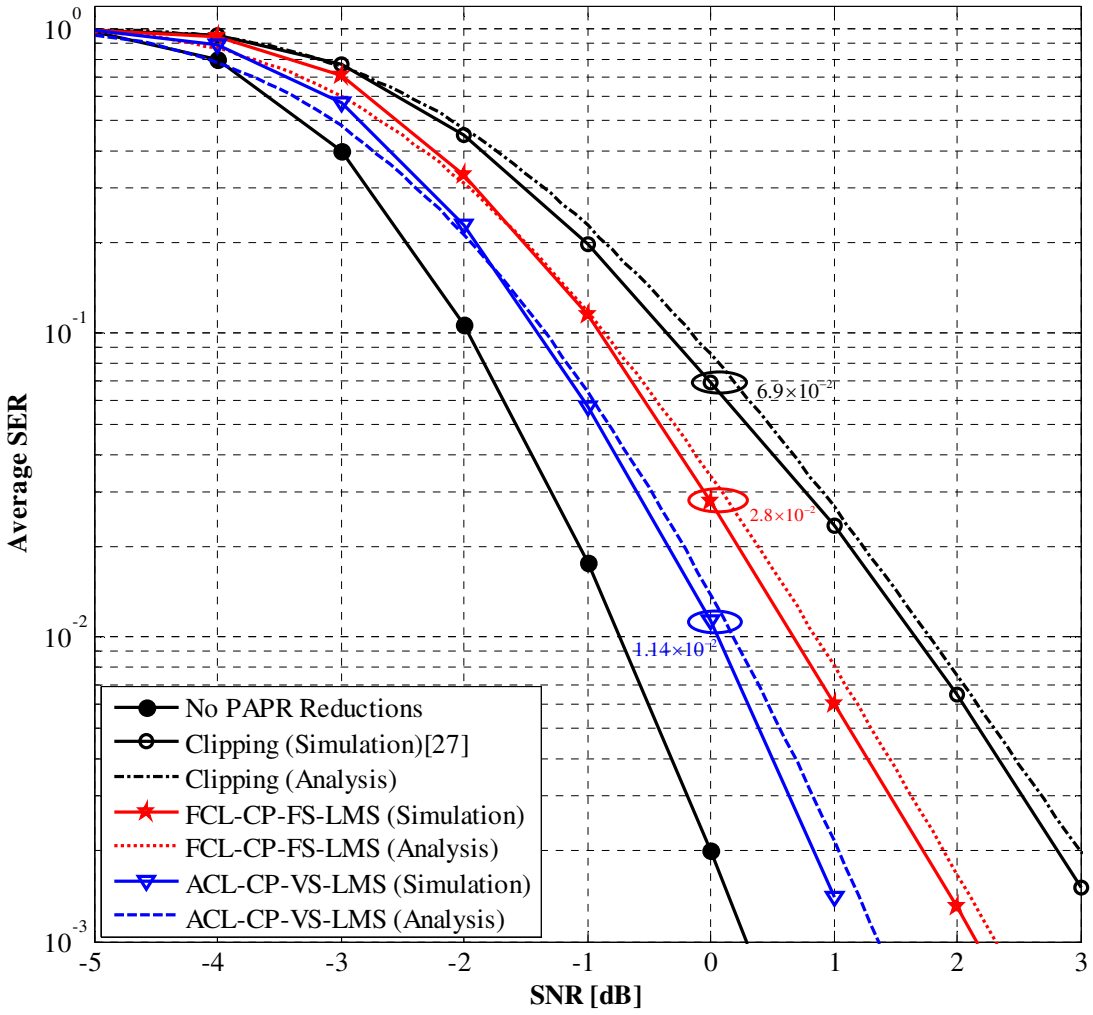


Figure 7.3 The SER performance of the CP-LMS under the perfect and imperfect CSI.

The gap of the SER performance between the FCL-CP-FS-LMS and the ACL-CP-VS-LMS is around $1.66\times10^{-2}$ at $E_b/N_0$ = 0dB. It means that the adjustable PAPR clipping level assists the APO effectively by using the SER feedback from all users. However, the proposed techniques provide a lower SER performance than the conventional CP. They can reduce the symbol error rate at $E_b/N_0$ = 0dB up to $1.14\times10^{-2}$ for the ACL-CP-VS-LMS and $2.8\times10^{-2}$ for the FCL-CP-FS-LMS, while the ordinary CP is about $6.9\times10^{-2}$. Although the SER performance of the CP-LMS is not comparable with the lowest SER performance of the transmitted signals without PAPR reductions, it is the trade-off between the SER performance and the large amounts of PAPR.

Figure 7.4 shows the CCDF of PAPR with each method. As mention in Chapter 1, the main task of the APO does not seem to reduce the amount of PAPR. Anyway, there is a slight reduction the amount of the PAPR around 0.2dB compared with the conventional CP and 6.8dB without any PAPR reductions.

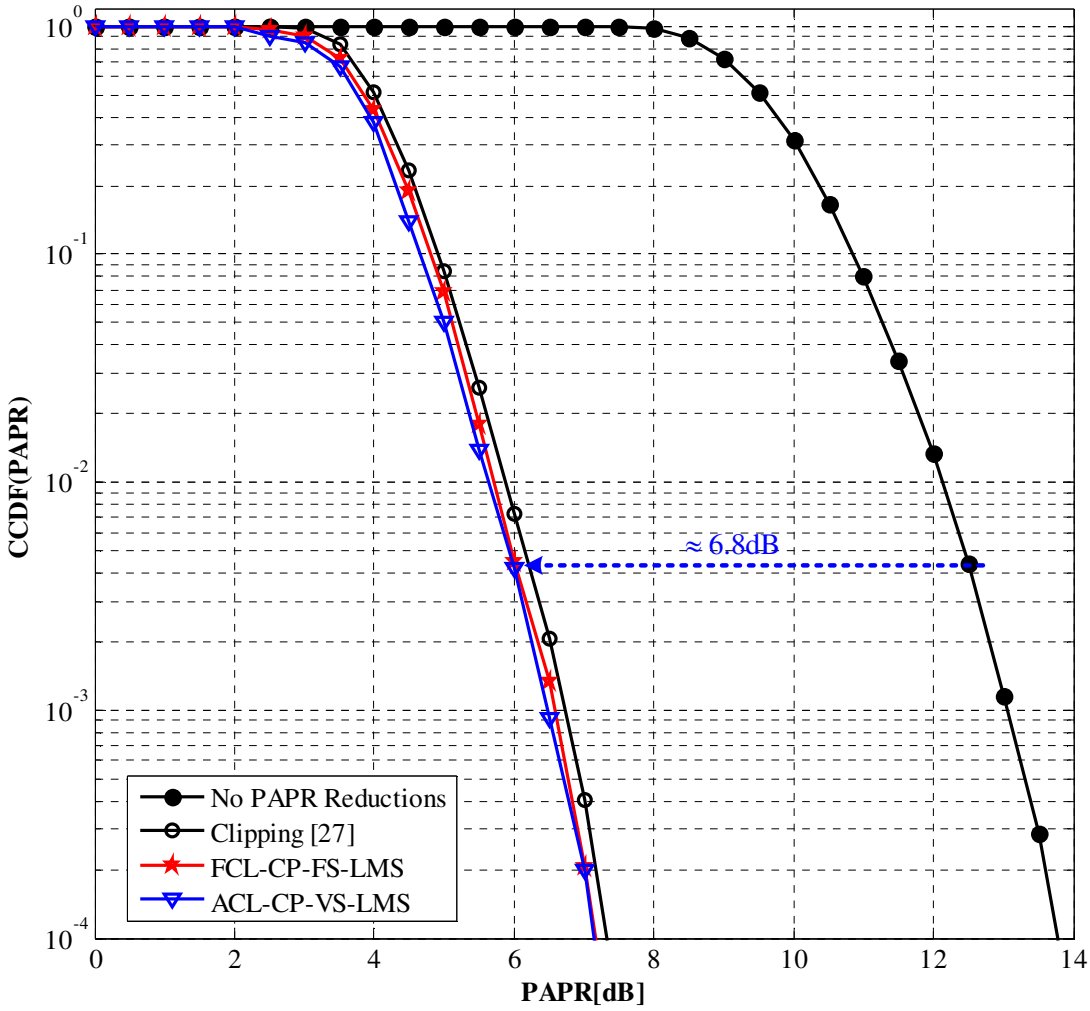


Figure 7.4 The CCDF (PAPR) performances of the CP-LMS.

The measurement of its complexity can be shown in the term of FLOPs counting [129]. Therefore, [2]the complexity of the CP-LMS can be shown in the FLOPs counting as

$$(2n_t - 1)(n_c n_s n_t n_u)(2n_c n_s n_t n_u - 1)(LN_{rep} n_c n_s n_u)^2,$$

and

[2] The more details of the FLOPs counting can be calculated and shown in Appendix C.

$$(2n_t - 1)(2n_c n_s n_t n_u - 1)(LN_{rep})^2 (n_c n_s)^2 (n_t n_u n_c n_s)^4,$$

for the FCL-CP-FS-LMS and the ACL-CP-VS-LMS respectively.

To conclude, this section provides the first case of the proposed scheme, which is the CP-LMS. This technique overwhelmingly improves the SER performance better than using normal clipping technique for every $E_b/N_0$ values. However, it may not be impressive in the term of its CCDF performance. In the next section, there is the next step of the proposed scheme, which is the modified RLS algorithm for the adjustable PAPR reduction level.

## 7.3 The CP with the RLS Algorithm (The CP-RLS)

The CP-RLS scheme is the second technique for consideration. There is a replacement for the section 7.2 with the proposed RLS algorithm. Both the FFF-RLS and the VFF-RLS are used for comparing all performances with the normal CP.

All equations from Eq. (5.11) to Eq. (5.15) are used in this experiment in the term of both a SER performance and a CCDF performance. Figure 7.5 shows the SER performance of the CP-RLS with or without the SER feedback from terminals in the WLAN cell. The gap of their SER performance is closer together than the CP-LMS shown in section 7.2. The gap of the SER performance between the FCL-CP-FFF-RLS and the ACL-CP-VFF-RLS is around $6.6\times10^{-3}$ at $E_b/N_0$ = 0dB. It means that the RLS algorithm can reduce the error rate in the case of without SER feedback and it also improves the overall SER performance better than the LMS algorithm from the previous section. The reduction of the symbol error rate at $E_b/N_0$ = 0dB is about $7.2\times10^{-3}$ and $1.38\times10^{-2}$ for the ACL-CP-VFF-RLS and the FCL-CP-FFF-RLS respectively.

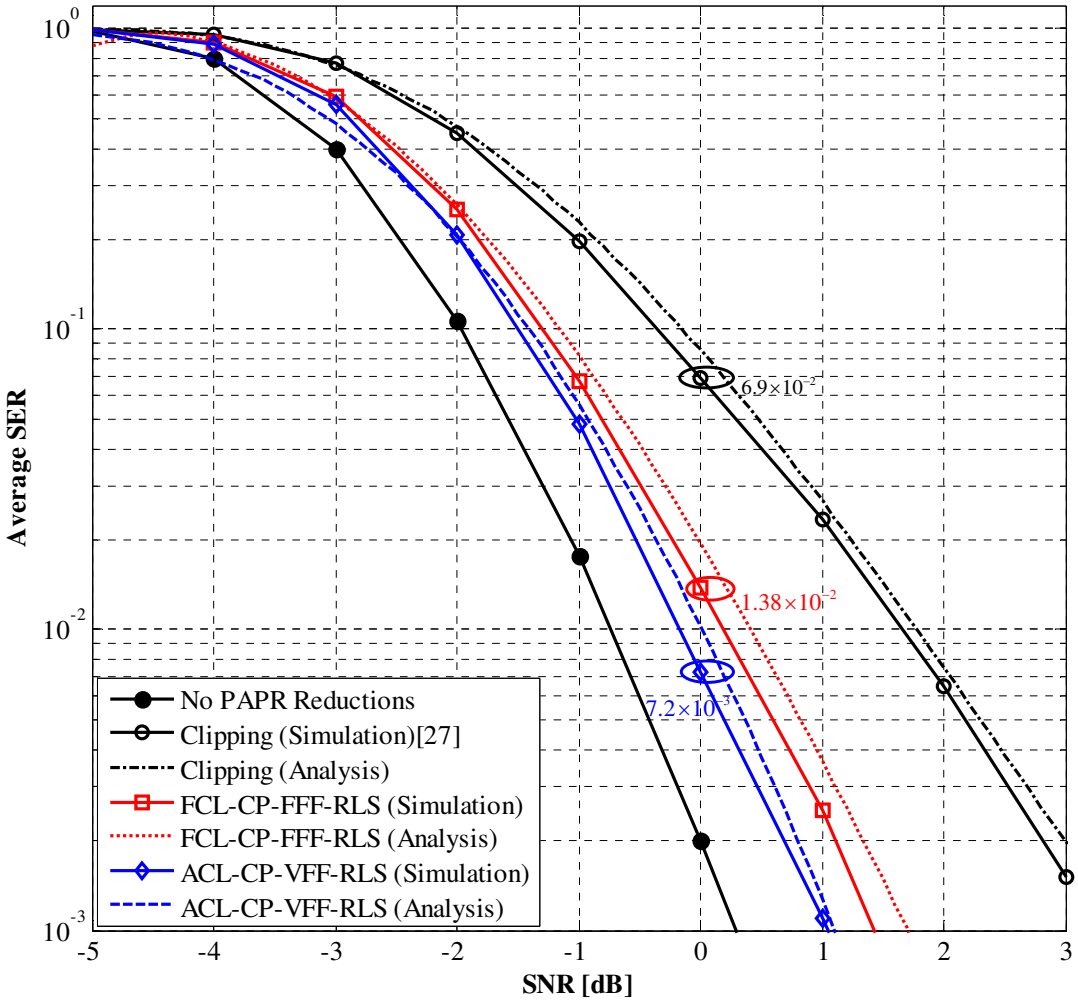


Figure 7.5 The SER performance of the CP-RLS under the perfect and imperfect CSI.

Their CCDF of PAPR can be shown in Figure 7.6. The results show that the performance of the CP-RLS is nearly the same as the CP-LMS, which is about 6.8dB compared with no PAPR reductions, and about 0.2dB compared with the conventional CP. Note that the CCDF performance of both the FCL-CP-FFF-RLS and the ACL-CP-VFF-RLS are also almost the same. It means that the proposed RLS algorithm effectively works in the same performance either with or without the SER feedback. This scheme is a good choose for the large-scale MIMO-OFDM systems, where the channel noise level is large resulting received signal at the transmitter.

In the term of the complexity, the FLOPs counting of the CP-RLS can be shown as

$$(2n_t - 1)(3n_c n_s n_t n_u - 1)(n_c n_s n_t n_u)^2 (LN_{rep} n_c n_s)^2,$$

and

$$(2n_t - 1)(LN_{rep}n_c n_s)^2(3n_c n_s n_t n_u - 1 + n_c n_s n_t n_u(2n_c n_s n_t n_u - 1))(n_c n_s n_t n_u)^3,$$

for the FCL-CP-FFF-RLS and the ACL-CP-VFF-RLS respectively.

It shows that the complexity of the CP-RLS is more than the CP-LMS causing the higher rates of the time and energy consumption in the large-scale MIMO-OFDM systems.

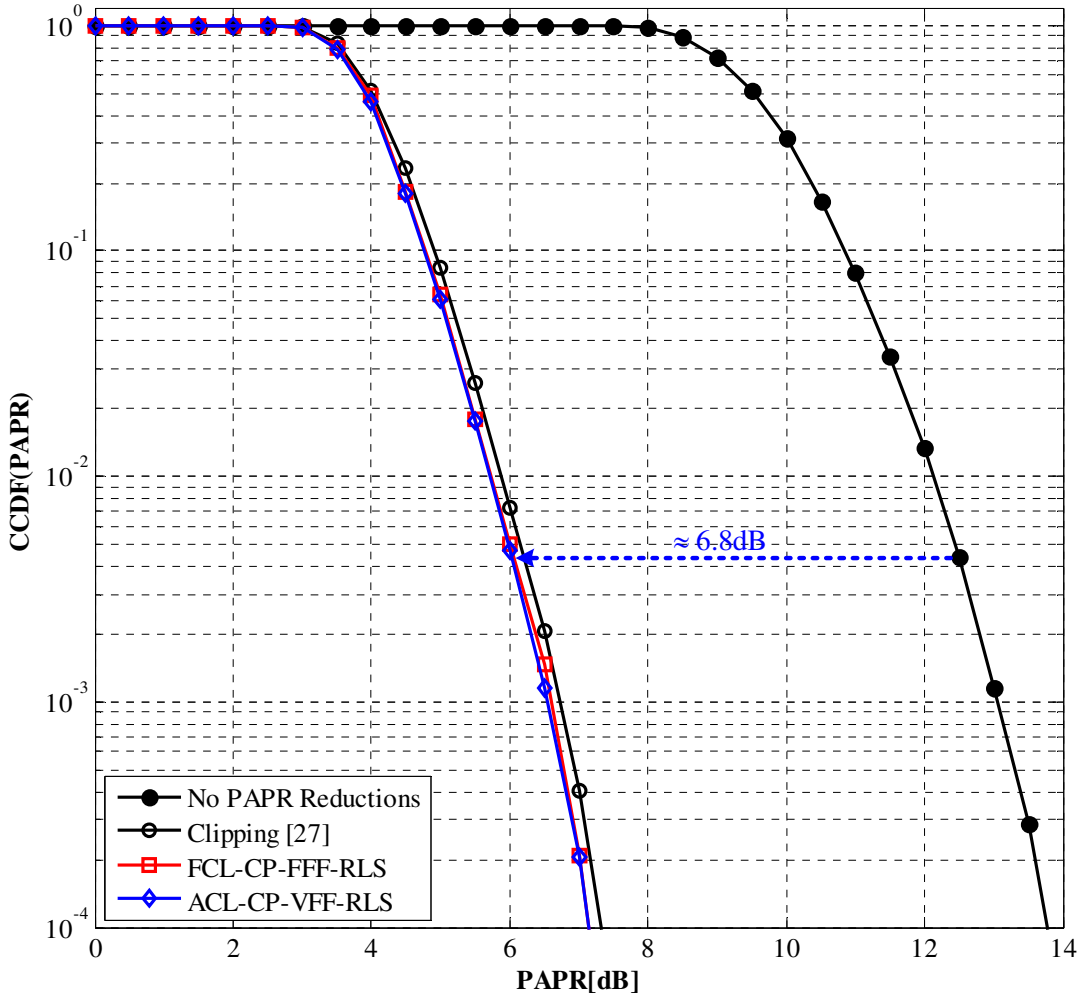


Figure 7.6 The CCDF (PAPR) performances of the CP-RLS.

## 7.4 The PMP Scheme with the LMS Algorithm (The PMP-LMS)

The PMP-LMS scheme is the third scheme for consideration in this section. Likewise, section 7.2 and section 7.3, both the LMS and the RLS algorithms are still compared, but the adjustable PAPR clipping process is changed from the clipping technique to be the PMP technique. In this section, both the fixed-clipping level and the variable clipping level of the PMP with the proposed LMS algorithm are presented.

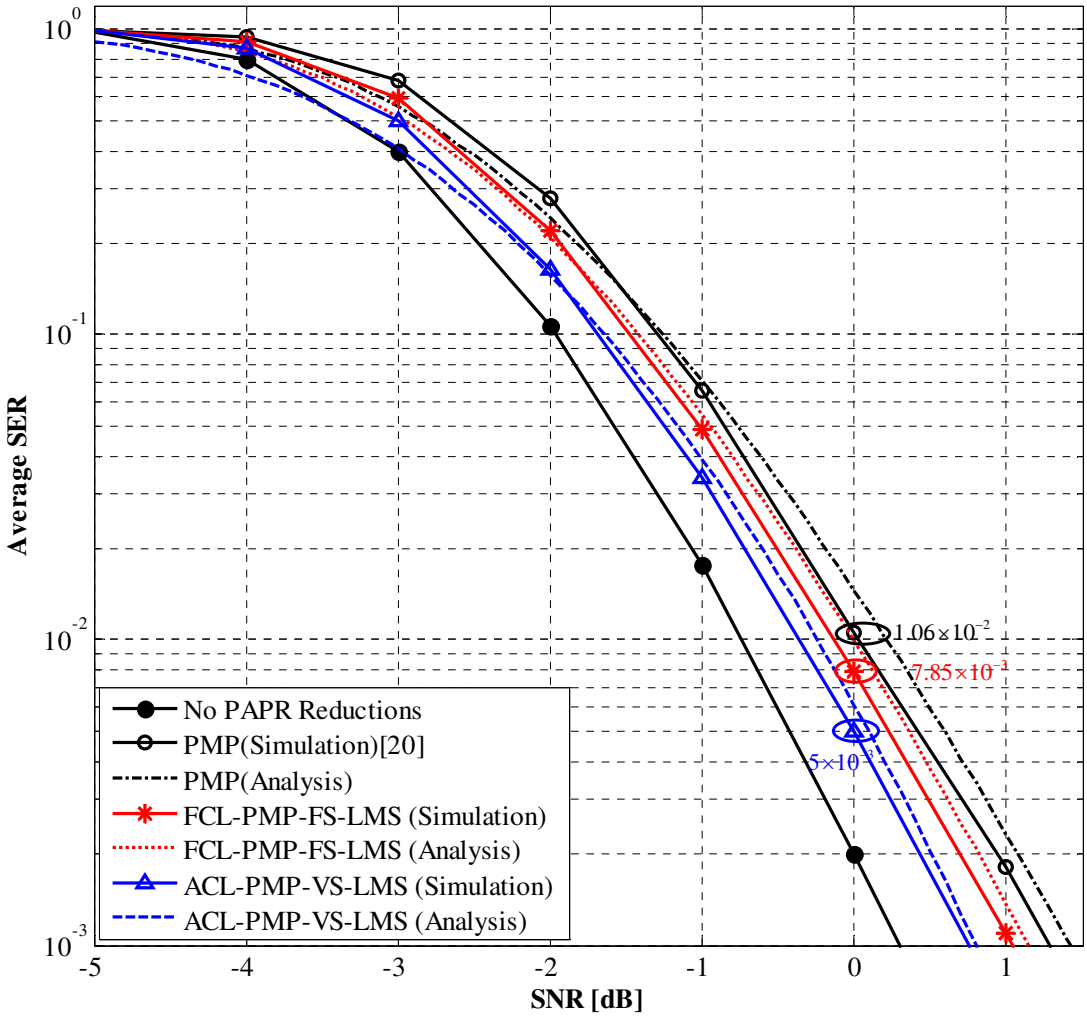


Figure 7.7 The SER performance of the PMP-LMS under the perfect and imperfect CSI.

Figure 7.7 shows the SER performance of the PMP-LMS under the perfect and imperfect CSI. The simulation results show that the proposed techniques, which are the FCL-PMP-FS-LMS and the ACL-PMP-VS-LMS, can assist the conventional

PMP to reduce the error rate effectively. The reductions of the symbol error rate at $E_b/N_0$ = 0dB are $5\times10^{-3}$ and $7.85\times10^{-3}$ for the perfect CSI and the imperfect CSI respectively, while the original PMP is about $1.06\times10^{-2}$ [21].

In Figure 7.8, even though the PMP is the high performant tool for the PAPR reduction, the proposed PMP-LMS scheme still slightly decreases the amount of PAPR about 0.1 dB compared with the conventional PMP technique [21]. In fact, it may not be compared with the CP-LMS scheme in term of the gap between the original CP and the proposed technique. The gap of the CCDF of PAPR reduction between the CP-LMS and the CP is about 0.2dB, but the PMP-LMS and the original PMP is around 0.1dB. In practice, the PAPR reduction performance is not much different, but it is distinctly different in the term of the symbol error rate.

The gap of the SER performance between the original CP and the CP-LMS technique at $E_b/N_0$ = 0dB is about $5.76\times10^{-2}$ ($6.9\times10^{-2}$–$1.14\times10^{-2}$=$5.76\times10^{-2}$), while the conventional PMP scheme and the PMP-LMS are $5.6\times10^{-1}$ ($1.06\times10^{-2}$–$5\times10^{-3}$=$5.76\times10^{-2}$). It means that the proposed schemes assist the SER performance of the CP more effective than the PMP scheme. The reason is the PMP scheme has a FITRA algorithm to help itself to smoothly clip output signal $\tilde{x}_{\beta_{PMP}}$, but the output signal of the CP $\tilde{x}_{\beta_{CP}}$ is the cutting shape without any equalization. This is the reason why the proposed scheme can assist to customise the output signal $\tilde{x}_{optz}$ of the CP better than the PMP scheme.

The complexity of the PMP-LMS can be shown in the term of the FLOPs counting as

$$(2n_c n_s n_t n_u - 1)(Z_{PMP} n_t n_u)(2n_t - 1)(n_t(2n_u - 1)(2n_t - 1) + n_c n_s)(LN_{rep} n_c n_s n_u)^2,$$

and

$$\left(n_t\left(2n_u - 1\right)\left(2n_t - 1\right) + n_c n_s\right)\left(2n_c n_s n_t n_u - 1\right)\left(Z_{PMP} n_t^2 n_u^2 n_c n_s\right)\left(2n_t - 1\right)\left(LN_{rep} n_c n_s n_u\right)^2,$$

for the FCL-PMP-FS-LMS and the ACL-PMP-VS-LMS respectively.

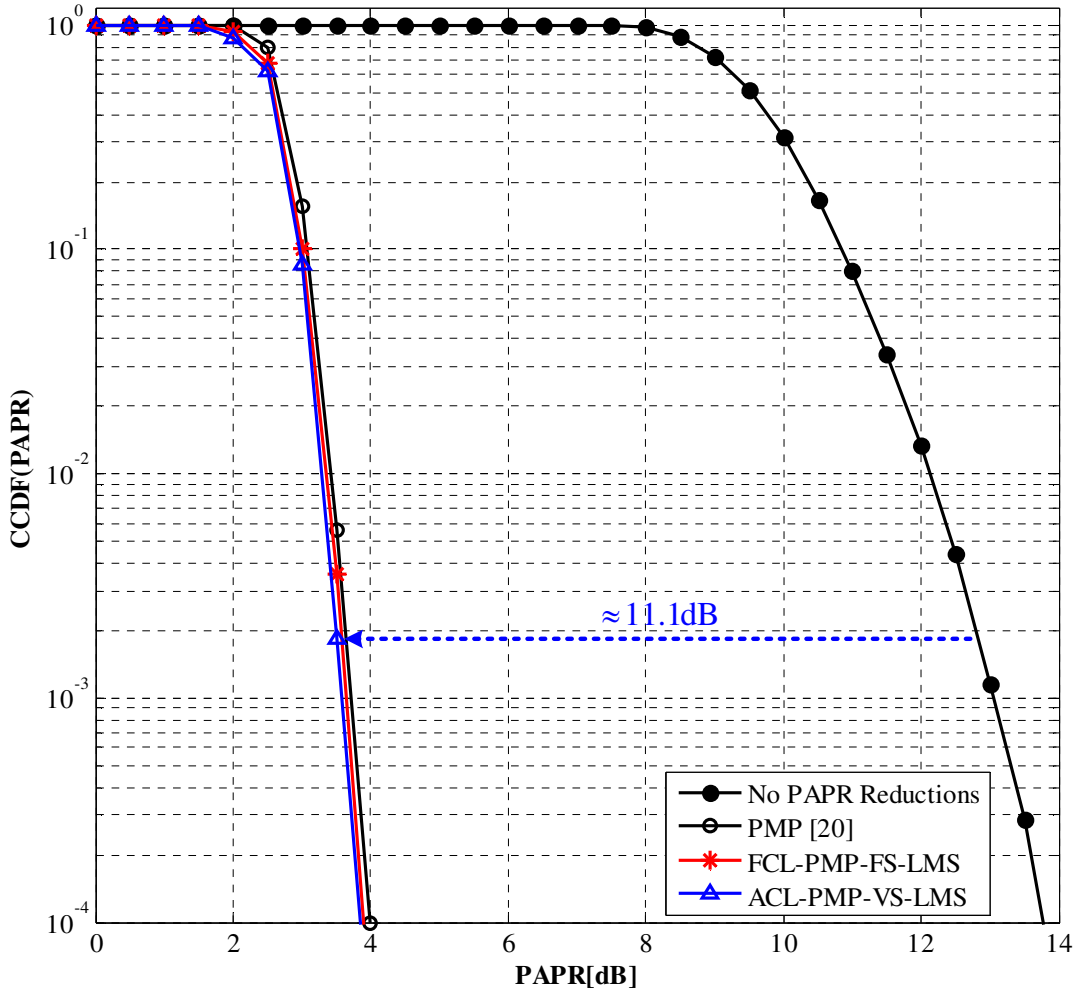


Figure 7.8 The CCDF (PAPR) performances of the PMP-LMS.

## 7.5 The PMP Scheme with the RLS Algorithm (The PMP-RLS)

The PMP-RLS scheme is the last scheme to consider in this section. In the term of the SER performance, this scheme seems like the best of the four cases that have presented in this chapter before.

As shown in Figure 7.9, the SER performance of the PMP-RLS under the perfect CSI at $E_b/N_0$ = 0dB is around $3.7\times10^{-3}$, and the imperfect CSI is about $6.3\times10^{-3}$ respectively. This is the closest gap of the SER that is nearly the performance in the case of no PAPR reductions. The gap of the SER performance between the ACL-PMP-VFF-RLS scheme and original transmitted signal $\tilde{x}$ without any clipping

processes at $E_b/N_0$ = 0dB is around $1.7\times10^{-3}$ ($3.7\times10^{-3}$–$2\times10^{-3}$=$1.7\times10^{-3}$). On the other hand, a disadvantage, its complexity need to be improved and can be represented as the FLOPs counting as

$$(2n_t-1)(LN_{rep}n_cn_s)^2(3n_cn_sn_tn_u-1)(Z_{PMP}n_t)(n_tn_u(2n_u-1)(2n_t-1)+n_cn_s),$$

and

$$\begin{aligned}&(2n_t-1)(LKn_cn_s)^2\left(3n_cn_sn_tn_u-1+n_cn_sn_tn_u\left(2n_cn_sn_tn_u-1\right)\right)\\&\qquad\cdot(Zn_t)\left(n_tn_u\left(2n_u-1\right)\left(2n_t-1\right)+n_cn_s\right)\left(n_cn_sn_tn_u\right),\end{aligned}$$

for the FCL-PMP-FFF-RLS and the ACL-PMP-VFF-RLS respectively.

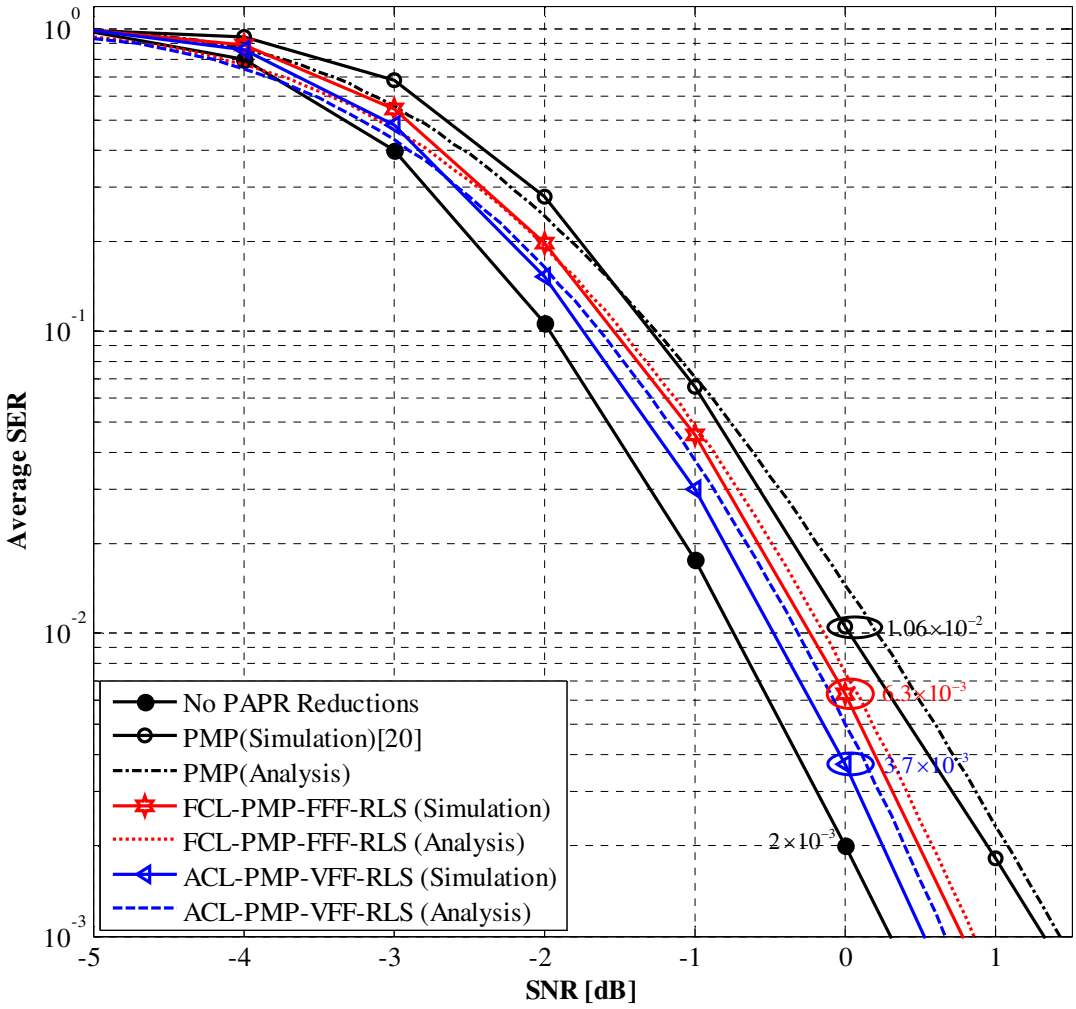


Figure 7.9 The SER performance of the PMP-RLS under the perfect and imperfect CSI.

Figure 7.10 shows the PAPR performances in the term of the CCDF of the PMP-RLS both with and without the SER feedback. Their performance is nearly the same,

and it means that the PMP-RLS can equalise the transmitted signal $\tilde{x}_{optz}$ effectively even though any amount of noise in the channel is harmful effects to the information in the SER feedback.

For the overall CCDF performance of the PMP-RLS, it seems like the same as the PMP-LMS performance in the previous section. The gap of the CCDF of PAPR reduction between the PMP-RLS and the conventional PMP is about 0.1dB, and no PAPR reductions are approximately 11.1dB.

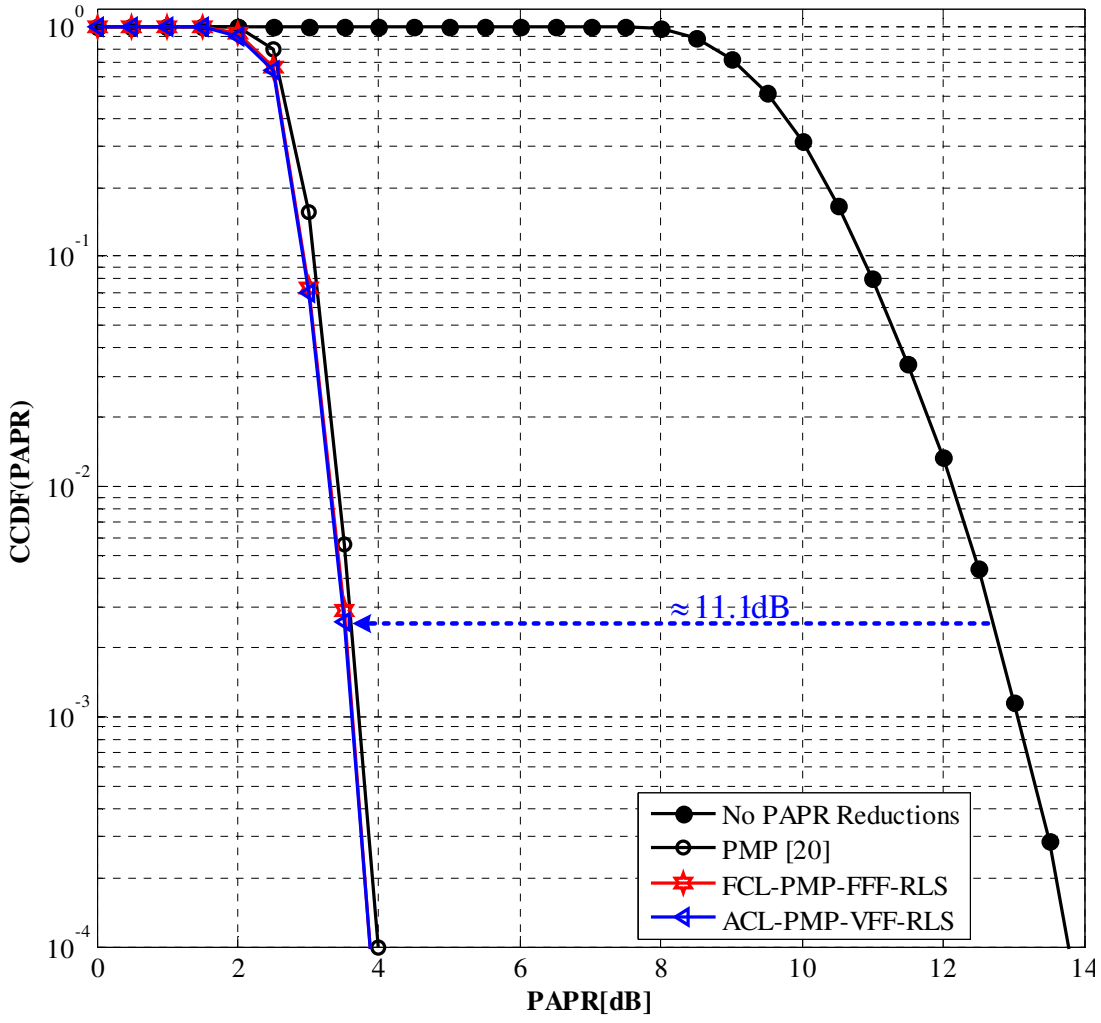


Figure 7.10 The CCDF (PAPR) performances of the PMP-RLS.

## 7.6 Summary

This chapter provides the performance comparisons of each proposed scheme, which are the CP-LMS, the CP-RLS, the PMP-LMS, and the PMP-RLS. The first comparison is the out-of-band distortion based on the power spectral density causing the error rate at the terminals in the WLAN cell. This result shows that the proposed RLS algorithm can lower the out-of-band power leakage by 4dB in both the conventional CP and the PMP scheme.

The comparisons of the proposed techniques with the SER, the CCDF, and complexity performances are represented from the section 7.2 to the section 7.5 respectively. It is found that the analysis for the SER performances in Figures 7.3, 7.5, 7.7, and 7.9 are lower than the simulation at low SNR, but are higher than the simulation at medium and high SNR. The deviation between the analysis and the simulation is no more than $\pm 4\times 10^{-4}\text{dB}$, which is acceptable for all experiments, being inline with current practice.

Figure 7.11 shows the overall SER performance of every proposed method. The results clearly show that the use of the SER feedback to control all coefficients of the proposed techniques can almost reduce the symbol error rate better than the conventional PAPR reductions for every $E_b/N_0$ values.

For the PAPR reduction performance comparison in the term of the CCDF of each scheme, it can be shown as a summary figure in Figure 7.12. Surprisingly, from the out-of-band distortion and the SER performance, the LMS algorithm is superior to the RLS algorithm for this case. However, the overall results show that the proposed schemes can slightly reduce the amount of PAPR only. This is because the aim of the proposed techniques does not focus on the PAPR reduction but does assist the conventional PAPR reductions to equalize the clipped signal before sending to all transmitting antennas. By this idea, the clipped signal from all PAPR reductions has nearly the same characteristic as the unclipped signal as the low level of PAPR as shown in Figure 7.13. As a result, the out-of-band distortion and the error rate can be decreased in the large-scale MIMO-OFDM systems effectively.

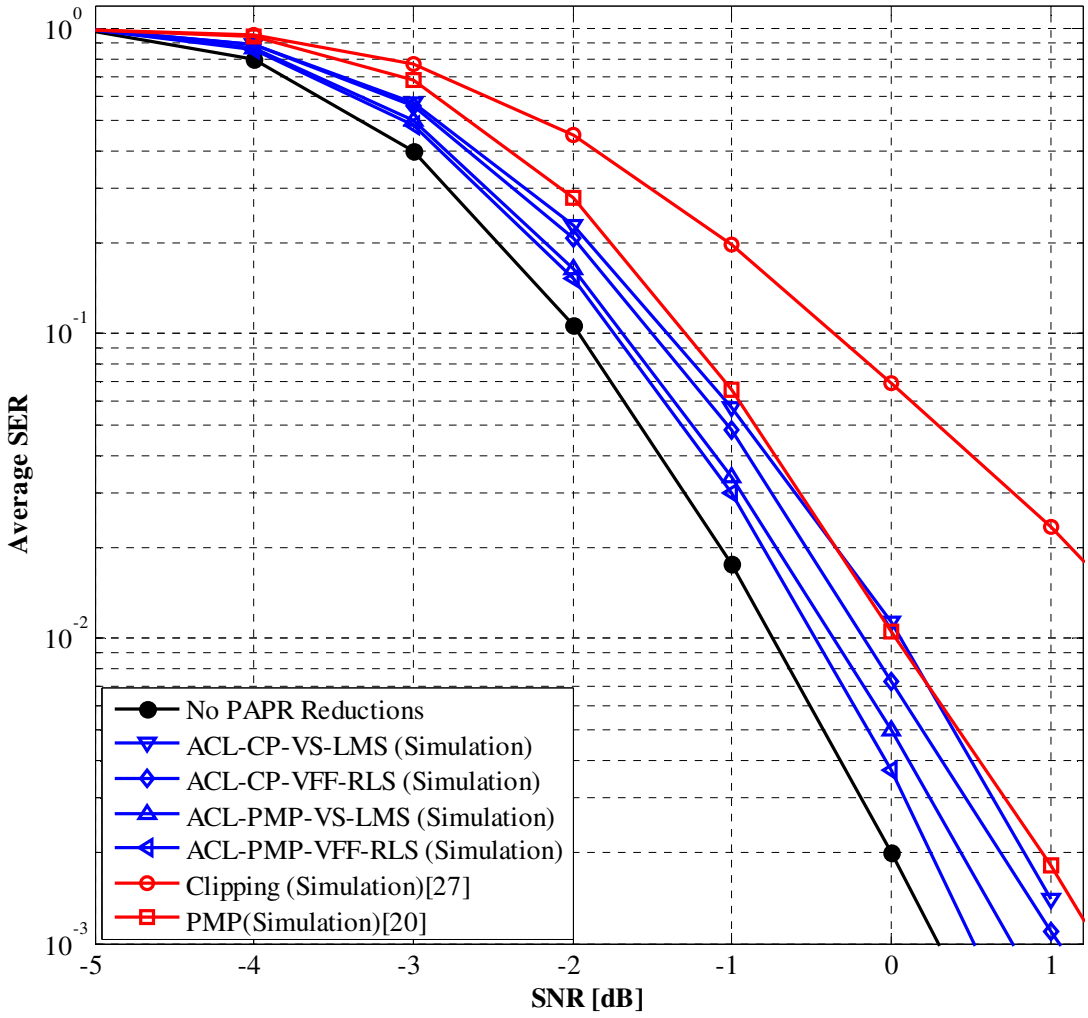


Figure 7.11 The SER performance of all proposed techniques under the perfect CSI.

Like a double–edged sword, the complexity of the proposed schemes seems like to be improving. The least complexity is the CP-LMS, but the most complexity is the PMP-RLS. One of the values that define their complexity in the term of FLOPs counting is the number of the signal repetition $N_{rep}$. For this case, the adaptive algorithm needs to improve the convergence rate to be faster than the proposed algorithms in the future. Another factor for the PMP to avoid the more complexity is the number of iterations $Z_{PMP}$ in a FITRA algorithm. This value is an important value that adds to the complexity of the systems. Like signal repetition $N_{rep}$, it is necessary to be developed to be less in the future.

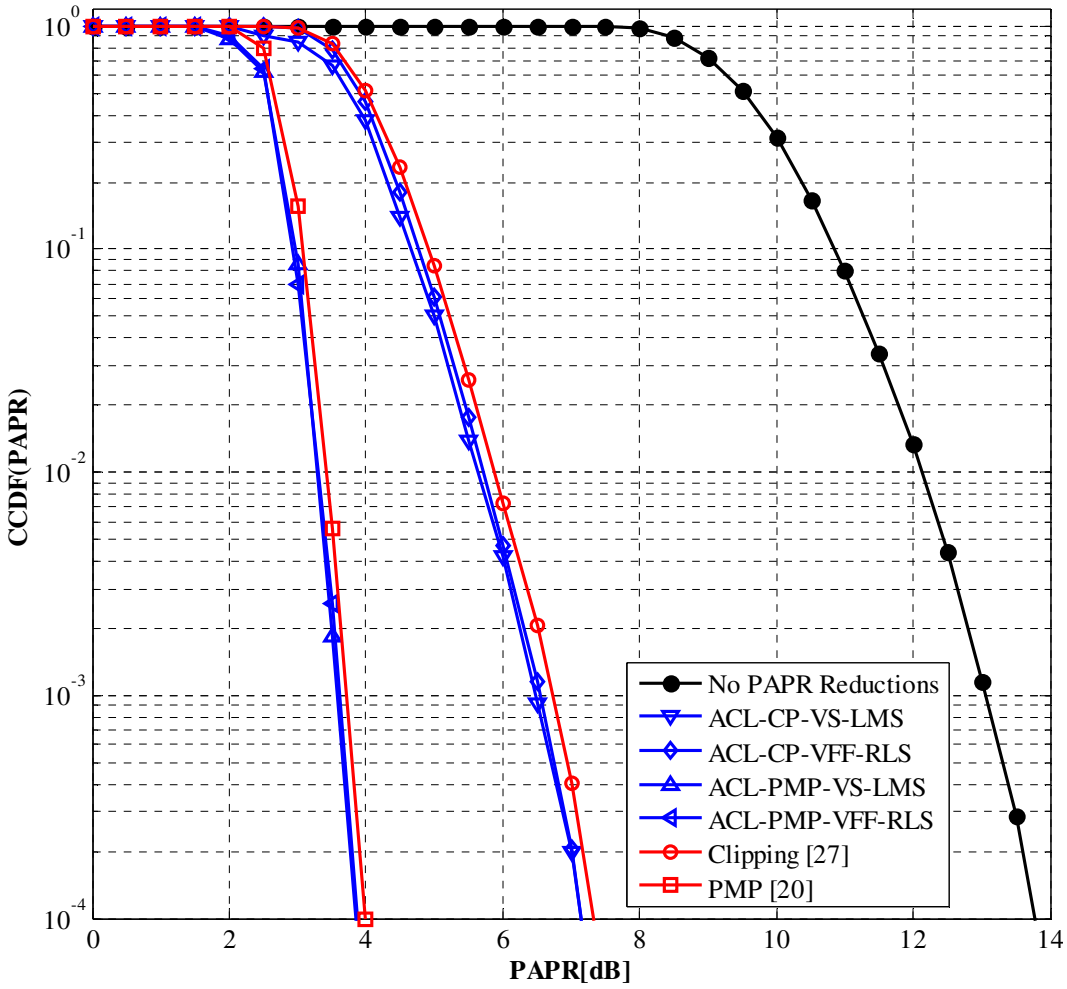


Figure 7.12 The CCDF (PAPR) performances of each scheme with the SER feedback.

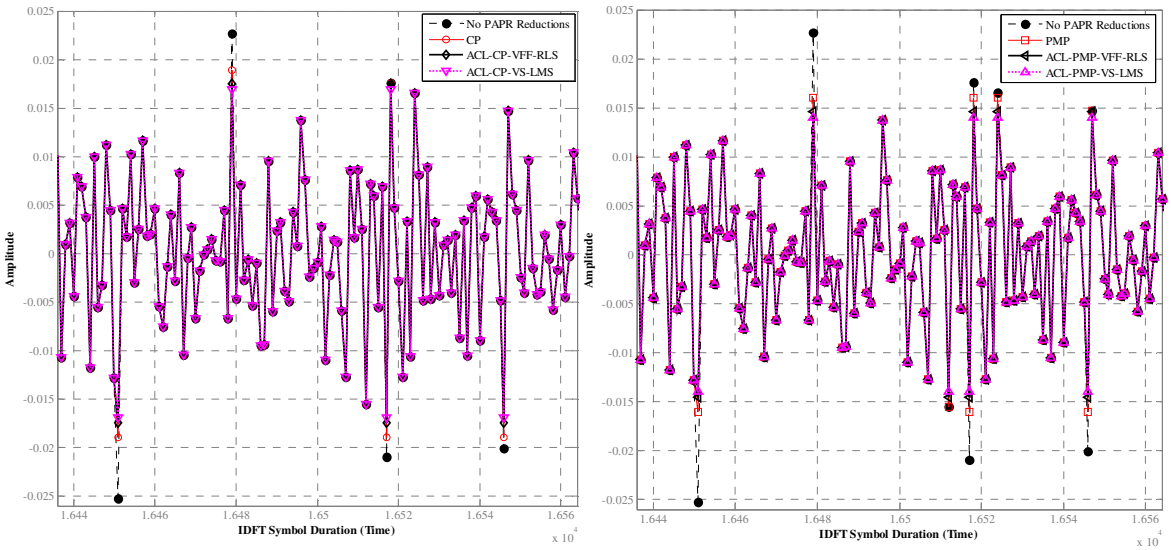


(a) The CP (b) The PMP

Figure 7.13 The unclipped signals, the clipped signals, and the proposed optimizing signals.

In terms of the large-scale MIMO, the ACL-PMP-VFF-RLS method is chosen to compare the performance of antennas varied from 10 to 1000. As shown in Figures 7.14 and 7.15, both the SER and CCDF (PAPR) performances are presented. At $E_b/N_0$ = -2dB, Figure 7.14 shows that the SER performance is nearly the same for $n_t$ = 600, 800, and 1000. The gap of SER performance from $n_t$ = 600 to 1000 is only 0.004625 while $n_t$ = 200 to 600 it is 0.044125 (an order of 10 difference). The reason for this is when the number of antennas at the BS is increased, the SER is reduced. It causes the feedback of SER for high numbers of antennas ($n_t$ = 600 and 1000) to be neary the same, while the amount of PAPR shown in Figure 7.15 (for the CCDF method) increases continuously. For this reason, it affects the overall performance of the proposed technique that is not as good as expected.

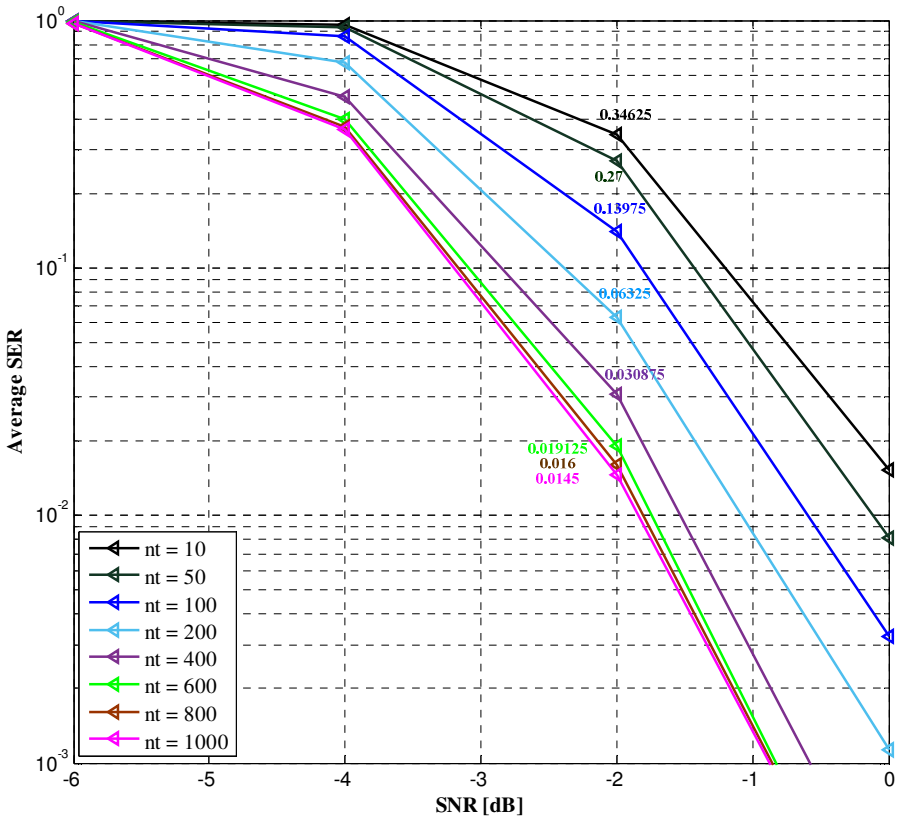


Figure 7.14 The SER performance of the ACL-PMP-VFF-RLS ($n_t$ = 10 to 1000).

Even though the proposed technique (ACL-PMP-VFF-RLS) gives the best SER performance at $n_t$ = 1000, further research is required to positively improve the performance. The gap of the PAPR from $n_t$ = 600 to $n_t$ = 1000 is approximately 2.5dB nearly the same at from $n_t$ = 200 to $n_t$ = 600 (approximately 3.5dB) while the results of the SER performance are very different. For future research, this problem

needs to be addressed. The decrease of SER at a high number of antennas should be consistent with the increase in PAPR.

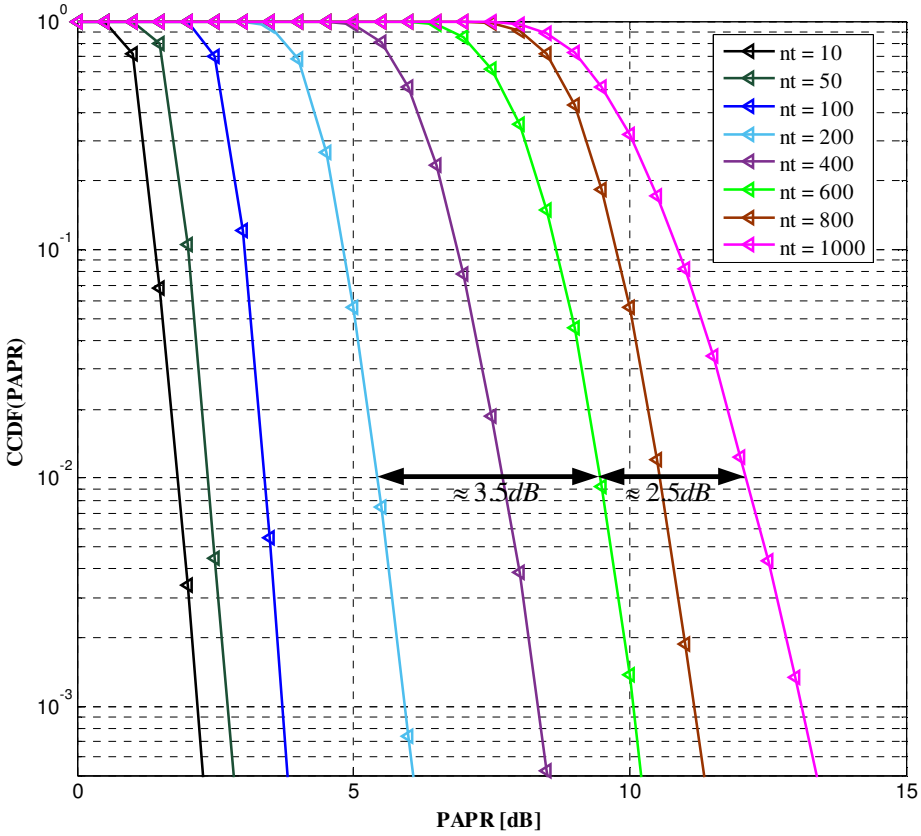


Figure 7.15 The CCDF (PAPR) performances of the ACL-PMP-VFF-RLS ($n_t$ = 10 to 1000).

It is very difficult to choose which one is the best scheme of the proposed techniques because each approach has different strengths and weaknesses. At the end of this chapter, the radar graphs are presented to make it easier to decide which one is the appropriated scheme for the practical tasks of the MIMO-OFDM systems. A radar graph is divided into five parts; the symbol error rate, the amount of PAPR, the complexity, the imperfect CSI (in the case of no SER feedback from all users), and the number of the overhead. There is a score range for each part on a range of one to ten; one is the lowest and ten is the highest. [3]All the radar graphs can be shown in Figure 7.16.

The overall performance of the original CP can be shown in Figure 7.16 (a). The advantages of this approach are the low overhead and complexity, and it can also be used in the case that the feedback capacity is limited and this will affect the

[3] The more areas are covered for the graph, the poorer system is provided for itself.

resolution and quality of the SER feedback at the BS. The proposed CP can be shown in Figures 7.16 (b) and 7.16 (c), which are the CP-LMS and the CP-RLS respectively. In this case, the CP-RLS seems superior to the CP-LMS in every part except the complexity, which the complexity score of the CP-RLS is 4.5, and the CP-LMS is 4.

The original PMP performance can be shown in Figure 7.16 (d). As the same of the original CP, the low overhead and complexity, and the high performance in the case of imperfect CSI are the advantages of the PMP compared with the proposed PMP as shown in Figures 7.16 (e) and 7.16 (f) respectively. The lowest of the SER, the amount of PAPR, the overhead, is the PMP-RLS. Moreover, it can be used in the case of the ill-conditioned behaviour of the MIMO channel effectively but its disadvantage is the highest complexity instead. Note that the complexity of the PMP-LMS is lower than the PMP-RLS for this case.

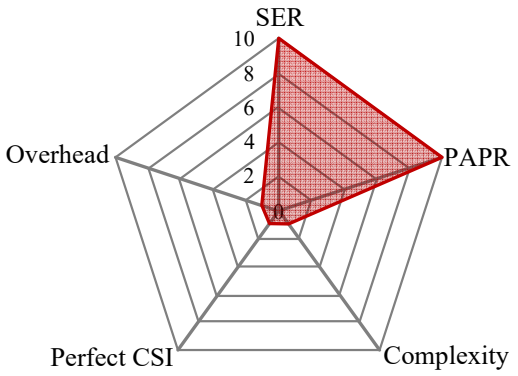


(a) CP

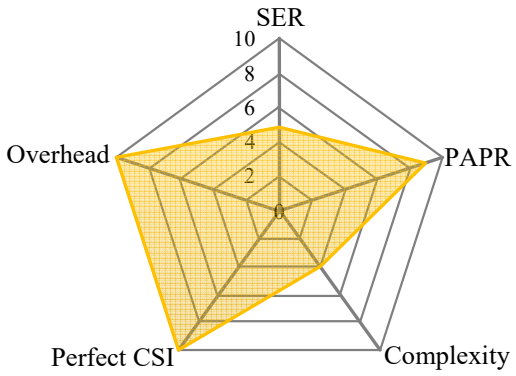


(b) CP-LMS

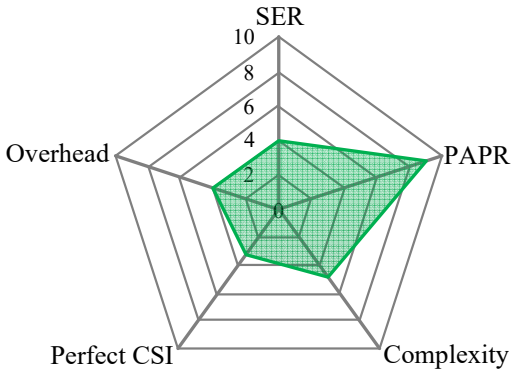


(c) CP-RLS

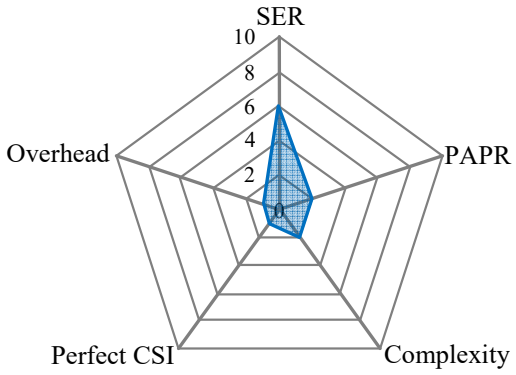


(d) PMP

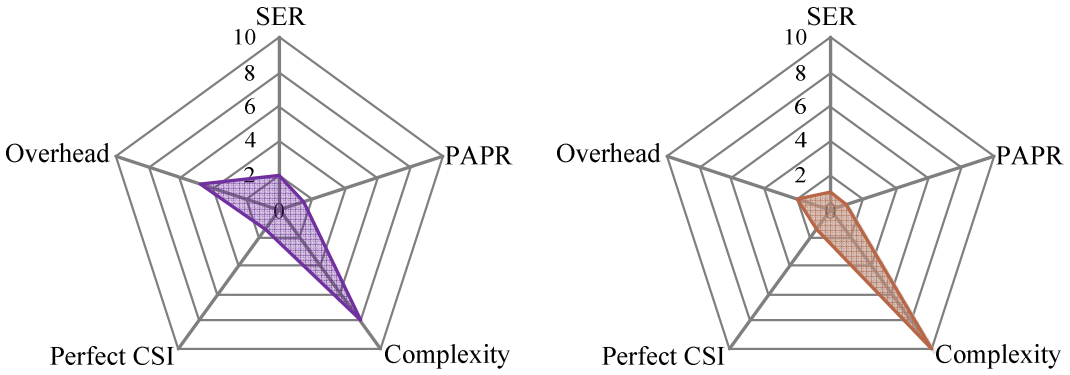


(e) PMP-LMS (f) PMP-RLS

Figure 7.16 The performance comparisons of the proposed schemes.

The next chapter is the last chapter of this thesis. It will provide the conclusion of every chapter and will also present the discussion of the future research on this project.

# Chapter 8

# Conclusions and Future Works

## 8.1 Summary

This thesis presents a novel tool to support the adjustable clipping level of the PAPR reductions. It includes the CP with LMS algorithm (CP-LMS), the CP with RLS algorithm (CP-RLS), the PMP with LMS algorithm (PMP-LMS), and the PMP with RLS algorithm (PMP-RLS) respectively. In the term of the new versions of both clipping and PMP schemes were represented in Chapter 4. The APO using both the variable LMS algorithm and the variable RLS algorithm were invented in Chapter 5. These innovations employ the benefit of the SER feedback from all users in the WLAN cell to adapt themselves to suit the situation of the transmission channel. Moreover, their system performance analyses are derived in Chapter 6 to prove their theory on each SER performance results in Chapter 7.

This chapter summaries the major contributions drawn from this thesis and presents future research directions arising from this work.

## 8.2 Conclusions

In this thesis, the major contributions are presented and investigated in different chapters.

In Chapter 4, the adjustable PAPR reduction level controlled with SER feedback was presented and investigated. The objective was to modify the conventional PAPR reductions of both clipping and PMP to use the benefit of CSI. The users' symbol error rate is fed to the BS to adjust the PAPR clipping level to save the unnecessary energy in the downlink large-scale OFDM-MIMO systems. In Figure 7.2, the experimental results indicate that the proposed PAPR reduction schemes can decrease the sided-leakage power more than the conventional PAPR reductions in the terms of both clipping and PMP respectively. Simulation results also demonstrate that the proposed techniques can reduce nonlinear distortions in memoryless RF amplifiers causing high symbol error rate in systems effectively.

In Chapter 5, an APO that is used to optimise the signals between the clipped signal and the original signal was invented. The objective was to equalise the clipped signal before sending to each antenna in the large-scale antenna systems. It also employs users' SER feedback to adapt its update algorithm to improve the quality of the transmitted signals. Both LMS and RLS algorithms were chosen to apply to be variable algorithms for this technique. Moreover, the proposed variable algorithms can be switched to the proposed FS in the case of the imperfect CSI, which is that all users cannot send SER feedback to a BS perfectly.

By the cooperation between the adjustable PAPR reduction level in Chapter 4 and the APO in Chapter 5, simulation results show that the existing techniques are outperformed by the proposed techniques in terms of both SER and CCDF-PAPR performances effectively.

Finally, the work in this thesis moves the research on cooperative systems based signal processing techniques a step forward. It is the first time of the PAPR problem solutions that uses both the adjustable PAPR clipping level and the optimising signal process. They also employ the feedback of all terminals to adapt themselves to suit the situation of the transmission channel. Therefore, efficient design of the PAPR reduction methods and signal processing algorithms that overcome the effects of the

high dynamic range of the PAPR signals are proposed. In this thesis, four different approaches were proposed namely: the CP-LMS, the CP-RLS, the PMP-LMS, and the PMP-RLS respectively. The work in this thesis provides new techniques of the PAPR reduction methods and is helpful for further study of signal processing in future wireless networks such as 5G networks.

## 8.3 Future Work

Many future research directions or investigations in the area of cooperative systems based signal processing techniques for PAPR reductions arise from these topics presented in this thesis.

1. *The adjustable PAPR reduction level*. As previously mentioned, both clipping and PMP methods were chosen to be applied in this thesis. They have been modified to clip the high PAPR as the iterative loop controlled with users' SER feedback. Though the flexibility of the proposed method, a variety of techniques may be utilized for adjusting the PAPR reduction level such as peak windowing, inter-carrier interference cancellation, random phase updating, or a companding scheme.

2. *The structure of the APO.* As mentioned in Chapter 5, the APO was based on the digital filter. Currently, many structures can be used for the digital filter theory such as cascade FIR, linear-phase FIR, polyphase FIR, infinite impulse response (IIR), decision feedback equaliser (DFE), etc. They can be applied in the APO's structure.

   Even though many structures can be replaced in the APO's structure, one aspect needs to be considered. Note that in Chapter 7, a value that critically increases the system complexity is the length of the structure, $L$, which should be particularly considered to desire its new structure.

3. *The updated algorithms*. The updated algorithms of the APO employ the modified algorithms based on both LMS and RLS. They take advantage of the CSI to adapt themselves to equalise the clipped signals tackling the ill-behaved power amplifiers in the systems.

However, in the digital filter theory, there are also many types of updated algorithms that are waiting to apply to use in the APO's algorithm. They all include normalized LMS, affine projection LMS, sign-data LMS, fast RLS, square root RLS, etc.

Note that in section 5.5 of Chapter 5, the number of the signal repetition, $N_{rep}$, is the very important value to design a new algorithm. It increases the overhead to process in the BS. This value also increases the processing time, the heat in the BS, and transmission power. Therefore, one thing that needs to be considered in the new algorithm design is the small number of the signal repetition.

4. *The implementation and verification*. The implementation on the practical system cannot be done with multiple limiting factors while doing this research such as budget, people, and time. Four aspects may be focused on the real system of this research in the future.

    - *The synchronization*. It is the essential task for typical massive MIMO-OFDM antenna arrays. It requires the reliable reception of the transmitted signals. From the perspective of physical layer design, proper synchronization algorithms are crucial to build a successful transmission system.

    - *The limited battery power in the uplink transmission*. The transmitted signals in an OFDM system can have high peak dynamic ranges in the time domain since many subcarrier components are added by an IDFT process. In this thesis, the downlink system was only considered to tackle the PAPR problems with unlimited power at the BS. On the other hand, in the practical uplink large-scale MIMO-OFDM systems, the transmission power in the terminals may have been limited. This may be degrading the efficiency of the power amplifier in the terminal. The PAPR problem is more important in the uplink since the efficiency of power amplifier is critical due to the limited battery power in a mobile terminal.

- *The antenna array configuration*. According to the ability of array to radiate the signals in the large-scale MIMO-OFDM systems, the antenna array configurations are classified into 2-dimensions and 3-dimensions antenna arrays. Practically, 2-dimensions antenna array is the linear antenna array, and the rectangle, spherical, and cylindrical antenna array belong to 3D antenna array respectively.

  In this thesis, the antenna array configuration was assumed to be the 2-dimensions antenna array, and many negative effects from the realistic situations were skipped in 3-dimensions antenna system. They include near-far effects, the nonstationary phenomenon of both azimuth and elevation angle in the transmitted signals, etc.

- *FPGA Processing Level*. This project will be developed in the physical layer with the Software Defined Radio (SDR). SDR is considered as a wireless device controlled and reconfigured by software [130]. In addition, it has been widely acceptable from wireless communication developers over the last ten years. It can change modulation and switch the channel depending on its surrounding environment. It can also adapt itself according to the other parameters outside the SDR board [131-132].

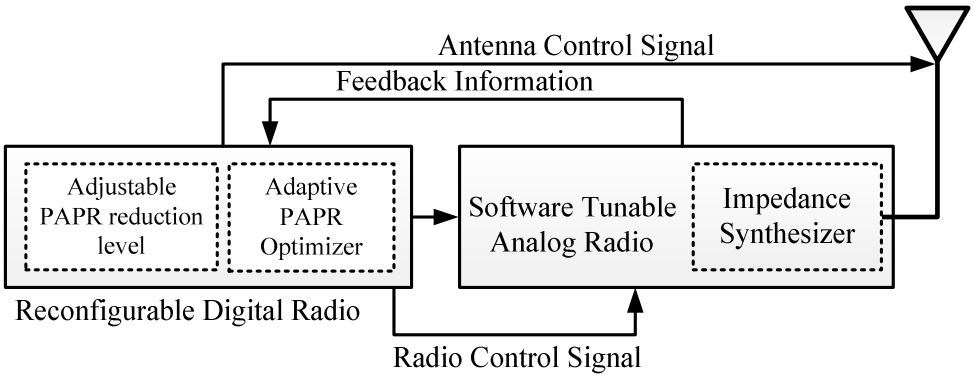


Figure 8.1 [1]The proposed technique on the ideal SDR architecture.

These are the four main areas of future research that they may affect the PAPR problems in the implementation of the large-scale MIMO-OFDM

[1] The Software Tunable Analog Radio is consisted of RF filters, combiners/splitters, data converter, power amplifier respectively.

systems. Moreover, various problems in the realistic system may occur such as the hardware issues, the embedded software process, the channel modelling problem, the pilot contamination problems, etc. They still need to be further investigated for PAPR reduction improvements in the next steps.

5. *The future publication plan*. Publication has occurred at the 2016 International Conference on Wireless Communications and Network Technology (ICWCNT2016). The title is 'The Adaptive PAPR Optimizer for PAPR Clipping in MIMO-OFDM systems' [80]. The next step will be to publish the new version of PMP that has been presented in Chapter 5, the SER performance analysis in Chapter 6, and the additional simulation results in Chapter 7. The author will target high-quality journal publications from this thesis.

From a long journey through chapter 1 to chapter 7, it can be seen that the introduction of the state of the art technology was represented from chapter 1 to chapter 3. Both chapter 4 and chapter 5 were the proposed techniques including their analysis performances in chapter 6. The simulation results and the discussion were provided in chapter 7. Finally, the conclusions and future works of this thesis can be shown in chapter 8.

# References


[1] J. Hoydis, S. Ten Brink, and M. Debbah, "Massive MIMO in the UL/DL of cellular networks: how many antennas do we need?," *IEEE J. Sel. Areas Commun.*, vol. 31, no. 2, pp. 160–171, Feb. 2013.

[2] D. Tse and P. Viswanath, *Fundamentals of wireless communication*. Cambridge, UK: Cambridge University Press, 2005.

[3] A. Chockalingam and B. S. Rajan, *Large MIMO systems*. Cambridge, UK: Cambridge University Press, 2014.

[4] Y. Mehmood, W. Afzal, F. Ahmad, U. Younas, I. Rashid, and I. Mehmood, "Large scaled multi-user MIMO system so called massive MIMO systems for future wireless communication networks," in *Proc. IEEE Automation and Comput.*, London, UK, Sep. 2013, pp. 1–4.

[5] F. Rusek, D. Persson, B. Lau, and E. Larsson, "Scaling up MIMO: opportunities and challenges with very large arrays," *IEEE Signal Process. Mag.*, vol. 30, no. 1, pp. 40–60, 2013.

[6] A. L. Swindlehurst, E. Ayanoglu, P. Heydari, and F. Capolino, "Millimeter-wave massive MIMO: The next wireless revolution?," *IEEE Commun. Mag.*, vol. 52, no. 9, pp. 56–62, 2014.

[7] M. Kountouris and N. Pappas, "HetNets and massive MIMO: Modeling, potential gains, and performance analysis," in *Proc. IEEE Antennas and Propagation in Wireless Communications*, Torino, Italy, Sep. 2013, pp. 1319–1322.

[8] J. G. Proakis, *Digital Communications, 4th ed*. Columbus, USA: McGraw-Hill Education, 2001.

[9] S. B. Weinstein and P. M. Ebert, "Data transmission by frequency-division multiplexing using the discrete Fourier transform," *IEEE Trans. Commun.,* vol. 19, no. 5, pp. 628–634, Oct. 1971.

[10] M. A. Mohamed, A. S. Samarah, and M. I. Fath Allah, "Study of performance parameters effects on OFDM systems," *IJCSI Int. J. Comp. Sci.*, vol. 9, no. 2, May 2012.

[11] R. van Nee and R. Prasad, *OFDM for Wireless Multimedia Communications*. Norwood, USA: Artech House Publishers, 2000.

[12] L. Ward, "802.11 ac Technology Introduction: White Paper," ROHDE&SCHWARZ.

[13] AiSLab, Beyond 4G and 5G Wireless Mobile Communications, January 2017. [Online]. Available: http://ais.unist.ac.kr/?page_id=211

[14] R. A. Abdelaal, A. S. Behbahani, and A. M. Eltawil, "On the performance of massive MIMO Cellular systems with power amplifiers," in *Proc. IEEE Wireless Telecommunications Symposium*, Washington, DC, USA, Apr. 2014, pp. 1–5.

[15] A. Jayalath, "OFDM for wireless broadband communications (peak power reduction, spectrum and coding)," Ph.D. dissertation, School of Computer Science and Software Engineering, Monash University, May 2002.

[16] S. C. Cripps, *RF Power Amplifiers for Wireless Communications*, Norwood, USA: Artech House Publishers, 2006.

[17] P. Banelli, G. Baruffa, and S. Cacopardi, "Effects of HPA nonlinearity on frequency multiplexed OFDM signals," *IEEE Trans. Broadcast*., vol. 47, no. 2, pp. 123–136, June 2001.

[18] I. Ahmad, A. I. Sulyman, A. Alsanie, A. Alasmari, and S. Alshebeili, "Spectral Re-growth due to High Power Amplifier Nonlinearities in MIMO-OFDM Relaying Channels," in *Proc. IEEE The Sixth International Conference on Broadband and Biomedical Communications*, Melbourne, Australia, Nov. 2011, pp. 240-245.

[19] G. Wunder, R. F. H. Fischer, H. Boche, S. Litsyn, and J. S. No, "The PAPR problem in OFDM transmission: New directions for a long-lasting problem," *IEEE Signal Process. Mag*., vol. 30, no. 6, pp. 130–144, 2013.

[20] N. N. N. A. Malik, N. Ngajikin, S. M. Idrus, and N. D. A. Latif, "Peak to average power ratio (PAPR) reduction in OFDM system," in *Proc. IEEE International RF and Microwave Conference*, Putrajaya, Malaysia, Sept. 2006, pp. 75-79.

[21] C. Studer and E. G. Larsson, "PAR-aware large-scale multi-user MIMO-OFDM downlink," *IEEE J. Sel. Areas Commun*., vol. 31, no. 2, pp. 303–313, Feb. 2013.

[22] S. K. Mohammed and E. G. Larsson, "Per–antenna constant envelope precoding for large multi–user MIMO systems," *IEEE Trans. Commun*., vol. 61, no. 3, pp. 1059–1071, Mar. 2013.

[23] A. Wakeel and W. Henkel, "Least-squares iterative PAR reduction for point-to-point large-scale MIMO-OFDM systems," in *Proc. IEEE International Conference on Communication*, Sydney, Australia, Jun. 2014, pp. 4638–4643.

[24] H. Prabhu, O. Edfors, J. Rodrigues, L. Liu, and F. Rusek, "A low complex peak-to-average power reduction scheme for OFDM based massive MIMO systems," in *Proc. IEEE International Symposium on Communications, Control and Signal Processing*, Athens, Greece, May 2014, pp. 114–117.

[25] M. Hu, Y. Li, W. Wang, and H. Zhang, "A piecewise linear companding transform for PAPR reduction of OFDM signals with companding distortion mitigation," *IEEE Trans. Broadcasting*, vol. 60, no. 3, pp. 532–539, Sept. 2014.

[26] T. Jiang, C. Ni, C. Xu, and Q. Qi, "Curve fitting based tone reservation method with low complexity for PAPR reduction in OFDM systems," *IEEE Commun. Lett*., vol. 18, no. 5, pp. 805–808, Aug. 2014.

[27] A. Ali, A. A. Rabah, M. Masood, and T. Y. Al-Naffouri, "Receiver-based recovery of clipped OFDM signals for PAPR reduction: A Bayesian approach," *IEEE Access*, vol. 2, pp. 1213–1224, Oct. 2014.

[28] K. Panta and J. Armstrong, "Effects of clipping on the error performance of OFDM in frequency selective fading channels," *IEEE Trans. Wirel. Commun*., vol. 3, no. 2, pp. 668–671, Mar. 2004.

[29] S. Andersson and Z. Zhang "Crest factor reduction using peak strainer," Master's thesis, Department of Signals & Systems, Chalmers University of Technology, 2013.

[30] T. Udomsripaiboon, C. Mingkwan, C. Benjangkaprasert, O. Sangaroon, and K. Janchitrapongvej, "Soft output decision feedback equalizer using variable step-size algorithm for turbo coded DS/CDMA systems," in *Proc. IEEE International Symposium on Intelligent Signal Processing and Communication Systems*, Hong Kong, China, Dec. 2005, pp. 505–508.

[31] T. Udomsripaiboon, K. Sieangjen, T. Kungwanchai, N. Sanpote, C. Benjangkaprasert, “The variable step-size algorithm for decision feedback equalizer turbo code DS/CDMA system using SOVA algorithm,” in *Proc. IEEE International Conference on Advanced Communication Technology*, Gangwon-Do, South Korea, Feb. 2008, pp. 598–601.

[32] R. Kudo, S. Armour, J. P. McGeehan, and M. Mizoguchi, “Channel state information feedback method for massive MIMO OFDM,” *IEEE Journal of Commun. and Networks*, vol. 15, no. 4, pp. 352-361, Sept. 2013.

[33] S. M. Webb, J. G. Ellison, S. R. Desbruslais, M. P. Fedoruk, and S. K. Turitsyn, “Adaptive pulse shaping through BER feedback,” *IEEE Journal of Lightwave Technology*, vol. 27, no. 17, pp. 3765-3772, Apr. 2009.

[34] Qualcom Inc., *The 1000× Data Challenge*, Nov. 2013. [Online]. Available: https://www.qualcomm.com/media/documents/files/1000x-mobile-data-challenge.pdf

[35] Ericson, *5G Radio Access-Research and Vision*, June 2013. [Online]. Available: https://www.ericsson.com/mx/res/docs/whitepapers/wp-5g.pdf

[36] Cisco, *Cisco Visual Networking Index: Global Mobile Data Traffic Forecast Update*, *2015–2020 White Paper*, Sept. 2016. [Online]. Available: http://www.cisco.com/c/en/us/solutions/collateral/service-provider/visual-networking-index-vni/mobile-white-paper-c11-520862.html.

[37] H. Q. Ngo, “Massive MIMO: Fundamentals and System Designs,” Ph. D. dissertation, Linkoping University, Linkoping, Sweden, Jan. 2015.

[38] D. Gesbert, M. Kountouris, R. W. Heath Jr., C. B. Chae, and T. Salzer, “Shifting the MIMO paradigm,” *IEEE Signal Process. Mag*., vol. 24, no. 5, pp. 36-46, Sep. 2007.

[39] M. Kobayashi, N. Jindal, and G. Caire, “Training and feedback optimizationfor multiuser MIMO downlink,” *IEEE Trans. Commun*., vol. 59, no. 8, pp.2228-2240, Aug. 2011.

[40] V. Stankovic and M. Haardt, “Generalized design of multiuser MIMO precoding matrices,” *IEEE Trans. Wireless Commun*., vol. 7, pp. 953-961, Mar.2008.

[41] G. Caire and S. Shamai, “On the achievable throughput of a multi-antenna Gaussian broadcast channel,” *IEEE Trans. Inf. Theory*, vol. 49, no. 7, pp.1691-1706, Jul. 2003.

[42] P. Viswanath and D. N. C. Tse, “Sum capacity of the vector Gaussian broadcast channel and uplink-downlink duality,” *IEEE Trans. Inf. Theory*, vol. 49, no. 8, pp. 1912-1921, Aug. 2003.

[43] T. Yoo and A. Goldsmith, “On the optimality of multiantenna broadcast scheduling using zero-forcing beamforming,” *IEEE J. Sel. Areas Commun*., vol. 24, no. 3, pp. 528-541, Mar. 2006.

[44] S. Verdú, *Multiuser Dectection*. Cambridge. UK: Cambridge University Press, 1998.

[45] N. Jindal and A. Goldsmith, “Dirty-paper coding vs. TDMA for MIMO broadcast channels,” *IEEE Trans. Inf. Theory*, vol. 51, no. 5, pp. 1783-1794, May 2005.

[46] C. Suh, M. Ho, and D. N. C. Tse, “Downlink interference alignment,” *IEEE Trans. Commun*., vol. 59, no. 9, pp. 2616-2626, Sep. 2011.

[47] F. M. M. Barboza, J. S. Garcia, L. S. Equigua, F. R. C. Soria, and J. F. Troncoso, “User scheduling algorithms in multiuser massive MIMO systems towards 5G,” *IEEE Latin America Trans*., vol. 13, no. 12, pp. 3781-3787, Feb. 2016.

[48] E. G. Larsson, O. Edfors, F. Tufvesson, and T. L. Marzettaactions, “Massive MIMO for next generation wireless systems,” *IEEE Comm. Mag*., vol. 52, no. 2, pp. 186-195, Feb. 2014.

[49] L. Dai, X. Gao, S. Han, C. L. I, Z. Wang, *Near-optimal linear precoding with low complexity for massive MIMO*, Sept. 2016. [Online]. Available: http://arxiv.org/abs/1411.4141

[50] Y. S. Cho, J. Kim, W. Y. Yang, and C.G. Kang, *MIMO-OFDM Wireless Communications with MATLAB*. New York, USA: John Wiley & Sons, 2005.

[51] N. Revuelto, “PAPR reduction in OFDM systems,” Master Thesis, Universitat Politècnica de Catalunya, Barcelona, Spain, Sept. 2008.

[52] S. Andersson and Z. Zhang, “Crest Factor Reduction Using Peak Strainer,” Master Thesis, Chalmers University of Technology, Gothenburg, Sweden, 2013.

[53] A. Katz, *Linearizing high power amplifiers*, Sept. 2016. [Online]. Available: http://www.lintech.com/PDF/hpa.pdf

[54] I. Ahmad, A. I. Sulyman, A. Alsanie, A. K. Alasmari, and S. A. Alshebeili, "Spectral broadening effects of high-power amplifiers in MIMO-OFDM relaying channels," *EURASIP J. Wireless Commun. and Networking*, vol. 1, Feb. 2013.

[55] P. Zetterberg, *RF Lecture*, Sept. 2016. [Online]. Available: http://slideplayer.com/slide/5813384/

[56] D. Dardari, V. Tralli, and A. Vaccari, "A novel low complexity technique to reduce non-linear distortion effects in OFDM systems," in *Proc. IEEE The Ninth IEEE International Symposium Personal, Indoor and Mobile Radio Communications*, Boston, USA, Sept. 1998, pp. 795–800.

[57] H. Rowe, "Memoryless nonlinearities with Gaussian inputs: Elementary results," *Bell Syst. Tech. J.*, vol. 61, pp. 1519–1525, Sept. 1982.

[58] R. van Nee and R. Prasad, *OFDM for Wireless Multimedia Communications*. Boston: Artech House Publishers, Mar. 2000.

[59] A. Saleh, "Frequency-independent and frequency-dependent nonlinear models of TWT amplifiers," *IEEE Trans. Commun*., vol. 29, no. 11, pp. 1715–1720, Nov. 1981.

[60] ——, "Intermodulation analysis of FDMA satellite systems employing compensated and uncompensated TWT's," *IEEE Trans. Commun*., vol. 30, pp. 1233–1242, May 1982.

[61] A. Jayalath, "OFDM for wireless broadband communications (peak power reduction, spectrum and coding)," Ph.D. dissertation, School of Computer Science and Software Engineering, Monash University, May 2002.

[62] E. Lawrey and C. Kikkert, "Peak to average power ratio reduction of OFDM signals using peak reduction carriers," in *The Fifth International Symposium on Signal Processing and Its Applications*, Brisbane, Australia, Aug. 1999, pp. 737–740.

[63] J. Tellado, "Peak to average power reduction for multicarrier modulation," Ph.D. dissertation, Stanford University, Sept. 1999.

[64] R. van Nee and A. de Wild, “Reducing the peak-to-average power ratio of OFDM,” in *Proc. IEEE Vehicle Technology Conference*, Ottawa, Canada, May 1998, pp. 2072–2076.

[65] A. D. S. Jayalath and C. Tellambura, “Peak-to-average power ratio of IEEE 802.11a PHY layer signals,” in *Proc. IEEE International Symposium on DSP for Communication Systems*, Manly-Sydney, Australia, Jan. 2002, pp. 31–36.

[66] Telecomhall, *What is Envelope Tracking?*, Oct. 2016. [Online]. Available: http://www.telecomhall.com/what-is-envelope-tracking.aspx.

[67] S. H. Han and J. H. Lee, “An overview of peak-to-average power ratio reduction techniques for multicarrier transmission,” *IEEE Trans. Wireless Commun*., pp. 56–65, Apr. 2005.

[68] T. Jiang and Y. Wu, “An overview: Peak-to-average power ratio reduction techniques for OFDM signals,” *IEEE Trans. Broadcast*., vol. 54, no. 2, pp. 257–268, June 2008.

[69] B. Torun, “Peak-to-average power ratio reduction techniques for wavelet packet modulation,” Master Thesis, Delft University of Technology, Oct. 2010.

[70] R. Bauml, R. Fischer, and J. Huber, “Reducing the peak-to-average power ratio of multicarrier modulation by selected mapping,” *Electronics Letters*, vol. 32, pp. 2056 – 2057, 1996.

[71] S. Muller and J. Huber, “OFDM with reduced peak-to-average power ratio by optimum combination of partial transmit sequences,” Electronics letters, vol. 33, no. 5, 1997.

[72] A. Jayalath and C. Tellambura, “The use of interleaving to reduce the peak-toaverage power ratio of an ofdm signal,” *in IEEE Global Telecommunications Conference, 2000*, vol. 1, pp. 82 –86, 2000.

[73] J. Tellado, *Multicarrier modulation with low PAR: applications to DSL and wireless*. Springer Netherlands, 2000.

[74] D. Kim and G. Stuber, “Clipping noise mitigation for OFDM by decision-aided reconstruction,” *IEEE Communications Letters*, vol. 3, no. 1, pp. 4–6, 1999.

[75] H. Prabhu, O. Edfors, J. Rodrigues, L. Liu, and F. Rusek, “A low complex peak-to-average power reduction scheme for OFDM based massive MIMO systems,” in *Proc. IEEE International Symposium on Communications, Control and Signal Processing*, Athens, Greece, May 2014, pp. 114–117.

[76] H. Y. Liang, G. L. Huang, H. S. Chen, and C. B. Lin, "Tone reservation scheme based on |ulu + v| construction for PAPR reduction in OFDM systems," in *Proc. IEEE Wireless and Optical Communication Conference*, Chongqing, China, May 2013, pp. 147–150.

[77] T. May and H. Rohling, "Reducing the peak-to-average power ratio in OFDM radio transmission systems," *Proc. of IEEE Vehicular Technology Conference, VTC 98*, pp. 2774–2778, 1998.

[78] H. Nikookar and K. Lidsheim, "Random phase updating algorithm for OFDM transmission with low PAPR," *IEEE Transactions on Broadcasting*, vol. 48, no. 2, pp. 123–128, 2002.

[79] X. Wang, T. Tjhung, and C. Ng, "Reduction of peak-to-average power ratio of OFDM systems using a companding technique," *IEEE Transactions on Broadcasting*, vol. 45, no. 3, 1999.

[80] T. Udomsripaiboon, J. Billingsley, and A. Maxwell, "The adaptive PAPR optimizer for PAPR Clipping in MIMO-OFDM systems," in *International Conference on Wireless Communications and Network Technology*, Guangzhou, China, June 2016.

[81] J. Armstrong, "Peak-to-average power reduction for OFDM by repeated clipping and frequency domain filtering," *IEEE Elec. Lett*., vol. 38, no. 5, pp. 246–247, Feb. 2002.

[82] A. Gusmao and R. Dinis, "Iterative receiver techniques for cancellation of deliberate nonlinear distortion in OFDM-type transmission," in *Int. OFDM Workshop04*, Dresden, German, Sept. 2004.

[83] P. R. Lasya and M. S. Kumar, "PAPR and out-of-band power reduction in OFDM-based cognitive radios," in *Proc. IEEE International Conference on Signal Processing And Communication Engineering Systems*, Guntur, India, Jan. 2015, pp. 473-476.

[84] S. Leung, S. Ju, and G. Bi, "Algorithm for repeated clipping and filtering in peak-to-average power reduction for OFDM," *IEE Elect. Lett*., vol. 38, no. 25, pp. 1726–1727, Dec. 2002.

[85] H. Chen and A. Haimovich, "Iterative estimation and cancellation of clipping noise for OFDM signals," *IEEE Commun. Lett*., vol. 7, no. 7, pp. 305–307, July 2003.

[86] ——, “An iterative method to restore the performance of clipped and filtered OFDM signals,” in *Proc. IEEE International Conference Communications*, Alaska, USA, vol. 5, May 2003, pp. 3438–3442.

[87] C. Sharma, P. K. Sharma, S. K. Tomar, and A. K. Gupta, “A modified iterative amplitude clipping and filtering technique for PAPR reduction in OFDM systems,” in *Proc. IEEE International Conference on Emerging Trends in Networks and Computer Communications*, Udaipur, India, Apr. 2011, pp. 365-368.

[88] K. Sahu and K. T. Veeramanju, “PAPR reduction in OFDM system using iterative clipping and filtering technique along with convolutional code,” in *Proc. IEEE the fifth International Conference on Communication Systems and Network Technologies*, Gwalior, India, Apr. 2015, pp. 412-415.

[89] Z. Yu, R. J. Baxley, and G. T. Zhou, “Iterative clipping for PAPR reduction in visible light OFDM communications,” in *Proc. IEEE Military Communications Conference*, Baltimore, USA, Oct. 2014, pp. 1681-1686.

[90] Y. C. Wang and Z. Q. Luo, “Optimized iterative clipping and filtering for PAPR reduction of OFDM signals,” *IEEE Trans. Commun*., vol. 59, no. 1, pp. 33–37, Jan. 2011.

[91] X. Zhu, W. Pan, H. Li, and Y. Tang, “Simplified approach to optimized iterative clipping and filtering for PAPR reduction of OFDM signals,” *IEEE Trans. Commun*., vol. 61, no. 5, pp. 1891–1901, May 2013.

[92] E. Udayakumar and P. Vetrivelan, “PAPR reduction for OQAM/OFDM signals using optimized iterative clipping and filtering technique,” in *Proc. IEEE International Conference on Soft-Computing and Networks Security*, Coimbatore, India, Feb. 2015, pp. 1-6.

[93] L. Yao, J. He, X. Xu, “Analysis and comparison of two clipping methods in PAPR reduction for OFDM system,” in *Proc. IEEE International Conference on Biomedical Engineering and Informatics*, Chongqing, China, Oct. 2012, pp. 1435–1438.

[94] N. Dinur and D. Wulich, “Peak to average power ratio in amplitude clipped high order OFDM,” in *Proc. IEEE Military Communication Conference*, Boston, USA, Oct. 1998, pp. 684–687.

[95] ——, "Peak-to-average power ratio in high-order OFDM," *IEEE Trans. Commun*., vol. 49, no. 6, pp. 1063–1072, June 2001.

[96] H. Ochiai and H. Imai, "Performance analysis of deliberately clipped OFDM signals," *IEEE Trans. Commun*., vol. 50, no. 1, pp. 89–101, Jan. 2002.

[97] D. Wulich, N. Dinur, and A. Glinowiecki, "Level clipped high-order OFDM," *IEEE Trans. Commun*., vol. 48, no. 6, pp. 928–930, June 2000.

[98] S. Thompson, J. Proakis, and J. Zeidler, "The effectiveness of signal clipping for PAPR and total degradation reduction in OFDM systems," in *Proc. IEEE Global Telecommunication Conference*, Nov. 2005, pp. 2811-2816.

[99] A. Beck and M. Teboulle, "A fast iterative shrinkage/thresholding algorithm for linear inverse problems," *Society for Indust. and Applied Math. J. Imaging Sci*., vol. 2, no. 1, Jan. 2009.

[100] M. Yamagishi and I. Yamada, "Overrelaxation of the fast iterative shrinkage/thresholding algorithm for fast signal recovery," in *Proc. IEEE Statistical Signal Processing Workshop*, Nice, France, Jun. 2011, pp.697–700.

[101] S. Haykin, *Adaptive Filter Theory 4th edition*. New Jersey, USA: Practice Hall, 2002.

[102] B. F. Boroujeny, *Adaptive Filters: Theory and Applications*. New York, USA: John Wiley & Sons, 2013.

[103] A. H. Sayed, *Adaptive Filters*. New York, USA: John Wiley & Sons, 2008.

[104] S. Sukhumalchayaphong and C. Benjangkaprasert, "Variable forgetting factor RLS algorithm for adaptive echo cancellation," in *Proc. IEEE International Conference on Control, Automation and Systems*, Seoul, South Korea, Oct. 2014, pp. 971–974.

[105] A. Charoenphol, T. Inchan, and C. Benjangkaprasert, "Adaptive forgetting factor RLS algorithm equalizer for DS-CDMA system based on adaptive Laguerre lattice filter," in *Proc. IEEE International Conference on Electrical Engineering/Electronics, Computer, Telecommunications and Information Technology*, Khon Kaen, Thailand, May 2011, pp. 344–347.

[106] A. Charoenphol and C. Benjangkaprasert, "Variable forgetting factor RLS adaptive equalizer for DS-CDMA system," in *Proc. IEEE Symposium on Computers & Informatics*, Kuala Lumpur, Malaysia, Mar. 2011, pp. 167–170.

[107] S. J. Chern and C. H. Sun, "Linearly constrained RLS algorithm with variable forgetting factor for DS-CDMA system," in *Proc. IEEE International Symposium on Intelligent Signal Processing and Communication Systems*, Kuching, Malaysia, Dec. 2014, pp. 261-264.

[108] M. Beza and M. Bongiorno, "Application of recursive least square (RLS) algorithm with variable forgetting factor for frequency components estimation in a generic input signal," in *Proc. IEEE Energy Conversion Congress and Exposition*, Raleigh, USA, Sept. 2012, pp. 2164–2171.

[109] B. Qin, Y. Cai, B. Champagne, M. Zhou, and S. Yousefi, "Low-complexity variable forgetting factor constant modulus RLS-based algorithm for blind adaptive beamforming," in *Proc. IEEE Asilomar Conference on Signals, Systems and Computers*, Pacific Grove, USA, Nov. 2013, pp. 171-175.

[110] H. Chen, Z. Wang, Y. Lu, D. Li, and T. Li, "Cumulant-based RLS algorithm with variable forgetting factor to estimate time-varying interharmonics," in *Proc. IEEE The Fourth International Conference on Instrumentation and Measurement, Computer, Communication and Control*, Harbin, China, Sept. 2014, pp. 351–356.

[111] F. Albu, "Improved variable forgetting factor recursive least square algorithm," in *Proc. IEEE International Conference on Control Automation Robotics & Vision*, Guangzhou, China, Dec. 2012, pp. 1789 – 1793.

[112] K. Sharpe, "Some properties of the crossings process generated by a stationary $\chi$ process," *Advances in Applied Probability*, vol. 10, no. 2, pp. 373–391, June 1978.

[113] M. Aronowich and R. J. Adler, "Extrema and level crossings of $\chi^2$ processes," *Advances in Applied Probability*, vol. 18, no. 4, pp. 901–920, Dec. 1986.

[114] N. M. Blachman, "Gaussian noise – part I: The shape of large excursions," *IEEE Trans. Inform. Theory*, vol. 34, no. 6, pp. 1396–1400, Nov. 1988.

[115] S. O. Rice, "Distribution of the maxima of a random curve," *Amer. J. Math.*, vol. 61, pp. 409–416, 1939.

[116] ——, "Mathematical analysis of random noise," *Bell Syst. Tech. J.*, vol. 23, pp. 282–332, 1944.

[117] ——, "Mathematical analysis of random noise," *Bell Syst. Tech. J.*, vol. 24, pp. 46–156, 1945.

[118] ——, “Statistical properties of a sine wave plus random noise,” *Bell Syst. Tech. J.*, vol. 27, pp. 109–157, 1948.

[119] ——, “Distribution of the duration of fades in radio transmission: Gaussian noise model,” *Bell Syst. Tech. J.*, vol. 37, pp. 581–635, 1958.

[120] R. Price, “A useful theorem for nonlinear devices having Gaussian inputs,” *IEEE Trans. Inform. Theory*, vol. 4, no. 2, pp. 69–72, June 1958.

[121] ——, “Comments on ‘a useful theorem for nonlinear devices having Gaussian inputs’,” *IEEE Trans. Inform. Theory*, vol. 10, no. 2, pp. 171–171, Apr. 1964.

[122] I. Blake and W. Lindsey, “Level-crossing problems for random processes,” *IEEE Trans. Inform. Theory*, vol. 19, no. 3, pp. 295–315, May 1973.

[123] N. M. Blachman, “Gaussian noise – part II: Distribution of phase change of narrow-bandnoise plus sinusoid,” *IEEE Trans. Inform. Theory*, vol. 34, no. 6, pp. 1401–1405, Nov. 1988.

[124] N. Blachman, “Gaussian noise: prediction based on its value and N derivatives,” *IEE Proc. F Radar and Signal Processing*, vol. 140, no. 2, pp. 98–102, Apr. 1993.

[125] J. Mazo, “Asymptotic distortion spectrum of clipped, DC-biased, Gaussian noise [optical communication],” *IEEE Trans. Commun.*, vol. 40, no. 8, pp. 1339–1344, Aug. 1992.

[126] A. Bahai, M. Singh, A. Goldsmith, and B. Saltzberg, “A new approach for evaluating clipping distortion in multicarrier systems,” *IEEE J. Select. Areas Commun.*, vol. 20, no. 5, pp. 1037–1046, June 2002.

[127] A. M. Tulino and S. Verdu, *Random matrix theory and wireless communications*. Boston, USA: Now Publishers Inc., 2004.

[128] Kratos Microwave Electronics Division, Solid State Power Amplifier – Microwave SSPA – General, January 2017. [Online]. Available: http://gmcatalog.kratosmed.com/prodsforfamily/solid-state-power-amplifier-sspa-general

[129] R. Hunger, “Floating point operations in matrix-vector calculus,” Technical University of Munich, Tech. Rep.

[130] M. N. O. Sadiku and C. M. Akujuobi, “Software Defined Radio: A brief overview,” *IEEE Potentials.*, vol.23, no.4, pp. 14-15, Oct. 2000.

[131] NuRAN Wireless, GNU Radio and MIMO SDR: How FPGA Processing Can Reduce Communication Bandwidth Requirements, January 2017. [Online]. Available: https://www.nutaq.com/blog/gnu-radio-and-mimo-sdr-how-fpga-processing-can-reduce-communication-bandwidth-requirements

[132] Ettus Research, USRP B210, January 2017. [Online]. Available: https://www.ettus.com/product/details/UB210-KIT

# Appendix A

This appendix provides the additional methods used for Chapter 6 and Chapter 7. They include Riemann Summ, Taylor's Series Expansion, Chebyshev's Inequality, Cauchy-Schwarz Inequality, Jacobian's Transformation respectively.

## A.1 Riemann Sum

The Riemann Sum formula provides a precise definition of the definite integral as the limit of an infinite series. It can be expressed as

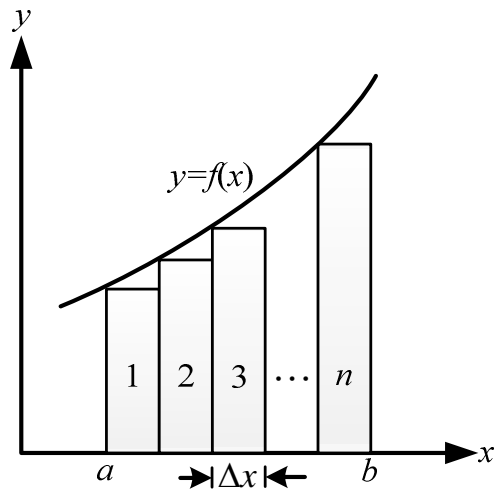


Figure A.1 Riemann Sum.

$$\lim_{n\to\infty}\sum_{i=0}^{n} f[x_i]\Delta x = \int_a^b f(x)\,dx, \tag{A.1}$$

where $\Delta x = \dfrac{b-a}{n}$.

# A.2 Taylor's Series Expansion

*Taylor's Theorem*. If $\tilde{x}$ is a discrete function and $n$ times differentiable in an interval $[k, k+h]$, then there exists some point in this interval, denoted by $k+\Delta h$ for some $\Delta \in [0,1]$, such that

$$\tilde{x}[k+h] = \tilde{x}[k] + h\dot{\tilde{x}}[k] + \frac{h^2}{2}\ddot{\tilde{x}}[k] + \cdots + \frac{h^{(n-1)}}{(n-1)!}\tilde{x}^{(n-1)}[k] + \frac{h^{(n)}}{n!}\tilde{x}^{n}[k+\Delta h]. \quad \text{(A.2)}$$

# A.3 Chebyshev's Inequality

*Chebyshev's Theorem*. If $X$ is a random variable with finite mean $\bar{X}$ and variance $\sigma_X^2$, then, for any $a > 0$,

$$\begin{aligned} Pr\left[\left|X-\bar{X}\right| \geq a\right] &\leq Pr\left[\left(X-\bar{X}\right)^2 \geq a^2\right] \\ &\leq \frac{1}{a^2}E\left[(X-\bar{X})^2\right] \\ &\leq \frac{\sigma_X^2}{a^2}. \end{aligned} \quad \text{(A.3)}$$

# A.4 Cauchy-Schwarz Inequality

*Cauchy-Schwarzs' Theorem*. Let $u$ and $v$ be two vectors in the real number. The Cauchy-Schwartz inequality states that

$$|u \cdot v| \leq |u| \cdot |v|. \quad \text{(A.4)}$$

Written out in coordinates, this says

$$|u_1v_1 + u_2v_2 + \cdots + u_nv_n| \leq \sqrt{u_1^2 + u_2^2 + \cdots + u_n^2}\sqrt{v_1^2 + v_2^2 + \cdots + v_n^2}. \quad \text{(A.5)}$$

# A.5 Jacobian's Transformation

*Jacobian's Theorem*. Since $x = r\cos\theta$ and $y = r\sin\theta$, then the Jacobian's matrix transformation is

$$\Delta J(r,\theta) = \begin{vmatrix} x_r & x_\theta \\ y_r & y_\theta \end{vmatrix} = \begin{vmatrix} \cos\theta & -r\sin\theta \\ \sin\theta & r\cos\theta \end{vmatrix}. \tag{A.6}$$

# Appendix B

## Proofs

## B.1 Discrete Time Independent of Different Clipping Pulses

The signal $\tilde{x}[k]$ can be expressed as a cyclostationary process. Then, from the time $k_p$ to $k_c$, the correlation of $\tilde{x}[k]$ depends only on the difference of the time $\Delta k = k_p - k_c$. Therefore, the correlation of $\tilde{x}[k]$ and $\tilde{x}[k+\Delta k]$ is

$$\begin{aligned} R_{\tilde{x}} &= \frac{E\left[\tilde{x}[k]+\tilde{x}^*[k+\Delta k]\right]}{2} \\ &= \frac{\sum_{i=-\frac{n_c}{2}}^{\frac{n_c}{2}-1}\sum_{l=-\frac{n_c}{2}}^{\frac{n_c}{2}-1} E\left[X_i X_l^*\right] e^{\frac{j2\pi\left(ik_p - l[k+\Delta k]\right)}{T_b}}}{2n_c} \\ &= \sigma_{\tilde{x}}^2 \frac{\sum_{i=-\frac{n_c}{2}}^{\frac{n_c}{2}-1} e^{\frac{j2\pi i\Delta k}{T_b}}}{n_c} \\ &= \sigma_{\tilde{x}}^2 \frac{\sin\left(\frac{\pi n_c \Delta k}{T_b}\right)}{n_c \sin\left(\frac{\pi \Delta k}{T_b}\right)} e^{\frac{-j\pi\Delta k}{T_b}}. \end{aligned} \tag{B.1}$$

Due to

$$\frac{E\left[\tilde{x}[k]\tilde{x}^{*}[k]\right]}{2}=\sigma_{\tilde{x}}^{2}, \tag{B.2}$$

the correlation coefficient of $\tilde{x}[k]$ and $\tilde{x}[k+\Delta k]$ can be also shown as

$$R_{\tilde{x}}[\Delta k]=\frac{\sin\left(\frac{\pi n_c \Delta k}{T_b}\right)}{n_c \sin\left(\frac{\pi \Delta k}{T_b}\right)} e^{-\frac{j\pi\Delta k}{T_b}}. \tag{B.3}$$

When the Nyquist sampling rate $T_b / n_c$ is employed, both $R_{\tilde{x}}[k]=\delta[k]$ and $\tilde{x}[k]$ are independent. Nevertheless, in the time domain, this possibility is small and can be skipped when the clipping pulses fall within a small time interval and have the large correlation. Then, the clipping pulses are appeared at different time instances and can be effectively treated as independent.

Let $\Delta k = cT_b / n_c,$ where $c$ is a real value, and $0 \le c < n_c$. Based on an assumption of a small $c$, and a large $n_c$ (or $c \ll n_c$), then,

$$R_{\tilde{x}}\left[\frac{cT_b}{n_c}\right]=\left|\frac{\sin[c\pi]}{n_c \sin\left(\frac{c\pi}{n_c}\right)}\right|=\left|\frac{\sin[c\pi]}{c\pi}\right|, \quad n_c \to \infty. \tag{B.4}$$

In [112], it shows that the up-crossing time of $\tilde{x}[k]$ is Poisson distributed, when $n_c \to \infty$:

$$\lim_{\beta(\zeta)\to\infty} Pr\left[U_{c,\beta(\zeta)}(0,\Delta k)=c\right]=\frac{\left(\Delta k \lambda_{\beta(\zeta)}\right)^{c} e^{-\Delta k \lambda_{\beta(\zeta)}}}{c!}, \tag{B.5}$$

where $U_{c,\beta(\zeta)}(0,\Delta k)$ is the total number of the up-crossing by a $\chi^2$ process

$$Y[k]=X_1^2[k]+X_2^2[k]+\ldots+X_{n_c}^2[k]. \tag{B.7}$$

From (B.7), the $\chi^2$ process is up-crossed at the variable clipping level $\beta(\zeta)/\sigma > 0$ with $\sigma = E\left[X_c^2[k]\right]$ for all $k$ in the during time interval $(0,\Delta k)$. For a

large $\beta(\zeta)$, each up-crossing of level $\beta(\zeta)$ leads to a parabolic clipping pulse. Then, in the duration $(0,\Delta k)$, the probability that is more than $i$ clipping pulses (or $i \geq 1$) occurs in the same time interval $(0,\Delta k)$. This probability can be shown as

$$\begin{aligned} Pr[i] &= Pr\left[U_{c,\beta(\zeta)}(0,\Delta k) > i \mid \beta(\zeta)\right] \\ &= Pr\left[U_{c,\beta(\zeta)}(0,\Delta k) > i-1\right] \\ &= 1-\sum_{l=0}^{i-1} \frac{\left(\Delta k \lambda_{\beta(\zeta)}\right)^l e^{-\Delta k \lambda_{\beta(\zeta)}}}{l!}. \end{aligned} \tag{B.8}$$

# B.2 The Qualified PDF and Moments of $\gamma_p$

The qualified PDF and moments of $\gamma_p$ from (6.17) are proved in this section, where $\ddot{\tilde{x}}[k_p] \leq 0$, $\dot{\tilde{x}}[k_p] = 0$, and $\tilde{x}[k_p] \geq \beta(\zeta)$. The subscript $p$ and the sampling index $k_p$ are dropped off in this following analysis. However, the probability of $Pr\left[\ddot{\tilde{x}} \mid \dot{\tilde{x}} = 0, \tilde{x} \leq \beta(\zeta)\right]$ unless $\beta(\zeta)$ is very low level will be shown in Appendix B.3.

Given the subscript $R$ and $I$ are symbolised from the real number and the imaginary number respectively, $\dot{\tilde{x}}_R = (\dot{\tilde{x}} + \dot{\tilde{x}}^*)/2$, and $\dot{\tilde{x}}_I = (\dot{\tilde{x}} - \dot{\tilde{x}}^*)/2j$. First, $\tilde{x}_R, \tilde{x}_I, \dot{\tilde{x}}_R$ and $\dot{\tilde{x}}_I$ will be proved to be independent when $n_c$ is large, then

$$\dot{\tilde{x}}[k] = \frac{1}{\sqrt{n_c}} \sum_{c=-\frac{n_c}{2}}^{\frac{n_c}{2}-1} \frac{j2\pi c}{T_b} X_c e^{\frac{j2\pi ck}{T_b}}. \tag{B.9}$$

Then, $\dot{\tilde{x}}_R$ and $\dot{\tilde{x}}_I$ are i.i.d Gaussian distribution with zero mean and variance

$$\dot{\sigma}^2 = \frac{4\pi^2\sigma_{\tilde{x}}^2}{n_c T_b^2} \sum_{c=-\frac{n_c}{2}}^{\frac{n_c}{2}-1} c^2 \approx \frac{(n_c^2+2)\pi^2\sigma_{\tilde{x}}^2}{3T_b^2}, \tag{B.10}$$

where $E\left[X_c X_l\right] = 0$ for any $c$ and $l$. When $n_c$ is large, then

$$\dot{\sigma}^2 \approx \frac{\pi^2 n_c^2 \sigma_{\tilde{x}}^2}{3T_b^2} \approx \frac{\pi^2}{3} BW^2 \sigma_{\tilde{x}}^2. \tag{B.11}$$

By the use of

$$\tilde{x}[k] = \frac{1}{\sqrt{n_c}} \sum_{c=-\frac{n_c}{2}}^{\frac{n_c}{2}-1} X_c e^{j2\pi \frac{ck}{T_b}}, \quad 0 \le k \le T_b,$$

and (B.9), then

$$E\left[\tilde{x}_R \dot{\tilde{x}}_R\right] = E\left[\tilde{x}_I \dot{\tilde{x}}_I\right] = 0. \tag{B.12}$$

On the other side,

$$E\left[\tilde{x}_R \dot{\tilde{x}}_I\right] = -E\left[\tilde{x}_I \dot{\tilde{x}}_R\right] = \frac{2\pi\sigma_{\tilde{x}}^2}{T_b n_c} \sum_{c=-\frac{n_c}{2}}^{\frac{n_c}{2}-1} c \approx -\frac{\pi\sigma_{\tilde{x}}^2}{T_b}, \tag{B.13}$$

and their correlations are

$$R_{\tilde{x}_R, \dot{\tilde{x}}_I} = -R_{\tilde{x}_I, \dot{\tilde{x}}_R} = -\frac{3}{\sqrt{n_c^2 + 2}}. \tag{B.14}$$

In (B.14), it proves that the correlations are zero when $n_c$ is large. Therefore, it also proves that $\tilde{x}_R, \tilde{x}_I, \dot{\tilde{x}}_R$ and $\dot{\tilde{x}}_I$ are independent when $n_c \to \infty$.

Second, the proof that the joint PDF $p\left(\dot{\tilde{x}}_I, \tilde{x}_R, \tilde{x}_I \mid \dot{\tilde{x}} = 0\right)$ is presented as follows. The distribution of both $\dot{\tilde{x}}_R$ and $\dot{\tilde{x}}_I$ cannot be changed by fixing $\tilde{x}_R$ and $\tilde{x}_I$ because all $\tilde{x}_R, \tilde{x}_I, \dot{\tilde{x}}_R$ and $\dot{\tilde{x}}_I$ are independent. Note that

$$\dot{\tilde{x}} = \frac{1}{\tilde{x}}\left(\tilde{x}_R \dot{\tilde{x}}_R + \tilde{x}_I \dot{\tilde{x}}_I\right). \tag{B.15}$$

Given $\dot{\tilde{x}}$ is also i.i.d Gaussian distribution with zero mean and variance

$$\dot{\sigma}_{\dot{\tilde{x}}}^2 = E\left[\dot{\tilde{x}}^2\right] = \dot{\sigma}^2. \tag{B.16}$$

The signal $\dot{\tilde{x}}$ is independent of $\tilde{x}_R, \tilde{x}_I,$ and $\tilde{x}$, and

$$p(\dot{\tilde{x}}) = \frac{1}{\sqrt{2\pi}\dot{\sigma}} e^{-\frac{\dot{\tilde{x}}}{2\dot{\sigma}^2}}, \tag{B.17}$$

then, the correlation between $\dot{\tilde{x}}_I$ and $\dot{\tilde{x}}$ is

$$R_{\dot{\tilde{x}}_I,\dot{\tilde{x}}} = \frac{\tilde{x}_I}{\tilde{x}}, \tag{B.18}$$

afterwards,

$$p\left(\dot{\tilde{x}}_I, \dot{\tilde{x}} \mid \tilde{x}_R, \tilde{x}_I\right) = \frac{\sqrt{\tilde{x}_R^2 + \tilde{x}_I^2}}{2\pi\dot{\sigma}^2 \left|\tilde{x}_R\right|} e^{\left(-\frac{\tilde{x}_R^2+\tilde{x}_I^2}{2\dot{\sigma}^2\tilde{x}_R^2}\left(\dot{\tilde{x}}_I^2 - 2\frac{\tilde{x}_I\dot{\tilde{x}}_I\tilde{x}}{\sqrt{\tilde{x}_R^2+\tilde{x}_I^2}} + \dot{\tilde{x}}^2\right)\right)}, \tag{B.19}$$

and

$$\begin{aligned} p\left(\dot{\tilde{x}}_I, \tilde{x}_R, \tilde{x}_I \mid \dot{\tilde{x}} = 0\right) &= \left.\frac{p\left(\dot{\tilde{x}}_I, \dot{\tilde{x}} \mid \tilde{x}_R, \tilde{x}_I\right) p\left(\tilde{x}_R\right) p\left(\tilde{x}_I\right)}{p\left(\dot{\tilde{x}}\right)}\right|_{\dot{\tilde{x}}=0} \\ &= \frac{\sqrt{\tilde{x}_R^2 + \tilde{x}_I^2}}{\left(2\pi\right)^{\frac{3}{2}} \dot{\sigma}\sigma_{\tilde{x}}^2 \left|\tilde{x}_R\right|} e^{\left(-\frac{\dot{\tilde{x}}_I^2\left(\tilde{x}_R^2+\tilde{x}_I^2\right)}{2\dot{\sigma}^2\tilde{x}_R^2} - \frac{\tilde{x}_R^2+\tilde{x}_I^2}{2\sigma_{\tilde{x}}^2}\right)}. \end{aligned} \tag{B.20}$$

In the case to obtain $p\left(\gamma, \tilde{x}, \theta \mid \dot{\tilde{x}} = 0\right)$, all transformations are used as

$$\dot{\tilde{x}}_I = \tilde{x}\gamma\left|\cos\theta\right| + \dot{\tilde{x}}\sin\theta, \tag{B.21}$$

$$\tilde{x}_R = \tilde{x}\cos\theta, \tag{B.22}$$

$$\tilde{x}_I = \tilde{x}\sin\theta, \tag{B.23}$$

By using Appendix A.5, all $\dot{\tilde{x}}_I, \tilde{x}_R, \tilde{x}_I$ can be replaced to $\gamma, \tilde{x}$, and $\theta$, therefore,

$$\Delta J(\gamma, \tilde{x}, \theta) = \left.\begin{vmatrix} \tilde{x}\cos\theta & \gamma\cos\theta & -\tilde{x}\gamma\sin\theta + \dot{\tilde{x}}\cos\theta \\ 0 & \cos\theta & -\tilde{x}\sin\theta \\ 0 & \sin\theta & \tilde{x}\cos\theta \end{vmatrix}\right|_{\dot{\tilde{x}}=0} = \tilde{x}^2\cos\theta, \tag{B.24}$$

$$\Delta J(\gamma, \tilde{x}, \theta) = \left.\begin{vmatrix} -\tilde{x}\cos\theta & -\gamma\cos\theta & \tilde{x}\gamma\sin\theta + \dot{\tilde{x}}\cos\theta \\ 0 & \cos\theta & -\tilde{x}\sin\theta \\ 0 & \sin\theta & \tilde{x}\cos\theta \end{vmatrix}\right|_{\dot{\tilde{x}}=0} = -\tilde{x}^2\cos\theta, \tag{B.25}$$

for both (B.24) and (B.25), they can be used in the case of $-\pi/2 \le \theta \le \pi/2,$ hence,

$$\Delta J(\gamma, \tilde{x}, \theta) = \tilde{x}^2 \left|\cos\theta\right|, \tag{B.26}$$

then, the Eq. (B.20) can be replaced by the use of (B.26) as

$$\begin{aligned} p\left(\gamma, \tilde{x}, \theta \mid \dot{\tilde{x}} = 0\right) &= p\left(\dot{\tilde{x}}_I, \tilde{x}_R, \tilde{x}_I \mid \dot{\tilde{x}} = 0\right)\left|\Delta J(\gamma, \tilde{x}, \theta)\right| \\ &= \frac{\tilde{x}^2}{(2\pi)^{\frac{3}{2}} \dot{\sigma}\sigma_{\tilde{x}}^2} e^{\left(-\frac{\tilde{x}^2\gamma^2}{2\dot{\sigma}^2} - \frac{\tilde{x}^2}{2\sigma_{\tilde{x}}^2}\right)}. \end{aligned} \tag{B.27}$$

Finally, the PDF of $\gamma$ is depended on the conditions when $\dot{\tilde{x}} = 0$ and $\tilde{x} \ge \beta(\zeta)$. It can be shown as

$$\begin{aligned} p\left(\gamma \mid \dot{\tilde{x}} = 0, \tilde{x} \ge \beta(\zeta)\right) &= \frac{\sum_{\tilde{x}=\beta(\zeta)}^{\infty} \sum_{\theta=0}^{2\pi} p\left(\gamma, \tilde{x}, \theta \mid \dot{\tilde{x}} = 0\right) \Delta\theta \Delta\tilde{x}}{\sum_{\tilde{x}=\beta(\zeta)}^{\infty} p(\tilde{x}) \Delta\tilde{x}} \\ &= \frac{\beta^3(\zeta)}{4\sqrt{2\pi}\dot{\sigma}\sigma_{\tilde{x}}^2 \Phi^3}\left(2\Phi e^{-\Phi^2} + \sqrt{\pi}\,\mathrm{erfc}\left(\Phi\right)\right) e^{\frac{\beta^2(\zeta)}{2\sigma_{\tilde{x}}^2}}, \end{aligned} \tag{B.28}$$

where

$$\Phi = \frac{\beta(\zeta)\sqrt{\gamma^2\sigma_{\tilde{x}}^2 + \dot{\sigma}^2}}{\sqrt{2}\dot{\sigma}\sigma_{\tilde{x}}}. \tag{B.29}$$

However, in the case of the CCDF of $\gamma$, it cannot be expressed in the closed form because $p\left(\gamma \mid \dot{\tilde{x}} = 0, \tilde{x} \ge \beta(\zeta)\right) = p\left(-\gamma \mid \dot{\tilde{x}} = 0, \tilde{x} \ge \beta(\zeta)\right),$ and the condition mean $\overline{\gamma} = E\left[\gamma \mid \dot{\tilde{x}} = 0, \tilde{x} \ge \beta(\zeta)\right] = 0$. Fortunately, in the term of the condition variance, $\sigma_\gamma^2 = E\left[\gamma^2 \mid \dot{\tilde{x}} = 0, \tilde{x} \ge \beta(\zeta)\right]$, it can be expressed by using (B.20).

The $p\left(\dot{\tilde{x}}_I, \tilde{x}_R, \tilde{x}_I \mid \dot{\tilde{x}} = 0\right)$ can be transformed to be $p\left(\dot{\tilde{x}}_I, \tilde{x}, \theta \mid \dot{\tilde{x}} = 0\right)$ by using the Jacobian's transformation when $\Delta J(\gamma, \tilde{x}, \theta) = \tilde{x}.$ Afterwards,

$$\sigma_{\gamma}^{2}=\frac{\sum_{\dot{\tilde{x}}_I=-\infty}^{\infty}\sum_{\tilde{x}=\beta(\zeta)}^{\infty}\sum_{\theta=0}^{2\pi}\frac{\dot{\tilde{x}}_I^{2}}{\tilde{x}^{2}\cos^{2}\theta}\,p\left(\dot{\tilde{x}}_I,\tilde{x},\theta\,|\,\dot{\tilde{x}}=0\right)\Delta\theta\Delta\tilde{x}\Delta\dot{\tilde{x}}_I}{\sum_{\dot{\tilde{x}}_I=-\infty}^{\infty}\sum_{\tilde{x}=\beta(\zeta)}^{\infty}\sum_{\theta=0}^{2\pi}p\left(\dot{\tilde{x}}_I,\tilde{x},\theta\,|\,\dot{\tilde{x}}=0\right)\Delta\theta\Delta\tilde{x}\Delta\dot{\tilde{x}}_I}$$
$$=\frac{\pi^{2}BW^{2}}{6}\left(\sum_{k=0}^{\infty}\frac{e^{-k\left(\frac{\beta_{CP}^{2}(\zeta)}{2\sigma_{\tilde{x}}^{2}}\right)}}{k}\Delta k\right)e^{\frac{\beta_{CP}^{2}(\zeta)}{2\sigma_{\tilde{x}}^{2}}}, \tag{B.30}$$

and,

$$\sigma_{\gamma}^{4}=\frac{\pi^{4}BW^{4}}{12}\left(\left(\sum_{k=0}^{\infty}\frac{e^{-k\left(\frac{\beta_{CP}^{2}(\zeta)}{2\sigma_{\tilde{x}}^{2}}\right)}}{k}\Delta k\right)e^{\frac{\beta_{CP}^{2}(\zeta)}{2\sigma_{\tilde{x}}^{2}}}-\frac{2\sigma_{\tilde{x}}^{2}}{\beta_{CP}^{2}(\zeta)}\right). \tag{B.31}$$

Moreover, the central moments of $|\gamma|$ can also be found by using (B.20). Hence, the mean of the condition of $|\gamma|$ can be expressed as

$$\begin{aligned}\left|\overline{\gamma}\right|&=E\left[\left|\gamma\right|\,|\,\dot{\tilde{x}}=0,\tilde{x}\geq\beta(\zeta)\right]\\&=\frac{\sum_{\dot{\tilde{x}}_I=-\infty}^{\infty}\sum_{\tilde{x}=\beta(\zeta)}^{\infty}\sum_{\theta=0}^{2\pi}\frac{\left|\dot{\tilde{x}}_I\right|}{\tilde{x}\left|\cos\theta\right|}\,p\left(\dot{\tilde{x}}_I,\tilde{x},\theta\,|\,\dot{\tilde{x}}=0\right)\Delta\theta\Delta\tilde{x}\Delta\dot{\tilde{x}}_I}{\sum_{\dot{\tilde{x}}_I=-\infty}^{\infty}\sum_{\tilde{x}=\beta(\zeta)}^{\infty}\sum_{\theta=0}^{2\pi}p\left(\dot{\tilde{x}}_I,\tilde{x},\theta\,|\,\dot{\tilde{x}}=0\right)\Delta\theta\Delta\tilde{x}\Delta\dot{\tilde{x}}_I}\\&=\frac{\pi BW}{\sqrt{3}}\operatorname{erfc}\left(\frac{\beta(\zeta)}{\sqrt{2}\sigma_{\tilde{x}}}\right)e^{\frac{\beta^{2}(\zeta)}{2\sigma_{\tilde{x}}^{2}}},\end{aligned} \tag{B.32}$$

and the conditional variance of $|\gamma|$ can be also shown as

$$\sigma_{|\gamma|}^{2}=\sigma_{\gamma}^{2}-\left|\overline{\gamma}\right|^{2}. \tag{B.33}$$

Both $\left|\overline{\gamma}\right|$ and $\sigma_{|\gamma|}$ are assumed to be zero when $\beta(\zeta)$ is high compared to the large-scale MIMO-OFDM half bandwidth (in rad/sec) $\pi BW$ .

# B.3 The Proof that Both $\ddot{\tilde{x}}[k_p]>0$ and $\dot{\tilde{x}}[k_p]=0$ or $\tilde{x}[k_p]\geq\beta(\zeta)$ When $\beta(\zeta)\to\infty$

The proof of $Pr\left[\ddot{\tilde{x}}[k_p]>0 \mid \dot{\tilde{x}}[k_p]=0, \tilde{x}[k_p]\geq\beta(\zeta)\right]\to 0$ when $\beta(\zeta)\to\infty$ is presented in this section. The discrete index $k_p$ is also dropped for the ease of equation as well as Appendix B.2.

Due to $\ddot{\tilde{x}}_R=(\ddot{\tilde{x}}+\ddot{\tilde{x}}^*)/2$ and $\ddot{\tilde{x}}_I=(\ddot{\tilde{x}}-\ddot{\tilde{x}}^*)/2j$, where

$$\ddot{\tilde{x}}[k]=-\frac{1}{\sqrt{n_c}}\sum_{c=-\frac{n_c}{2}}^{\frac{n_c}{2}-1}\frac{4\pi^2c^2}{T_b^2}X_c e^{\frac{j2\pi ck}{T_b}}, \tag{B.34}$$

where $\ddot{\tilde{x}}_R$ and $\ddot{\tilde{x}}_I$ are i.i.d Gaussian distribution with zero mean and variance

$$\begin{aligned}\ddot{\sigma}^2&=\frac{16\pi^4\sigma_{\tilde{x}}^2}{n_cT_b^4}\sum_{c=-\frac{n_c}{2}}^{\frac{n_c}{2}-1}c^4\approx\frac{\pi^4\sigma_{\tilde{x}}^2}{15T_b^4}(3n_c^4+20n_c^2-8)\\&\approx\frac{n_c^4\pi^4\sigma_{\tilde{x}}^2}{5T_b^4}=\frac{\pi^4}{5}BW^4\sigma_{\tilde{x}}^2.\end{aligned} \tag{B.35}$$

By the use of

$$\tilde{x}[k]=\frac{1}{\sqrt{n_c}}\sum_{c=-\frac{n_c}{2}}^{\frac{n_c}{2}-1}X_c e^{j2\pi\frac{ck}{T_b}},\quad 0\leq k\leq T_b,$$

and (B.34), then

$$\begin{aligned}&E\left[\tilde{x}_R\ddot{\tilde{x}}_I\right]=E\left[\tilde{x}_I\ddot{\tilde{x}}_R\right]=0,\\&E\left[\tilde{x}_R\ddot{\tilde{x}}_R\right]=E\left[\tilde{x}_I\ddot{\tilde{x}}_I\right]=-E\left[\dot{\tilde{x}}_I^2\right]=-\frac{\pi}{3}BW^2\sigma_{\tilde{x}}^2,\end{aligned} \tag{B.36}$$

and, the correlations are

$$R_{\tilde{x}_R,\ddot{\tilde{x}}_R}=-R_{\tilde{x}_I,\ddot{\tilde{x}}_I}=-\frac{\sqrt{5}}{3}. \tag{B.37}$$

Given $\tilde{x}_R, \tilde{x}_I, \ddot{\tilde{x}}_R$, and $\ddot{\tilde{x}}_I$ are i.i.d Gaussian distribution with mean

$$\begin{aligned} E\left[\ddot{\tilde{x}}_R\right] &= -\frac{\pi^2}{3} BW^2 \tilde{x}_R, \\ E\left[\ddot{\tilde{x}}_I\right] &= -\frac{\pi^2}{3} BW^2 \tilde{x}_I, \end{aligned} \tag{B.38}$$

and their variances are $4\ddot{\sigma}^2 / 9$.

Note that $\dot{\tilde{x}}_I = \gamma \left|\tilde{x}_R\right|, \dot{\tilde{x}} = (\tilde{x}_R \dot{\tilde{x}}_R + \tilde{x}_I \dot{\tilde{x}}_I) / \tilde{x} = 0$, then $\dot{\tilde{x}}_R = -(\tilde{x}_I \dot{\tilde{x}}_I) / \tilde{x}_R$, and

$$\ddot{\tilde{x}} = \frac{\dot{\tilde{x}}_R^2 + \dot{\tilde{x}}_I^2 + \tilde{x}_R \ddot{\tilde{x}}_R + \tilde{x}_I \ddot{\tilde{x}}_I}{\tilde{x}} = \frac{\tilde{x}^2 \gamma^2 + \tilde{x}_R \ddot{\tilde{x}}_R + \tilde{x}_I \ddot{\tilde{x}}_I}{\tilde{x}}. \tag{B.39}$$

Then, given $\tilde{x}_R, \tilde{x}_I, \gamma$, and $\dot{\tilde{x}} = 0$, $\ddot{\tilde{x}}$ is i.i.d Gaussian distribution with mean

$$\bar{\ddot{\tilde{x}}} = E\left[\ddot{\tilde{x}} \mid \tilde{x}_R, \tilde{x}_I, \gamma, \dot{\tilde{x}} = 0\right] = \frac{\left(\tilde{x}^2 \gamma^2 - \frac{\pi^2 BW^2 (\tilde{x}_R^2 + \tilde{x}_I^2)}{3}\right)}{\tilde{x}} = \tilde{x}\left(\gamma^2 - \frac{\pi^2 BW^2}{3}\right), \tag{B.40}$$

and its variance is

$$\begin{aligned} \ddot{\sigma}_{\ddot{\tilde{x}}}^2 &= E\left[\ddot{\tilde{x}}^2 \mid \tilde{x}_R, \tilde{x}_I, \gamma, \dot{\tilde{x}} = 0\right] - \bar{\ddot{\tilde{x}}}^2 \\ &= \frac{4\ddot{\sigma}^2}{9} = \frac{4\pi^4 BW^4 \sigma_{\tilde{x}}^2}{45}. \end{aligned} \tag{B.41}$$

Therefore, the variance of $\ddot{\tilde{x}} / \sigma_{\tilde{x}}$ when $\dot{\tilde{x}} = 0$ and $\tilde{x} \geq \beta(\zeta)$ is

$$\frac{\ddot{\sigma}_{\ddot{\tilde{x}}}^2}{\sigma_{\tilde{x}}^2} = \frac{4\pi^4 BW^4}{45}, \tag{B.42}$$

which is a constant number varied in the $BW$ only.

The mean $\bar{\ddot{\tilde{x}}}$ depends on $\tilde{x}$ rather than the individual $\tilde{x}_R$ and $\tilde{x}_I$. Therefore,

$$\begin{aligned} p(\ddot{\tilde{x}} \mid \gamma, \tilde{x}, \dot{\tilde{x}} = 0) &= p(\ddot{\tilde{x}} \mid \gamma, \tilde{x}_R, \tilde{x}_I, \dot{\tilde{x}} = 0) \\ &= \frac{1}{\sqrt{2\pi}\sigma_{\ddot{\tilde{x}}}} e^{\left(-\frac{(\ddot{\tilde{x}} - \bar{\ddot{\tilde{x}}})^2}{2\sigma_{\ddot{\tilde{x}}}^2}\right)}, \end{aligned} \tag{B.43}$$

hence, the qualified mean of $\ddot{\tilde{x}}/\sigma_{\tilde{x}}$ when $\dot{\tilde{x}}=0$ and $\tilde{x}\geq\beta(\zeta)$ can be expressed

$$\overline{\ddot{\tilde{x}}/\sigma_{\tilde{x}}}=E\left[\frac{\ddot{\tilde{x}}}{\sigma_{\tilde{x}}}\,|\,\dot{\tilde{x}}=0,\tilde{x}\geq\beta(\zeta)\right]$$

$$\text{as}\quad=\frac{\sum_{\ddot{\tilde{x}}=-\infty}^{\infty}\sum_{\tilde{x}=\beta(\zeta)}^{\infty}\sum_{\gamma=-\infty}^{\infty}\sum_{\theta=0}^{2\pi}\ddot{\tilde{x}}p(\ddot{\tilde{x}},\gamma,\tilde{x},\theta\,|\,\dot{\tilde{x}}=0)\Delta\theta\Delta\gamma\Delta\tilde{x}\Delta\ddot{\tilde{x}}}{\sigma_{\tilde{x}}\sum_{\tilde{x}=\beta(\zeta)}^{\infty}p(\tilde{x})\Delta\tilde{x}}. \tag{B.44}$$

Nevertheless,

$$\begin{aligned}\sum_{\ddot{\tilde{x}}=-\infty}^{\infty}\ddot{\tilde{x}}p(\ddot{\tilde{x}},\gamma,\tilde{x},\theta\,|\,\dot{\tilde{x}}=0)\Delta\ddot{\tilde{x}}&=\sum_{\ddot{\tilde{x}}=-\infty}^{\infty}\ddot{\tilde{x}}p(\ddot{\tilde{x}}\,|\,\gamma,\tilde{x},\theta,\dot{\tilde{x}}=0)\,p(\gamma,\tilde{x},\theta\,|\,\dot{\tilde{x}}=0)\Delta\ddot{\tilde{x}}\\&=\overline{\ddot{\tilde{x}}}p(\gamma,\tilde{x},\theta\,|\,\dot{\tilde{x}}=0),\end{aligned} \tag{B.45}$$

where $p(\gamma,\tilde{x},\theta\,|\,\dot{\tilde{x}}=0)$ is based on (B.27). Therefore,

$$\begin{aligned}\overline{\ddot{\tilde{x}}/\sigma_{\tilde{x}}}&=\frac{\sum_{\tilde{x}=\beta(\zeta)}^{\infty}\sum_{\gamma=-\infty}^{\infty}\sum_{\theta=0}^{2\pi}\overline{\ddot{\tilde{x}}}p(\gamma,\tilde{x},\theta\,|\,\dot{\tilde{x}}=0)\Delta\theta\Delta\gamma\Delta\tilde{x}}{\sigma_{\tilde{x}}\sum_{\tilde{x}=\beta(\zeta)}^{\infty}p(\tilde{x})\Delta\tilde{x}}\\&=\frac{\sqrt{2\pi}(\sqrt{5}\sigma_{\tilde{x}}\ddot{\sigma}-3\dot{\sigma}^2)\,\mathrm{erfc}\left(\frac{\beta(\zeta)}{\sqrt{2}\sigma_{\tilde{x}}}\right)e^{\frac{\beta^2(\zeta)}{2\sigma_{\tilde{x}}^2}}-2\sqrt{5}\ddot{\sigma}\beta(\zeta)}{6\sigma_{\tilde{x}}^2}\\&=-\frac{\pi^2BW^2\beta(\zeta)}{3\sigma_{\tilde{x}}}.\end{aligned} \tag{B.46}$$

In conclusion, when $\beta(\zeta)$ is very high level, the mean of $\overline{\ddot{\tilde{x}}/\sigma_{\tilde{x}}}$ converges to $-\infty$. Then, the probability $Pr\left[\ddot{\tilde{x}}>0\,|\,\dot{\tilde{x}}=0,\tilde{x}\geq\beta(\zeta)\right]$ is forward to zero. Also furthermore, the large-scale MIMO-OFDM systems are normally large bandwidth. For this reason, when both $\beta(\zeta)$ and $\overline{\ddot{\tilde{x}}/\sigma_{\tilde{x}}}$ are very small, the probability $Pr\left[\ddot{\tilde{x}}>0\,|\,\dot{\tilde{x}}=0,\tilde{x}\geq\beta(\zeta)\right]$ is approximated to be zero distinctly.

# B.4 The Proof that Both $\gamma_p$ and $\tau_p$ are Uncorrelated When $\dot{\tilde{x}}=0$ and $\tilde{x}\geq\beta(\zeta)$

The conditional joint PDF $p(\ddot{\tilde{x}},\gamma,\tilde{x}\,|\,\dot{\tilde{x}}=0)$ is found in this section. By the use of both (B.27) and (B.43), then

$$\begin{aligned} p(\ddot{\tilde{x}},\gamma,\tilde{x}\,|\,\dot{\tilde{x}}=0) &= p(\ddot{\tilde{x}}\,|\,\gamma,\tilde{x},\theta,\dot{\tilde{x}}=0)\,p(\gamma,\tilde{x},\theta\,|\,\dot{\tilde{x}}=0)\,p(\theta) \\ &= \frac{\tilde{x}^2}{2\pi\sigma_{\ddot{\tilde{x}}}\dot{\sigma}\sigma_{\tilde{x}}^2}\,e^{\left(-\frac{(\ddot{\tilde{x}}-\bar{\ddot{\tilde{x}}})^2}{2\sigma_{\ddot{\tilde{x}}}^2}-\frac{\tilde{x}^2\gamma^2}{2\dot{\sigma}^2}-\frac{\tilde{x}^2}{2\sigma_{\tilde{x}}^2}\right)}. \end{aligned} \tag{B.47}$$

Therefore, the conditional joint at the moments of $\tau$ and $\gamma$ can be calculated as

$$E\left[\tau^i\gamma^n\,|\,\dot{\tilde{x}}=0,\tilde{x}\geq\beta(\zeta)\right]=\frac{\sum_{\tilde{x}=\beta(\zeta)}^{\infty}\sum_{\gamma=-\infty}^{\infty}\sum_{\ddot{\tilde{x}}=-\infty}^{0}\tau^i\gamma^n\,p(\ddot{\tilde{x}},\gamma,\tilde{x}\,|\,\dot{\tilde{x}}=0)\Delta\ddot{\tilde{x}}\Delta\gamma\Delta\tilde{x}}{\sum_{\tilde{x}=\beta(\zeta)}^{\infty}p(\tilde{x})\Delta\tilde{x}}, \tag{B.48}$$

where $i$ and $n$ are positive constants. However, the joint PDF $p(\ddot{\tilde{x}},\gamma,\tilde{x}\,|\,\dot{\tilde{x}}=0)$ is symmetric to $\gamma$. Then, both

$$\sum_{\gamma=-\infty}^{\infty}\tau^i\gamma^n\,p(\ddot{\tilde{x}},\gamma,\tilde{x}\,|\,\dot{\tilde{x}}=0)\Delta\gamma\approx 0, \tag{B.49}$$

and

$$E\left[\tau^i\gamma^n\,|\,\dot{\tilde{x}}=0,\tilde{x}\geq\beta(\zeta)\right]=0 \tag{B.50}$$

for every odd of $n$.

Finally, it can prove that $E\left[\tau^i\gamma^n\,|\,\dot{\tilde{x}}=0,\tilde{x}\geq\beta(\zeta)\right]=0$ when $\dot{\tilde{x}}=0$ and $\tilde{x}\geq\beta(\zeta)$ affecting both $\tau$ and $\gamma$ are uncorrelated.

# Appendix C

## Floating Point Operations (FLOPs)

The complexities of the proposed techniques can be represented in the term of the floating point operations (FLOPs) counting number. Typically, it is used to illustrate the complexity of the system in terms of the addition and multiplication operations in signal processing tasks [128]. This section will show the FLOPs of the proposed schemes, which are the CP-LMS, the CP-RLS, the PMP-LMS, and the PMP-RLS. Their transmitted signal $\boldsymbol{x}_{\Omega_{ZF}}$ is used for FLOPs calculation and can be represented as

$$\boldsymbol{x}_{\Omega_{ZF}} = \underbrace{\sqrt{\frac{n_u}{Tr\left(\left(\mathbf{G}_{ZF}\mathbf{G}_{ZF}^{H}\right)^{-1}\right)}}}_{\Omega_{ZF}} \underbrace{\sum_{l=0}^{L-1} \boldsymbol{w}_l \left[\sum_{t=1}^{n_t}\sum_{n=1}^{N_{rep}} \tilde{\boldsymbol{x}}^{t}_{\beta(\zeta),n}[k-l]\right]}_{\sum_{t=1}^{n_t}\tilde{\boldsymbol{x}}^{t}_{\beta(\zeta),n}[k]}, \tag{C.1}$$

where $\Omega_{ZF}$ is a normalization factor and is a scalar value.

The difference of the proposed schemes and the conventional PAPR reductions is the summation term in (C.1). In the case of the conventional PAPR reductions, a FLOPs conversion table from [128] is used for the FLOPs counting as

$$\sum_{t=1}^{n_t}\tilde{\boldsymbol{x}}^{t}_{\beta(\zeta),n}[k] = n_c n_s n_t n_u. \tag{C.2}$$

On the other hand, the proposed schemes, the Eq. (C.1) can also be factored into three terms that are a scalar $\sqrt{n_u / Tr((\mathbf{G}_{ZF}\mathbf{G}_{ZF}^{H})^{-1})}$ , a matrix $\sum_{l=0}^{L-1}\boldsymbol{w}_l[\cdot] \in \mathbb{C}^{L\times n_t}$ , and a matrix $\sum_{t=1}^{n_t}\sum_{n=1}^{N_{rep}}\tilde{\boldsymbol{x}}^{t}_{\beta(\zeta),n}[k-l]$. They can be totally calculated as the FLOPs counting as

$$\sqrt{\frac{n_u}{Tr\left(\left(\mathbf{G}_{ZF}\mathbf{G}_{ZF}^{H}\right)^{-1}\right)}}\sum_{l=0}^{L-1}\boldsymbol{w}_l\left[\sum_{t=1}^{n_t}\sum_{n=1}^{N_{rep}}\tilde{\boldsymbol{x}}_{\beta(\zeta),n}^{t}[k-l]\right]=(2n_t-1)(LN_{rep}n_cn_s)^2. \quad \text{(C.3)}$$

In the term of the conventional clipping scheme, it can be calculated as the FLOPs counting as

$$\left|\tilde{x}_{\beta_{CP}}(t)\right|=\begin{cases}\left|\tilde{x}(t)\right|, & \text{if } \left|\tilde{x}(t)\right|<\beta\\ \beta, & \text{if } \left|\tilde{x}(t)\right|\geq\beta\end{cases}=n_cn_sn_tn_u. \quad \text{(C.4)}$$

Moreover, according to Algorithm 2 in chapter 4 [21], the PMP can be represented as the FLOPs number as

$$\boldsymbol{y}[k]-\frac{2}{\mathcal{L}}\mathbf{H}^{H}(\mathbf{H}\boldsymbol{y}[k]-\hat{\boldsymbol{s}})=\left(2n_u-1\right)\left(2n_t-1\right)n_un_t^2, \quad \text{(C.5)}$$

and

$$\boldsymbol{x}[k]+\frac{t[k]-1}{t[k+1]}(\boldsymbol{x}[k]-\boldsymbol{x}[k\text{-}1])=n_cn_sn_tn_u. \quad \text{(C.6)}$$

Therefore, from (C.2), (C.4), (C.5), and (C.6), the entire complexity of the clipping scheme is $(n_cn_sn_tn_u)^2$ and the PMP is $(Z_{PMP}n_t)(n_tn_u(2n_u-1)(2n_t-1)+n_cn_s)$. As a result, the adjustable PAPR clipping levels of both the clipping and the PMP are $(n_cn_sn_tn_u)^3$ and $(Z_{PMP}n_t)(n_tn_u(2n_u-1)(2n_t-1)+n_cn_s)(n_cn_sn_tn_u)$ respectively.

In the case of the adaptive algorithms, they can be shown as the FLOPs counting as

$$w[k+1]=w[k]\text{-}\,\mu e[k]^*\tilde{x}_{\beta(\zeta)}[k]=2n_cn_sn_tn_u-1, \quad \text{(C.7)}$$

$$\left.\begin{aligned}w[k+1]&=w[k]+\mu[k]e[k]^*\tilde{x}_{\beta(\zeta)}[k],\\ \mu[k+1]&=\delta\mu[k]+\rho\varphi^2[k],\\ \varphi[k+1]&=\xi\varphi[k]+\upsilon[1-\zeta],\end{aligned}\right\}=(n_un_sn_cn_t)(2n_un_sn_cn_t-1), \quad \text{(C.8)}$$

$$k[k]=\frac{\Theta[k\text{-}1]\tilde{x}_{\beta(\zeta)}[k]}{\chi+\tilde{x}_{\beta(\zeta)}[k]\Theta[k\text{-}1]\tilde{x}_{\beta(\zeta)}[k]}=3n_cn_sn_tn_u-1, \quad \text{(C.9)}$$

and

$$\left.\begin{aligned} k[k] &= \frac{\Theta[k\text{-}1]\tilde{x}_{\beta(\zeta)}[k]}{\chi[k]+\tilde{x}_{\beta(\zeta)}[k]\Theta[k\text{-}1]\tilde{x}_{\beta(\zeta)}[k]}, \\ \operatorname{sign}\left[z[k]\right] &= \operatorname{sign}\left[e[k]e[k-1]\right]\cdot\operatorname{sign}\left[\tilde{x}_{\beta(\zeta)}[k]k[k-1]\right], \end{aligned}\right\} \quad (C.10)$$
$$= (3n_c n_s n_t n_u - 1)(2n_c n_s n_t n_u - 1)(n_c n_s n_t n_u),$$

for the FS-LMS, the VS-LMS, the FFF-RLS, and the VFF-RLS respectively.

Finally, the proposed schemes can be totally presented as the FLOPs counting as the Table C.1.

**Table C.1** The FLOPs counting of each scheme.

| **Methods** | **FLOPs counting** |
|---|---|
| FCL-CP-FS-LMS | $(2n_t-1)(n_c n_s n_t n_u)(2n_c n_s n_t n_u-1)(LN_{rep}n_c n_s n_u)^2$ |
| ACL-CP-VS-LMS | $(2n_t-1)(2n_c n_s n_t n_u-1)(LN_{rep})^2(n_c n_s)^2(n_t n_u n_c n_s)^4$ |
| FCL-CP-FFF-RLS | $(2n_t-1)(3n_c n_s n_t n_u-1)(n_c n_s n_t n_u)^2(LN_{rep}n_c n_s)^2$ |
| ACL-CP-VFF-RLS | $(2n_t-1)(LN_{rep}n_c n_s)^2(3n_c n_s n_t n_u-1+n_c n_s n_t n_u(2n_c n_s n_t n_u-1))$ $(n_c n_s n_t n_u)^3$ |
| FCL-PMP-FS-LMS | $(2n_c n_s n_t n_u-1)(Z_{PMP}n_t n_u)(2n_t-1)(n_t(2n_u-1)(2n_t-1)+n_c n_s)$ $(LN_{rep}n_c n_s n_u)^2$ |
| ACL-PMP-VS-LMS | $\left(n_t\left(2n_u-1\right)\left(2n_t-1\right)+n_c n_s\right)\left(2n_c n_s n_t n_u-1\right)\left(Z_{PMP}n_t^2 n_u^2 n_c n_s\right)$ $\left(2n_t-1\right)\left(LN_{rep}n_c n_s n_u\right)^2$ |
| FCL-PMP-FFF-RLS | $(2n_t-1)(LN_{rep}n_c n_s)^2(n_t n_u(2n_u-1)(2n_t-1)+n_c n_s)(Z_{PMP}n_t)$ $(3n_c n_s n_t n_u-1)$ |
| ACL-PMP-VFF-RLS | $\left(2n_t-1\right)\left(LKn_c n_s\right)^2\left(n_c n_s n_t n_u\right)\left(n_t n_u\left(2n_u-1\right)\left(2n_t-1\right)+n_c n_s\right)$ $\left(Zn_t\right)\left(3n_c n_s n_t n_u-1+n_c n_s n_t n_u\left(2n_c n_s n_t n_u-1\right)\right)$ |

# Appendix D

## Algorithms

**Algorithm 1** The process of the adjustable PAPR level for clipping scheme with $N_{qt} = 10$.

1: **initialize** $\tilde{\boldsymbol{x}}_{vec} \leftarrow [real(\tilde{\boldsymbol{x}}); imaginary(\tilde{\boldsymbol{x}})]$, $K \leftarrow length(\tilde{\boldsymbol{x}}_{vec})$, $N_{qt} \leftarrow 10$,

$$i \leftarrow 0:1:N_{qt}-1,\ \tilde{x}_{\beta_{\min}} \leftarrow \frac{\alpha \cdot \beta_{\min}}{100},\ \tilde{x}_{\beta_{\max}} \leftarrow \frac{\alpha \cdot \beta_{\max}}{100},\ j \leftarrow 1:-0.1:0.$$

% Adjustable PAPR level process

2: $\Delta q \leftarrow \dfrac{\tilde{x}_{\beta_{\max}} - \tilde{x}_{\beta_{\min}}}{N_{qt}}$

3: **for** $q = 1,\ldots,\ N_{qt}$ **do**

4: **if** $\zeta \geq j[q]$ **do**

5: $\beta_{qt} \leftarrow \tilde{x}_{\beta_{\max}} - i[q]\Delta q$

6: **else**

7: $\beta_{qt} \leftarrow \tilde{x}_{\beta_{\min}}$

8: **end if**

9: **end for**

10: $\beta_{CP}(\zeta) \leftarrow \beta_{qt}$

% Clipping process

11: **for** $k = 1,\ldots,\ K$ **do**

12: **if** $\left|\tilde{\boldsymbol{x}}_{vec}[k]\right| > \beta_{CP}(\zeta)$ **do**

13: $\tilde{\boldsymbol{x}}_{\beta(\zeta)_{CP}}[k] \leftarrow \beta_{CP}(\zeta) \times sign[\tilde{\boldsymbol{x}}_{vec}[k]]$

14: **else**

15: $\tilde{\boldsymbol{x}}_{\beta(\zeta)_{CP}}[k] \leftarrow \tilde{\boldsymbol{x}}_{vec}[k]$

16: **end if**

17: **end for**

**Algorithm 2** The conventional clipping level for the FITRA algorithm [21].

1: **initialize** $\boldsymbol{x}[0] \leftarrow \mathbf{0}_{n_t \times 1}$, $\boldsymbol{y}[1] \leftarrow \boldsymbol{x}_0, t[1] \leftarrow 1, \mathcal{L} \leftarrow 2\sigma^2_{\max}(\mathbf{H})$

2: **for** $k = 1, 2, \ldots, Z_{PMP}$ **do**

3: $\quad \boldsymbol{b} \leftarrow \boldsymbol{y}[k] - \frac{2}{\mathcal{L}} \mathbf{H}^H (\mathbf{H}\boldsymbol{y}[k] - \hat{\boldsymbol{s}})$

4: $\quad \alpha \leftarrow \arg\min_{\tilde{\alpha}} \left\{ \lambda_{PMP} \tilde{\alpha} + \frac{\mathcal{L}}{2} \sum_{i=1}^{N} ([\,|\,[\boldsymbol{b}]_i\,| - \tilde{\alpha}]^+)^2 \right\}$

5: $\quad \boldsymbol{x}[k] \leftarrow trunc_{\alpha}(\boldsymbol{b})$

6: $\quad t[k+1] \leftarrow \frac{1}{2}(1 + \sqrt{1 + 4t[k]^2}$

7: $\quad \boldsymbol{y}[k+1] \leftarrow \boldsymbol{x}[k] + \frac{t[k]-1}{t[k+1]} (\boldsymbol{x}[k] - \boldsymbol{x}[k-1])$

9: **end for**

10: **return** $\boldsymbol{x}[Z_{PMP}]$

**Algorithm 3** The variable clipping level for the FITRA algorithm.

1: **initialize** $\boldsymbol{x}[0] \leftarrow \mathbf{0}_{n_t \times 1}$, $\boldsymbol{y}[1] \leftarrow \boldsymbol{x}_0, t[1] \leftarrow 1, \mathcal{L} \leftarrow 2\sigma^2_{\max}(\mathbf{H}), \zeta[0] \leftarrow 1$

2: **for** $k = 1, 2, \ldots, Z_{PMP}$ **do**

3: $\quad \boldsymbol{b} \leftarrow \boldsymbol{y}[k] - \frac{2}{\mathcal{L}} \mathbf{H}^H (\mathbf{H}\boldsymbol{y}[k] - \hat{\boldsymbol{s}})$

4: $\quad \beta(\zeta) \leftarrow \arg\min_{\tilde{\alpha}} \left\{ \lambda(\zeta)_{PMP} \tilde{\alpha} + \frac{\mathcal{L}}{2} \sum_{i=1}^{N} ([\,|\,[\boldsymbol{b}]_i\,| - \tilde{\alpha}]^+)^2 \right\}$

5: $\quad \boldsymbol{x}[k] \leftarrow trunc_{\beta(\zeta)}(\boldsymbol{b})$

6: $\quad t[k+1] \leftarrow \frac{1}{2}(1 + \sqrt{1 + 4t[k]^2}$

7: $\quad \boldsymbol{y}[k+1] \leftarrow \boldsymbol{x}[k] + \frac{t[k]-1}{t[k+1]} (\boldsymbol{x}[k] - \boldsymbol{x}[k-1])$

9: **end for**

10: **return** $\boldsymbol{x}[Z_{PMP}]$

**Algorithm 4** The LMS optimisation process.

1: **initialize** $L \leftarrow 5,\ w_l[0] \leftarrow 0,\ \mu \leftarrow 0.9,\ \mu[0] \leftarrow 0,\ \varphi[0] \leftarrow 1,\ e[0] \leftarrow 1,\ \zeta[0] \leftarrow 1,$

$\delta \leftarrow 0.999,\ M \leftarrow N_{rep} \cdot n_c \cdot n_s,\ \rho \leftarrow 0.001,\ \xi \leftarrow 0.999,\ \upsilon = 0.00001,$

$J(w^o) \leftarrow [0,\cdots,1]$

2: **concatenate**

$\tilde{\boldsymbol{x}}_n \leftarrow [\tilde{x}_1, \tilde{x}_2, \cdots, \tilde{x}_{N_{rep}}];\ \tilde{\boldsymbol{x}}_{\beta(\zeta),n} \leftarrow [\tilde{x}_{\beta(\zeta),1}, \tilde{x}_{\beta(\zeta),2}, \cdots, \tilde{x}_{\beta(\zeta),N_{rep}}];$

3: **while** $J\left(w^o\right) \le J\left(w\right)$ **do**

4: **for** $k = 0,1,\cdots,M$ -1 **do**

5: $\boldsymbol{r}[k] \leftarrow \sum_{l=0}^{L-1} w_l[k]\tilde{\boldsymbol{x}}_{\beta(\zeta),n}[k]$

6: $\boldsymbol{e}[k] = \tilde{\boldsymbol{x}}_n[k] - \boldsymbol{r}[k]$

7: **case** FS-LMS

8: $\sum_{l=0}^{L-1} w_l[k+1] \leftarrow \sum_{l=0}^{L-1} w_l[k] + \mu \boldsymbol{e}[k] * \tilde{\boldsymbol{x}}_{\beta(\zeta),n}[k]$

9: **case** VS-LMS

10: $\sum_{l=0}^{L-1} w_l[k+1] \leftarrow \sum_{l=0}^{L-1} w_l[k] + \mu[k]\boldsymbol{e}[k] * \tilde{\boldsymbol{x}}_{\beta(\zeta),n}[k]$

11: $\mu[k+1] \leftarrow \delta\mu[k] + \rho\varphi^2[k]$

12: $\varphi[k+1] \leftarrow \xi\varphi[k] + \upsilon(1-\zeta)$

13: **end case**

14: **end for**

15: **end while**

16: $x_{optz} \leftarrow \boldsymbol{r}$

17: **return** $x_{optz}$

**Algorithm 5** The RLS optimisation process.

1: **initialize** $L \leftarrow 5,\ w_l[0] \leftarrow 0,\ \chi[0] \leftarrow 1,\ e[0] \leftarrow 1,\ \varphi[0] \leftarrow 1,\ \zeta[0] \leftarrow 1,\ \Theta[0] \leftarrow \delta^{-1}\mathbf{I}_{L\times L},$

$\delta \leftarrow 0.004,\ \xi \leftarrow 0.999,\ \vartheta \leftarrow 0.00001,\ \varpi \leftarrow 0.001,\ \rho \leftarrow 0.9996,$

$M \leftarrow N_{rep} \cdot n_c \cdot n_s,\ J(w^o) \leftarrow [0,\cdots,1]$

2: **concatenate**

$\tilde{\boldsymbol{x}}_n \leftarrow [\tilde{x}_1, \tilde{x}_2, \cdots, \tilde{x}_{N_{rep}}];\ \tilde{\boldsymbol{x}}_{\beta(\zeta),n} \leftarrow [\tilde{x}_{\beta(\zeta),1}, \tilde{x}_{\beta(\zeta),2}, \cdots, \tilde{x}_{\beta(\zeta),N_{rep}}];$

3: **while** $J\left(w^{o}\right) \le J\left(w\right)$ **do**

4: **for** $k = 1,2,\ldots,M$ **do**

5: **case** FFF-RLS

6: $k[k] \leftarrow \dfrac{\Theta[k-1]\tilde{\boldsymbol{x}}_{\beta(\zeta),n}[k]}{\chi + \tilde{\boldsymbol{x}}_{\beta(\zeta),n}[k]\Theta[k-1]\tilde{\boldsymbol{x}}_{\beta(\zeta),n}[k]}$

7: $\boldsymbol{r}[k] \leftarrow \sum_{l=0}^{L-1} w_l[k]\tilde{\boldsymbol{x}}_{\beta(\zeta),n}[k]$

8: $\boldsymbol{e}[k] \leftarrow \tilde{\boldsymbol{x}}_n[k] - \boldsymbol{r}[k]$

9: $\sum_{l=0}^{L-1} w_l[k] \leftarrow \sum_{l=0}^{L-1} w_l[k-1] + k[k]\boldsymbol{e}[k]^{*}$

10: $\varphi[k] \leftarrow \xi\varphi[k-1] + \vartheta(1-\zeta)$

11: $\Theta[k] \leftarrow \dfrac{\varpi\varphi^{2}[k\text{-}1]}{\chi}\left(\Theta[k-1] - k[k]\tilde{\boldsymbol{x}}_n[k]\Theta[k-1]\right)$

12: **case** VFF-RLS

13: $k[k] \leftarrow \dfrac{\Theta[k-1]\tilde{\boldsymbol{x}}_{\beta(\zeta),n}[k]}{\chi[k] + \tilde{\boldsymbol{x}}_{\beta(\zeta),n}[k]\Theta[k-1]\tilde{\boldsymbol{x}}_{\beta(\zeta),n}[k]}$

14: $\boldsymbol{r}[k] \leftarrow \sum_{l=0}^{L-1} w_l[k]\tilde{\boldsymbol{x}}_{\beta(\zeta),n}[k]$

15: $\boldsymbol{e}[k] \leftarrow \tilde{\boldsymbol{x}}_n[k] - \boldsymbol{r}[k]$

16: $\sum_{l=0}^{L-1} w_l[k] \leftarrow \sum_{l=0}^{L-1} w_l[k-1] + k[k]\boldsymbol{e}[k]^{*}$

17: $\varphi[k] \leftarrow \xi\varphi[k-1] + \vartheta(1-\zeta)$

18: $\operatorname{sign}\left[z[k]\right] \leftarrow \operatorname{sign}\left[\boldsymbol{e}[k]\boldsymbol{e}[k-1]\right] \cdot \operatorname{sign}\left[\tilde{\boldsymbol{x}}_{\beta(\zeta),n}[k]k[k-1]\right]$

19: $\psi[k] \leftarrow \left(1 + \rho\operatorname{sign}\left[z[k]\right]\right)\left(1 - \chi[k\text{-}1]\right)$

20: $\chi[k] \leftarrow 1 - \psi[k]$

21: $\Theta[k] \leftarrow \dfrac{\varpi\varphi^{2}[k-1]}{\chi[k]}\left(\Theta[k-1] - k[k]\tilde{\boldsymbol{x}}_n[k]\Theta[k-1]\right)$

22: **end case**

23: **end for**

24: **end while**

25: $x_{optz} \leftarrow \boldsymbol{r}$

26: **return** $x_{optz}$

# Publications

# Notification of Acceptance

# ICWCNT2016

On behalf of program committee of ICWCNT2016, we're pleased to inform you that your paper entitled:

Paper Title: The Adaptive PAPR optimizer for PAPR Clipping in MIMO-OFDM systems

Author(s): T. Udomsripaiboon, J. Billingsley, and A. Maxwell

Paper ID: NT0148

was accepted and will be published in the conference proceeding of:

**2016 International Conference on Wireless Communications and Network Technology**

***Guangzhou, China***

***June 24th ~ June 26th, 2016***

which will be published by World Scientific Publishing Company, and submitted to EI and CPCI database for indexing by the publisher.


**ICWCNT2016 Committee**

# The Adaptive PAPR optimizer for PAPR Clipping in MIMO-OFDM systems

T. Udomsripaiboon†, J. Billingsley, and A. Maxwell

*School of Mechanical and Electrical Engineering, University of Southern Queensland, Toowoomba, QLD 4350, Australia*

†*E-mail: thana.udomsripaiboon@usq.edu.au*

*www.usq.edu.au*

This article presents a novel tool to support a peak-to-average power ratio (PAPR) clipping method. It is applicable to multi-input multi-output systems that have large scale antennas and use orthogonal frequency division multiplexing. An adaptive PAPR optimizer is presented, based on a Recursive Least Squares algorithm with the novel addition of a 'variable forgetting factor'. This is controlled by the average bit error rate from all terminals. The task of the adaptive PAPR optimizer is to process the appropriate clipping of signals before sending to at each antenna. The simulation results show that the proposed method achieves a better overall system performance than that of conventional PAPR clipping in terms of the symbol error rate for large-scale multiuser MIMO-OFDM systems.

*Keywords*: PAPR reductions; large-scale MIMO-OFDM; RLS algorithm; PAPR clipping scheme; adaptive PAPR optimizer.

## 1. Introduction

One of the major disadvantages of orthogonal frequency division multiplexing (OFDM) systems is a high peak-to-average-power-ratio (PAPR) caused by the inverse discrete Fourier transform (IDFT) at the transmitter. It causes power amplifiers (PA) to have a nonlinear response for high dynamic- range input levels causing distortions in transmitted signal. The system therefore requires that the linear PAs that are installed with each transmitting antenna must have a high dynamic range, in order to avoid in-band distortion and out-of-band components resulting from any non-linearity and signal clipping. Linear PAs are very expensive and normally have a lower power efficiency than their non-linear counterparts. Increasing the number of antennas increases the seriousness of the problem, especially in the case of the large scale use of antennas in multiple-input multiple-output (MIMO) systems [1].

2

This paper presents a novel tool to support the clipping technique. It is named 'adaptive PAPR optimizer' (APO), with symbol $\Gamma[\bullet]$. The tool is a combination of the adaptive Recursive Least Squares (RLS) equalizer and the PAPR clipping method. It optimizes the output signals resulting from the high peak signal level, $\alpha$, and the clipped signal level, $\beta$, before sending them to each antenna in the MIMO transmission. From the results of simulation, the adaptive PAPR optimizer is shown to improve the overall SER performance in large scale MIMO-OFDM downlink systems more effectively than the conventional PAPR clipping scheme.

## 2. System Model

We consider a large-scale multiuser MIMO-OFDM system downlink channel as presented in Fig.1. A single receiver antenna ($n_r$ = 1) is individually installed in each user terminal $n_u$. Also, the transmitter is equipped with total number of antennas $n_t >> n_u$. A received signal matrix $\mathbf{y} = \left[\boldsymbol{y}_1, \boldsymbol{y}_2, \cdots, \boldsymbol{y}_{n_u}\right]^T$ is composed of the received signal vectors for all terminals and can be expressed as being derived from the transmitted signal $\mathbf{x}_\Omega$ by

$$\mathbf{y} = \sqrt{\gamma_0}\mathbf{H}\mathbf{x}_\Omega + \mathbf{n} \tag{1}$$

where $\gamma_0$ is the signal-to-noise-plus-distortion ratio. The channel gain with flat Rayleigh distribution whose entries follow $\mathcal{CN}(0,1)$ is presented as $\mathbf{H} \in \mathbb{C}^{n_u \times n_t}$, where $\mathbf{n} = \left[\boldsymbol{n}_1, \boldsymbol{n}_2, \cdots, \boldsymbol{n}_{n_u}\right]^T$ is independent and identically distributed (i.i.d) circularly symmetric additive complex Gaussian noise (AWGN) with zero mean and variance $\sigma^2$.

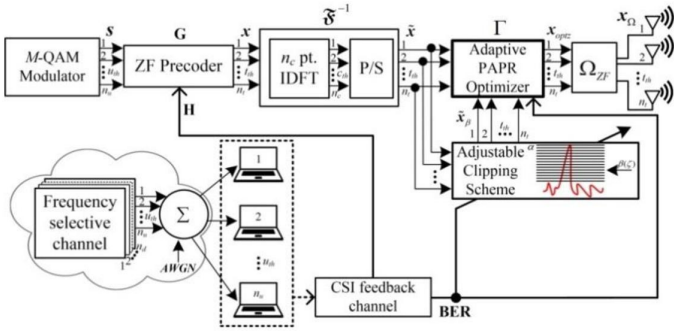


Fig. 1: System model of large-scale MIMO-OFDM downlink with the APO for PAPR clipping.

## 3. Adaptive PAPR Optimizer

An adaptive PAPR optimizer has been inspired by Armstrong [2]. It combines the functionality of a PAPR reduction and a digital filter. The APO optimizes the difference between low and high amplitude dynamic signals, $\tilde{\mathbf{x}}_{\beta}$ and $\tilde{\mathbf{x}}$. The optimized signals are not only at the same level as those of low dynamic range but they also retain the signal shape of the original (i.e. high dynamic range).

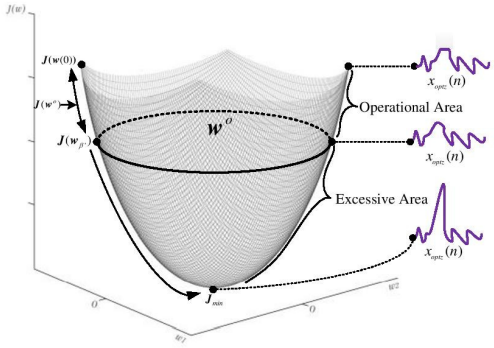


Fig.2 Operational area of the adaptive PAPR optimizer.

Fig. 2 shows both the operational area and the excessive area of an adaptive filter in a typical plot of the cost function of weight vectors, $J(\boldsymbol{w})$, for the case in which the weight vector, $\boldsymbol{w}$, is two-dimensional. For the case of APO, the optimum weight vector, $\boldsymbol{w}^o$, is around the operational area that varies from $J(\boldsymbol{w}(0))$ to $J(\boldsymbol{w}_{\beta'})$. A threshold value is defined with $J(\boldsymbol{w}^o)$ in order to limit the operation of the APO to lie between $J(\boldsymbol{w}(0))$ and $J(\boldsymbol{w}_{\beta'})$. For the $J(\boldsymbol{w}(0))$, the output $x_{optz}(n)$ is the same as the clipped signal $\tilde{x}_{\beta}(n)$ and for the $J(\boldsymbol{w}_{\beta'})$, the output $x_{optz}(n)$ is the desired signal for sending to an antenna. If the APO were to operate in the excessive area from $J(\boldsymbol{w}_{\beta'})$ to $J_{min}$, the high dynamic range of $x_{optz}(n)$, it would increase the average power required of the power amplifiers at the transmitter.

### 3.1. *Variable Forgetting Factor Recursive Least Squares Algorithm*

The novel variable-forgetting-factor (VFF) RLS algorithm for the APO is developed from the fixed-forgetting-factor (FFF) RLS algorithm in [3]. Starting with the Kalman gain of the VFF-RLS algorithm as

4

$$k(n) = \frac{\Phi(n\text{-}1)\tilde{x}_{\beta}(n)}{\chi(n) + \tilde{x}_{\beta}(n)\Phi(n\text{-}1)\tilde{x}_{\beta}(n)}, \tag{2}$$

where the variable forgetting factor is symbolized by $\chi(n)$, $\Phi(n)$ is the inverse correlation matrix of the input signal and the initial value of $\Phi(0)$ is $\delta^{-1}\mathbf{I}_{L\times L}$, where $\delta$ is small positive constant.

The value of $\Phi(n)$ is controlled by the average bit error rate (BER) from all terminals in the wireless local area network (WLAN) cell, $\zeta$, through channel state information (CSI) channel [4-5]. The average BER can be used for controlling the gain of $\chi(n)$ by means of

$$\varphi(n) = \xi\varphi(n\text{-}1) + \vartheta(1\text{-}\zeta), \tag{3}$$

where $\xi$ is a forward gain and $\vartheta$ is a backward gain.

The updated inverse correlation matrix for the VFF-RLS algorithm can be described as follows

$$\text{sign}[z(n)] = \text{sign}[e(n)e(n\text{-}1)] \cdot \text{sign}[\tilde{x}_{\beta}(n)k(n\text{-}1)], \tag{4}$$

$$\psi(n) = \big(1 + \rho\,\text{sign}[z(n)]\big)\big(1 - \chi(n-1)\big), \tag{5}$$

$$\chi(n) = 1 - \psi(n), \tag{6}$$

$$\Phi(n) = \frac{\varpi}{\varphi^2(n\text{-}1)\chi(n)}\big(\Phi(n-1) - k(n)\tilde{x}(n)\Phi(n-1)\big), \tag{7}$$

where $\text{sign}[\cdot]$ is the signum function; $\rho$ and $\varpi$ are the positive values that are in the range of 0 to 1.

The finite impulse response (FIR) is utilized as the main structure of the APO. Finally, the optimized vector, $\boldsymbol{x}_{optz}$, is represented in term of the clipped signal vector, $\tilde{\boldsymbol{x}}_{\beta}$, as

$$\boldsymbol{x}_{optz} = \sum_{l=0}^{L-1} \boldsymbol{w}_l \tilde{\boldsymbol{x}}_{\beta}(n-l), \tag{8}$$

where *L* denotes an adaptive PAPR optimizer length.

### 3.2. *Adjustable Clipping Scheme*

The simplest method to reducing a large PAPR in the OFDM signals, $\tilde{\boldsymbol{x}}$ , is clipping PAPR reduction [2]. It clips the high amplitude peaks in the frequency domain. For the conventional clipping method, the clipping process is defined as

$$\tilde{\boldsymbol{x}}_{\beta} = \begin{cases} \tilde{\boldsymbol{x}} & \text{if } |\tilde{\boldsymbol{x}}| < \beta \\ \beta & \text{if } |\tilde{\boldsymbol{x}}| \geq \beta \end{cases} . \tag{9}$$

By modifying (9) to scale the level of $\beta$ by using $\zeta$ as

$$\beta(\zeta) = \kappa\zeta\alpha, \tag{10}$$

where $\kappa$ is a scaling factor of $\zeta$ ,the clipped signal in (9) can be rewritten as

$$\tilde{\boldsymbol{x}}_{\beta(\zeta)} = \begin{cases} \tilde{\boldsymbol{x}} & \text{if } |\tilde{\boldsymbol{x}}| < \kappa\zeta\alpha \\ \kappa\zeta\alpha & \text{if } |\tilde{\boldsymbol{x}}| \geq \kappa\zeta\alpha \end{cases}, \tag{11}$$

## 4. Simulation Results

One thousand packets consisting of 216 bits per packet were sent. The channel taps were set to $n_d$ = 4, $n_u$ = 10, $n_t$ = 100, a number of OFDM subcarriers $n_c$ = 128, Also, we utilized a 16-QAM constellation to map the coded bits at the WLAN base station.

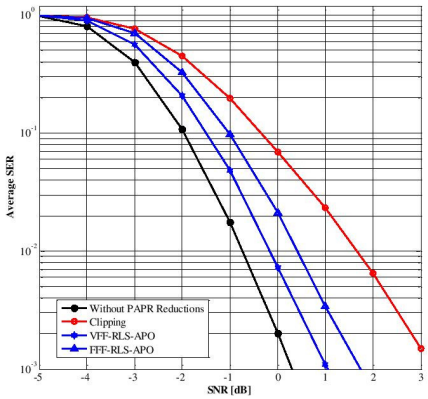


Fig.3 The SER performance of the adaptive PAPR optimizer with RLS algorithms.

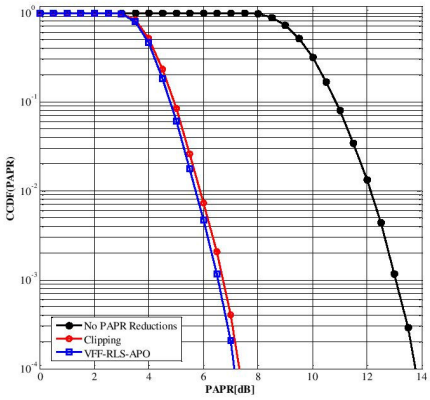


Fig.4 The CCDF (PAPR) performance of all PAPR reduction technique.

The parameters of the adaptive PAPR optimizer are defined as follows: $L$ = 5, a fixed forgetting factor $\chi = 1$, an initial variable forgetting factor $\chi(0) = 1$,

$\vartheta = 0.00001,\ \xi = 0.999,\ \delta = 0.004,\ \zeta(0) = 1,\ e(0) = 1,\ \rho = 0.9996,\ \varpi = 0.001,$
$\varphi(0) = 1,\ J(w^o) = 0.00000625,\ \beta(0) = 1,$ and $\kappa = 1.$

The comparison of both FFF-RLS-APO and VFF-RLS-APO average SER performances with the perfect power control versus $E_b/N_0$ is shown in Fig.3. The proposed method, VFF-RLS-APO, is seen to substantially enhance the SER performance beyond that of the conventional clipping method for every value of $E_b/N_0$.

The complementary cumulative distribution function (CCDF) of PAPR with different schemes is presented in Fig. 4. The adaptive optimizer combined with a VFF-RLS algorithm provides a slightly better PAPR-reduction capability when compared with a conventional clipping-PAPR technique. By itself, the APO does not offer PAPR reduction. It is a tool to assist PAPR reduction schemes for equalizing the clipped signal before sending to each antenna in the downlink channel. The main objective of the APO is to optimize the vector between $\tilde{\boldsymbol{x}}_k$ and $\tilde{\boldsymbol{x}}_{\beta(\zeta),k}$. The desired signal will be the same level as $\beta(\zeta)$ and the same desired signal shape of $\tilde{\boldsymbol{x}}_k$.

## 5. Conclusion

The new tool that assists a PAPR clipping method has been shown by these simulation results to be more effective that clipping in its absence.

## 6. References


1. G. Wunder, R. F. H. Fischer, H. Boche, S. Litsyn, and J. S. No, The PAPR problem in OFDM transmission: New Directions for a Long-Lasting Problem, *IEEE Signal Processing Mag*. **30**, 130 (2013).
2. J. Armstrong, Peak-to-average power reduction for OFDM by repeated clipping and frequency domain filtering, *IEEE Electronics Letters* **38**, 246 (2002).
3. S. Haykin, *Adaptive Filters Theory*, 5th ed. (Prentice-Hall Inc., USA, 2014).
4. S. Sukhumalchayaphong and C. Benjangkaprasert, Variable forgetting factor RLS algorithm for adaptive echo cancellation, in *14th Intl. Conf. on Control, Automation and Systems (ICCAS)*, (Seoul, South Korea, 2014).
5. T. Udomsripaiboon, K. Sieangjen, T. Kungwanchai, N. Sanpote, and C. Benjangkaprasert, The variable step-size algorithm for decision feedback equalizer turbo code DS/CDMA system using SOVA algorithm, in *10th Intl. Conf. on Advanced Communication Technology (ICACT)*, (Gangwon-Do, South Korea, 2008).